Characterization of Chromium Trihalide based Magnetic Tunnel Junctions via First Principles Calculations

by

Jonathan J. Heath

A dissertation submitted to the Graduate Faculty of
Auburn University
in partial fulfillment of the
requirements for the Degree of
Doctor of Philosophy

Auburn, Alabama
May 1, 2021

Keywords: 2D Materials, Magnetic Tunnel Junctions, Ballistic Transport

Approved by

Marcelo A. Kuroda, Chair, Associate Professor of Physics
Jianjun Dong, Professor of Physics
Stuart Loch, Professor of Physics
Sarit Dhar, Professor of Physics
George Flowers, Dean of Graduate School & Professor of Mechanical Engineering

Abstract

At finite temperatures, free-standing two-dimensional (2D) materials were originally theorized to be thermodynamically unstable, let alone possess magnetization. However, in 2018, the first ferromagnetic 2D semiconductor CrI_3 was successfully exfoliated from bulk. Owing to its atomically thin and magnetic properties, CrI_3 became an exceptional 2D material candidate for spintronic research. Shortly following the discovery of monolayer CrI_3, the fabrication of graphene/few-layer CrI_3 based magnetic tunnel junctions (computer memory components) was realized. Through the use of an external magnetic field, these low temperature devices were able to successfully modulate tunneling current through few-layer CrI_3 channels, producing tunneling magnetoresistances of 95%, 300%, and 550% in bilayer, trilayer, and tetralayer CrI_3 junctions, respectively. Although remarkable magnetoristances are achieved in these 2D based junctions, tunneling current is exceptionally low compared to conventional devices due to graphene's low density of states. More fundamentally, the transport mechanisms in graphene/few-layer CrI_3 based devices were not fully understood due to inconsistencies found between experiment and theory.

In our work, we are the first to characterize graphene/N-layer CrI_3 (N = 1, 2, and 3) based magnetic tunnel junctions using first principles calculations within the density functional theorem and Landauer's formalism for ballistic transport. We identify that tunneling is indeed the dominant transport mechanism in graphene/CrI_3 junctions based on their electronic band structures and our ballistic transport calculations, where we achieve tunneling magnetoresistances values of approximately 170% and 350% in bilayer and trilayer junctions, respectively. Moreover, we find that quantum confinement and interlayer coupling play a significant role in describing spin transport through these devices.

Furthermore, we characterize electronic band alignments between N-layer graphene (N = 1, 2, and 3) and monolayer CrX_3 (X = F, Cl, Br, and I) using pseudohybrid Hubbard density functionals, key descriptions missing in the literature. For increasing graphene layers, we note

that Ohmic graphene/CrX_3 contacts transform into Schottky contacts, requiring no external field or force. Additionally, graphene band gaps as large as 173 meV are produced in Bernal stacked graphene/CrF_3 heterojunctions due to significant charge transfer. We offer a simple electrostatic model that describes charge screening in graphene/CrX_3 junctions using isolated material properties.

Lastly, we identify several transition metal dichalcogenide candidates as a graphene substitute, which offer several orders of magnitude greater spin transmission. In addition, we propose a scheme that provides transmission estimates through CrX_3 (X = Br and I) channels based on the complex band structure of bulk CrX_3. This technique is not limited to the 2D materials found in this study, rather it can be extended to incorporate a multitude of material systems.

Acknowledgments

I want to thank my advisor Dr. Marcelo Kuroda for all his support and invaluable guidance during my time at Auburn University. Most of our work together would not be possible without the financial backing of the NSF DMR-1848344 grant and the computational resources of Auburn's Hopper and Easley Clusters. I want to thank the Committee members Dr. Jianjun Dong, Dr. Stuart Loch, and Dr. Sarit Dhar as well as the University Reader Dr. Evangelos Miliordos for all their time and consideration. I want to also recognize our collaborators Dr. Marcio Costa and Dr. Marco Buongiorno-Nardelli for their assistance in our second paper on CrI_3 MTJs (Ref. [1]). I want to thank my friend and colleague Miles Blanchet and Dr. Ryan Comes for involving us in their paper on $CoMn_2O_4$ thin films (Ref. [2]), War Eagle! Additionally, I want to thank the members within my research group and my friends, Lu Wang and Adam Pfeifle, for all of their assistance. Most of all, I want to thank my wonderful fiancee Zahra for all of her support during these trying times.

Table of Contents

List of Figures

List of Tables

List of Abbreviations

2D	Two-dimensional
ACBN0	Agapito-Curtarolo-Buongiorno Nardelli
AFM	Antiferromagnetic
AP	Antiparallel
BS	Band structure
BZ	Brillouin zone
CBE	Conduction band edge
CBS	Complex Band structure
CVD	Chemical vapor deposition
DFT	Density Functional Theory
DOS	Density of states
DP	Dirac point
EA	Electron affinity
ERI	Electron repulsion integrals
FET	Field effect transistor
FM	Ferromagnetic

GGA Generalized gradient approximation

Gr Graphene

H-K Hohenberg–Kohn

HEG Homogeneous electron gas

HF Hartree-Fock

HSE Heyd–Scuseria–Ernzerhof

IE Ionization energy

KS Kohn–Sham

LDA Local-density approximation

MBE Molecular beam epitaxy

MIGS Metal-induced gap states

MOKE Magneto-optical Kerr effect microscopy

MOSFET Metal–oxide–semiconductor field effect transistor

MTJ Magnetic tunnel junction

P Parallel

PAW Projector augmented wave

PBE Perdew–Burke-Ernzerhof

PDOS Projected density of states

PW92 Perdew-Wang 1992

QMC Quantum Monte Carlo

SCF Self-consistent field

SIE	Self-interaction error
TM	Transition metal
TMD	Transition metal dichalcogenide
TMR	Tunneling magnetoresistance
VBE	Valence band edge
vdW	van der Waals
WF	Work function

Chapter 1

Introduction

1.1 2D Material Background

Unlike bulk crystals which extend in all three dimensions, two-dimensional (2D) crystals possess one nano-sized dimension, producing a free-standing layer(s) of atoms. 2D materials were originally theorized to be thermodynamically unstable nearly ninety years ago by Peierls and Landau [18, 19], followed by work of Mermin three decades later [20]. In 2004, however, the first single-atom thick material known as graphene was mechanically exfoliated from its bulk counterpart graphite using a piece of Scotch tape [21]. Soon following the discovery of graphene, a plethora of free-standing 2D crystals were successfully isolated from bulk through mechanical exfoliation or liquid exfoliation via a solvent [22, 23, 24, 25]. Currently, thousands of 2D materials are theorized to be stable based on high-throughput calculations [26].

A 2D material is characterized as a single to a few atoms thick layer, in which strong covalent bonds exist between the in-plane atoms. Moreover, 2D materials weakly interact with neighboring layers (or nonreactive surfaces) by means of the van der Waals (vdW) forces due to the lack of dangling bonds [27]. These 2D structures are commonly referred to as vdW materials in literature based on their interlayer interactions. Some materials like graphene offer unique or enhanced properties compared to conventional materials such as 10 times greater in-plane electron mobility (13,000-15,000 $cm^2V^{-1}s^{-1}$) than silicon at room temperature [28, 29] and nearly 100 times greater tensile strength than steel [30, 31]. Due to the absence of dangling bonds, 2D materials can be readily stacked on top of one another regardless of epitaxy, where nonidentical (identical) stacked layers form heterostructures (homostructures). The formation

of 2D heterostructures (vdW engineering) enables the properties of one or more materials to be modifiable such as the band gap [32]. Alternatively, by changing the stacking order of layers via translational or turbostratic (rotational) displacements, the electronic properties of the structure can also be modified as seen in the case for graphene (Fig. 1.1). Lastly, the most common 2D crystals belong to one of six main 2D material families: Xenes, nitrides, MXenes, transition metal (di)chalcogenides, transition metal (tri)halides, and organic materials.

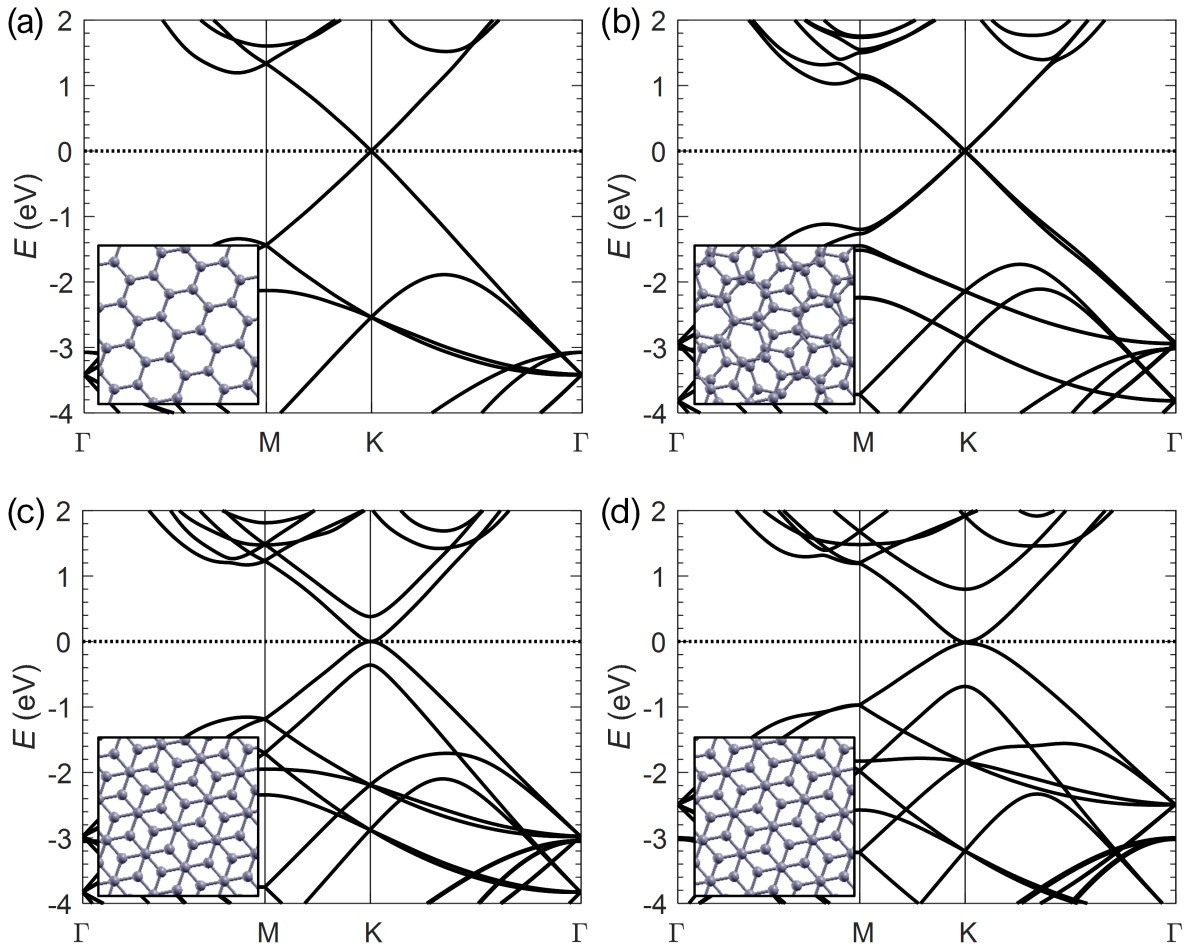

Figure 1.1: Electronic band structure of (a) graphene monolayer (b) turbostratic (rotated) graphene bilayer (c) Bernal stacked graphene bilayer (d) Bernal stacked graphite.

1.1.1 Xenes

Xenes are 2D allotropes of nonmetal or metal elements that remain stable down to the monolayer. The most popular Xene is semimetallic graphene (monolayer of graphite), a single atom thick hexagonal sheet of C atoms. Graphene is the first Xene that was mechanically exfoliated from its bulk counterpart through the famous "Scotch tape method" [21]. Furthermore, graphene is also classified as a 2D Dirac material which produces a crossing of electronic states at a single point in reciprocal space [Dirac point as seen in Fig. 1.1(a)] due to the hexagonal symmetry of the three sp^2 orbitals [33]. Consequently, Dirac fermions with zero effective masses reside at the Fermi energy (highest occupied energy level: E = 0), enabling the high electron mobility in graphene [23]. In addition to graphene, many other Xenes with various properties exist such as silicene [24, 34], germanene [35, 36], phosphorene [37], borophene [38], stanene [39], antimonene [40], bismuthene [41], and plumbene [42].

1.1.2 Nitrides

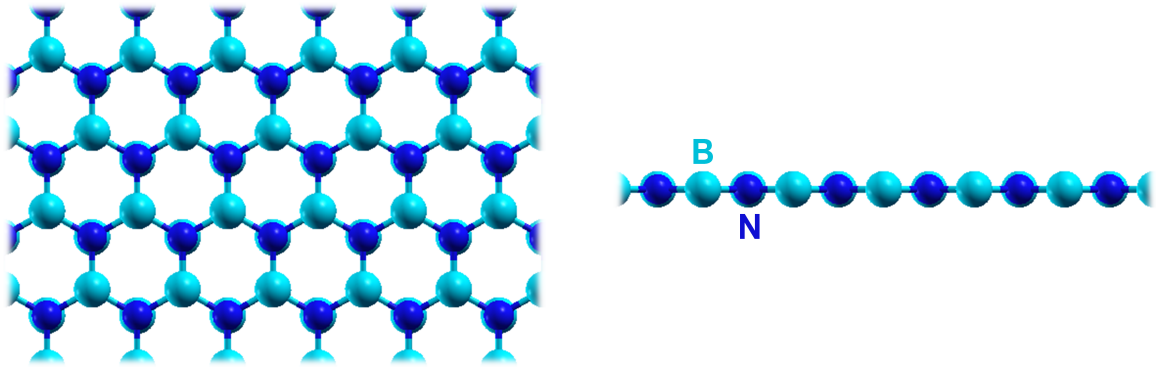

Figure 1.2: Crystal structure of h-BN from a top view (left) and side view (right). Note that h-BN forms a flat hexagonal sheet at one atom thick similar to graphene.

Nitrides are chemical compounds in which pnictogens (nitrogen) are combined with elements with comparable or lower electronegativity. Like carbonides, nitride materials are categorized as covalent, ionic, or interstitial compounds. One of the most popular two-dimensional (2D) nitrides is hexagonal-BN (h-BN), a single atom thick honeycomb sheet composed of alternating B and N atoms (Fig. 1.2). Predicted roughly three decades ago [43] and later chemically synthesized into monolayers [22, 44], h-BN is classified as a wide band gap ($\sim$ 5.9 eV)

semiconductor. Similarly, flat and buckled 2D allotropes of GaN exist [45], which serve as alternative wide band gap semiconductors. Moreover, the growth [46, 47] and chemical exfoliation [48] of graphitic carbon nitride (g-C3N4) was achieved, where the semiconducting g-C3N4 monolayer is comprised of triangular domains of C and N atoms. Lastly, a new 2D metallic nitride Si_2BN is predicted to be stable [49].

1.1.3 MXenes

MXenes are 2D transition metal carbides, nitrides, or carbonitrides with the general formula $M_{n+1}X_nT_x$, where M denotes a transition metal, X denotes C and/or N, T_x denotes surface terminations (commonly T = O, OH, or F), and n = 1 to 4. These 2D materials are derived from MAX bulk crystals with the formula $M_{n+1}AX_n$, where A commonly denotes a group 13 or 14 element. Almost a decade ago, Titanium carbonides $Ti_3C_2T_x$ were the first MXenes produced through the exfoliation of Ti_3AlC_2 crystals (Fig. 1.3) via chemical etching (Al layer removal). Depending on the chemical terminations, $Ti_3C_2T_x$ layers possess metallic or semiconducting properties [50]. Following the discoveries of 2D transition metal carbides, titanium carbonitrides Ti_3CNT_x were more recently produced [51, 52, 53]. Currently, there are over thirty MXenes that exist [54].

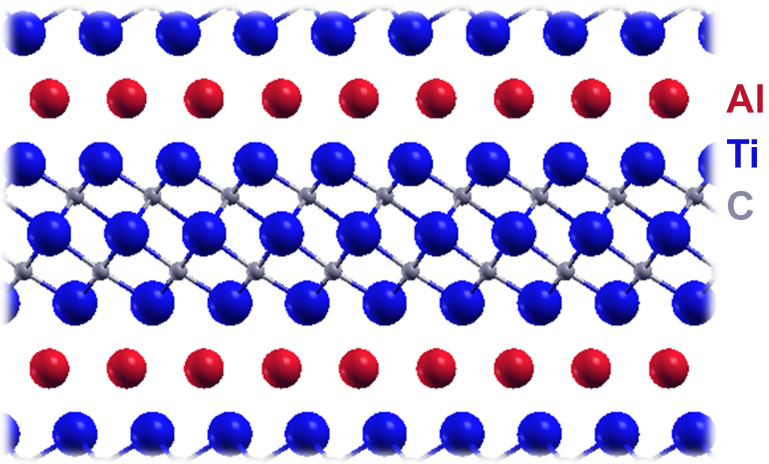

Figure 1.3: Crystal structure of a MAX bulk crystal Ti_3AlC_2 before chemical etching, where Al atoms (red) divide potential MXenes.

1.1.4 Transition Metal (Di)chalcogenides

Transition metal dichalcogenides (TMDs) are comprised of three atom thick layers with the general formula MX_2, where M denotes a transition metal and X denotes a chalcogen. TMDs exist in several polymorphs such as in the 1H / 2H / 3R (hexagonal), 1T (trigonal), or 1T' / 1T" / Pbca (distorted 1T) phases as shown in Fig. 1.4. Both MoS_2 and $NbSe_2$ are the first TMDs that were mechanically exfoliated from bulk following the discovery of graphene [23]; although, monolayer WS_2 and MoS_2 were achieved via intercalation-assisted exfoliation a decade or two prior, respectively [55, 56]. Depending on the phase, MoS_2 (or WS_2) layers possess metallic (1T) or semiconducting (2H) properties. More recently, alternative TMD's have been exfoliated or even grown using molecular beam epitaxy (MBE) such as metallic 1T-$MnSe_2$, 1T-VS_2, and 1T-VSe_2, which all display ferromagnetic properties down to the monolayer [57, 58, 59, 60].

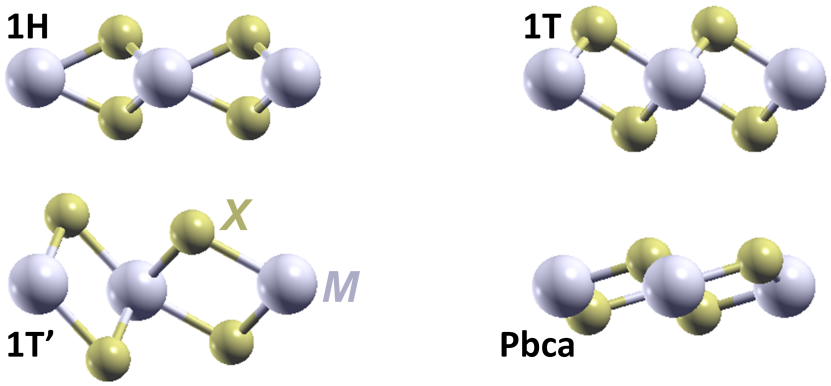

Figure 1.4: Crystal structure of four common TMD polymorphs: 1H, 1T, 1T', and Pbca from a side view.

1.1.5 Transition Metal (Tri)halides

Transition metal trihalides are comprised of three atom thick layers with the general formula MX_3, where M denotes a transition metal and X denotes a halide. At room temperature, transition metal trihalides adopt a monoclinic (C2/m) structure; while for low temperatures, they adopt a rhombohedral ($R\bar{3}$) structure as seen in Fig. 1.5. For over fifty years, bulk MX_3 crystals were known to exhibit magnetic properties below their respective Curie temperatures [61, 62]. The existence of magnetic order in 2D material systems, especially as inherited from their bulk counterparts, was an open question until recent years. Early work by Mermin and Wagner based

on an isotropic Heisenberg model with long-range order determined that at $T > 0$ spontaneous magnetism and antiferromagnetism is absent in two dimensions [63, 64].

However, owing to the extension into a third dimension of most 2D materials, theoretical analyses using first-principles calculations predicted 2D ferromagnetic semiconductors from the exfoliation of K_2CuF_4 or $CrXTe_3$ (X = Si, Ge) crystals [65, 66]. Subsequent experiments in $CrGeTe_3$ [67, 68, 69] and CrI_3 [70] have recently confirmed the attainment of spin order (ferromagnetic or antiferromagnetic) in 2D material systems via magneto-optical Kerr effect microscopy (MOKE) at low temperatures. The first single layer ferromagnetic semiconductor CrI_3 was mechanically exfoliated from bulk [70]. Identical to its bulk counterpart [13], monolayer CrI_3 retains a 1.2 eV band gap based on optical absorbance measurements [70]. Following this achievement, alternative single layer ferromagnetic semiconductors such as $CrCl_3$ and $CrBr_3$ were mechanically exfoliated or grown using MBE [71, 72, 73, 74]. Based on optical absorbance and photoconductivity measurements, bulk $CrCl_3$ and $CrBr_3$ possess 2.3 and 2.1 eV band gaps, respectively [12]. Moreover, monolayer ferromagnetic half-metals VCl_3 and VI_3 are theoretically predicted to be stable [75].

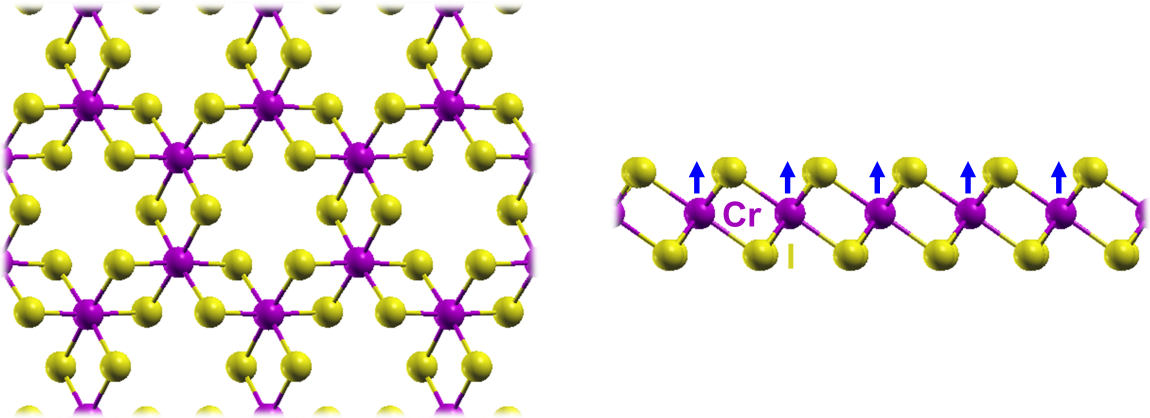

Figure 1.5: Crystal structure of monolayer CrI_3 from a top view (left) and side view (right). Below its Curie temperature, monolayer CrI_3 is ferromagnetic in which magnetic moments (blue arrows) are formed via three unpaired electrons in each Cr atom.

1.1.6 Organic Materials

Organic materials are carbon based compounds which commonly contain other light elements such as H, N, and O. These compounds can be classified as cellulosic materials, proteinaceous materials, or organic polymers. One popular 2D organic material is $Ni_3(HITP)_2$ (HITP = 2,3,6,7,10,11-hexaiminotriphenylene), an open honeycomb structure (P6/mmm constrained symmetry) grown in 2014 via chemical bath deposition. $Ni_3(HITP)_2$ is classified as a semiconducting metal-organic graphene analogue (s-MOG) and is one of the most conductive ($\approx$ 40 S·cm^{-1}) 2D organic materials at room temperature [76]. Properties of these 2D materials under the metal-organic framework (MOF) are modified by changing either the organic functional groups or simply the metal as seen with $Cu_3(HITP)_2$ [77, 78]. Additionally, an alternative allotrope of carbon known as graphyne has been proposed, an open honeycomb structure [79]; although, semiconducting graphdiyne (graphyne with diacetylene groups) currently exists [80].

1.2 Heterostructures

As briefly mentioned prior, due to the lack of dangling bonds, vdW materials may be assembled on top of one another to form heterostructures. These novel structures are formed by means of mechanical assembly (via adhesive tape) or grown using chemical vapor deposition (CVD) and MBE techniques [81]. Over the past decade, some of the most widely studied 2D materials based heterostructures involve the stacking of graphene and h-BN layers [82, 83]. In a study performed by Hunt et al. (2013), monolayer graphene/multilayer h-BN heterostructures were assembled above graphite using a dry transfer technique (polymer and tape) [84]. For structures in which graphene was well oriented with the adjacent h-BN, the formation of a small energy gap of $\sim$30 meV was observed in graphene based on conductivity measurements, as illustrated in Fig. 1.6(a). However, for structures in which graphene was misaligned ($\sim$5 degrees) with the adjacent h-BN [Fig. 1.6(b)], the band gap in graphene reduced to $\sim$10 meV due to weaker interlayer interactions (coupling) [3]. Beyond this achievement in band gap engineering, numerous 2D material based heterojunctions and devices currently exist [81].

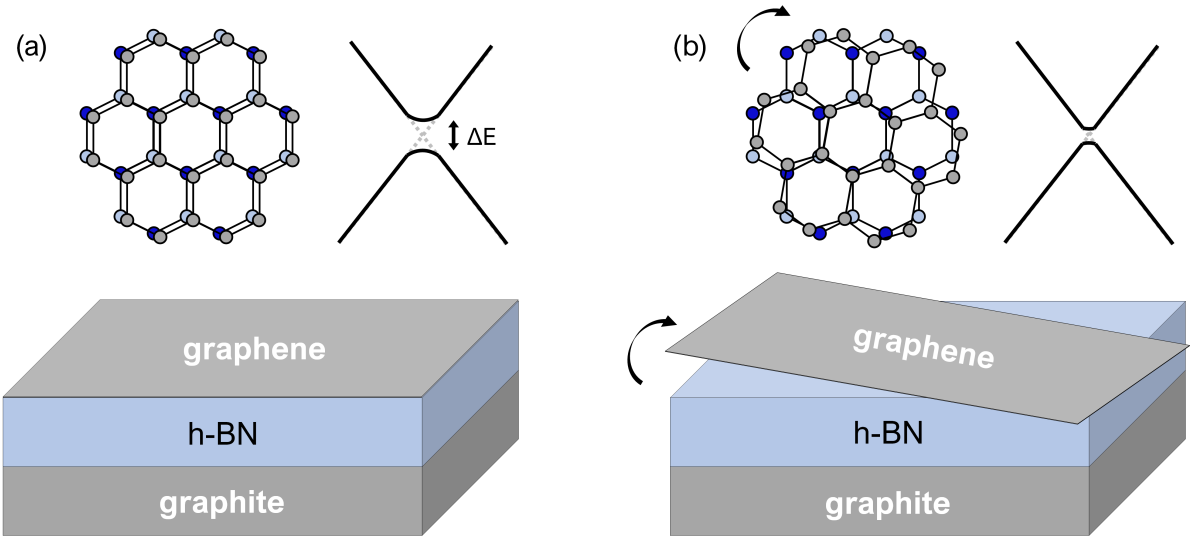

Figure 1.6: Schematic of graphene/h-BN/graphite heterostructure for (a) well oriented graphene/h-BN junctions and (b) turbostratic graphene/h-BN junctions, adapted from [3]. Note that the Dirac point of isolated graphene is marked by gray dashed lines.

1.3 Applications

Recently, 2D materials have become a prime focus in device applications due to their diverse properties, atomic thicknesses, and free-standing assembly. The successful implementation of graphene in a variety of device applications has encouraged researchers to explore the incorporation of alternative vdW materials within 2D based devices [85]. 2D materials offer a broad range of applications including gas sensors, filters, batteries, supercapacitors, transistors, photodetectors, spintronics, and many more [86, 87]. Below, we describe a few applications relevant to our research.

1.3.1 Filtration/Energy Storage Devices

Porous graphene membranes were recently demonstrated as effective desalination devices, capable of filtering nearly 100% of salt from water, rivaling conventional polymer-based materials. This feat was accomplished by etching nanosized pores within the graphene membrane through the use of an oxygen plasma [88]. Beyond filtration, porous graphene membranes have applications in gas sensors [86, 89] and in energy storage devices beyond standard lithium-ion batteries, where the porous graphene sheet serves as a catalyst [90, 91].

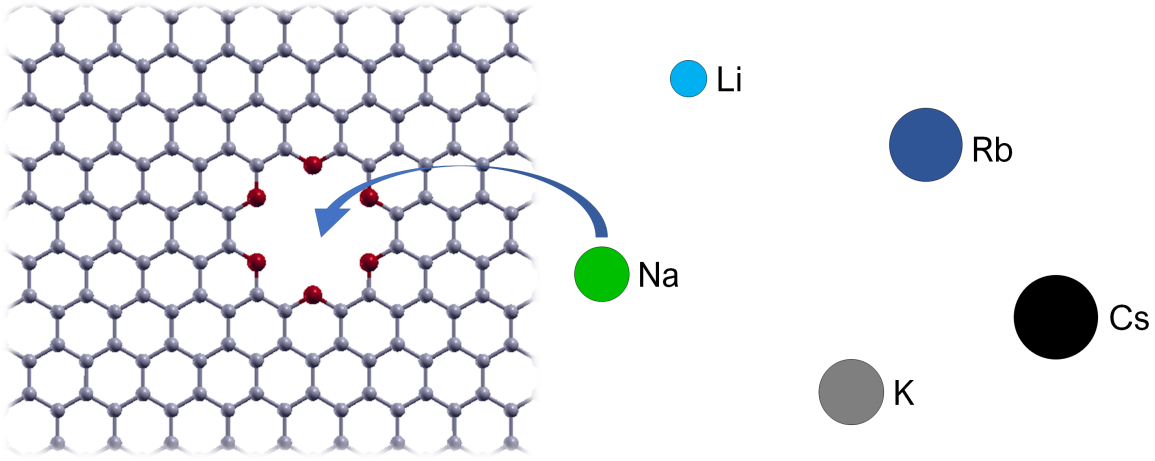

Figure 1.7: Schematic of symmetric oxygen-passivated graphene nanopore interacting with alkali metal elements (or cations), where nanopores behave as docking sites.

In order to characterize porous graphene membranes, we investigated in a prior study the interactions between various oxygen-passivated graphene nanopores and the alkali metals (Li, Na, K, Rb, Cs) via ab initio calculations (Fig. 1.7). We find that each alkali metal binds the strongest to graphene nanopores with openings that match the alkali metal's van der Waals (vdW) radius. The binding energy can also be approximated based on the energy difference between an alkali metal's valence s-state and the Fermi energy of the combined system. As a result of the neighboring alkali metal donating its outermost electron to the porous graphene sheet, the Fermi level draws closer to the localized s-state. Moreover, interactions between alkali metals and pristine graphene can be approximated using the Langmuir–Gurney adsorption model, which treats the graphene layer as an infinite conducting plane. Our work is currently published in Physical Chemistry Chemical Physics **20**, 25822-25828 (see Ref. [92] for more details). Additionally, this work was presented at Oak Ridge National Laboratory during the 2017 Center for Nanophase Materials Sciences (CNMS) User Meeting as well as an oral presentation at the 2018 American Physical Society (APS) March Meeting.

1.3.2 Field Effect Transistors

Metal–oxide–semiconductor field effect transistors (MOSFETs) are one of the most frequent logic components found in electronic devices. The conventional MOSFET is comprised of

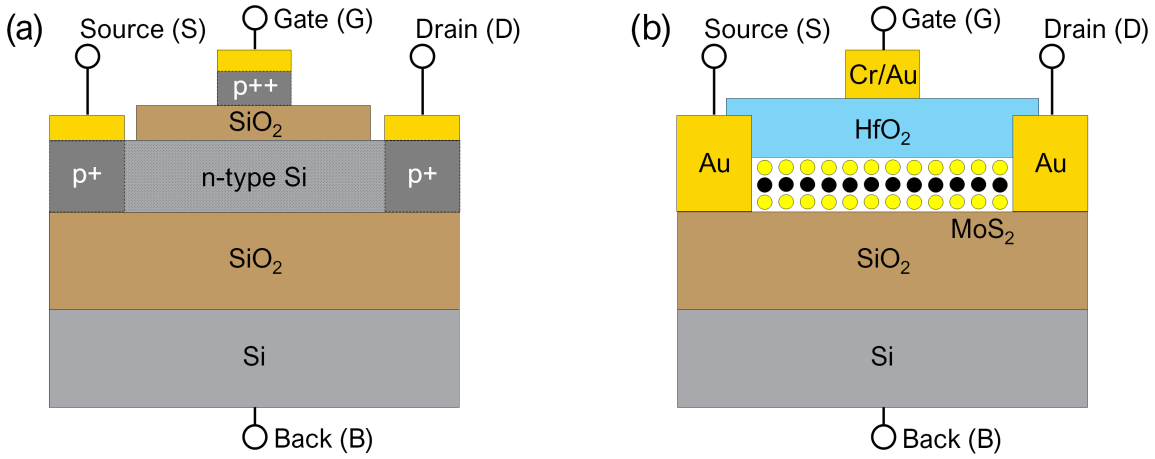

Figure 1.8: (a) Schematic of a conventional silicon based MOSFET where n-type silicon serves as the channel material, adapted from [4]. (b) Schematic of a 2D material 1H-MoS_2 based MOSFET where monolayer MoS_2 serves as the channel material, adapted from [5]. Both p+ and p++ materials represent p-type silicon in the conventional MOSFET. Note that device dimensions are not drawn to scale.

source and drain electrodes linked by a semiconducting channel (commonly silicon). Additionally, a top metal gate lies above the semiconducting channel, separated by a thin oxide film [Fig. 1.8(a)]. Through the use of a top gate voltage V_G, commonly in tandem with a back gate bias V_B, carrier concentrations within the channel are modified. For gate voltages above a particular threshold ("on" state), a drain-to-source voltage V_{DS} can be used to modulate current. One common metric used to gauge the performance of MOSFET devices is the on/off current ratio, a comparison between the total drain current measured with a "high" applied gate voltage versus a "low" applied gate voltage. Moreover, another measure is the subthreshold swing (SS) which measures how readily a device can be swung from an "off" to an "on" state, where an ideal SS value is $\sim$60 mV$\cdot$dec^{-1} [93].

Due to its high in-plane electron mobility, graphene was one of the first 2D materials successfully used as a MOSFET channel substitute roughly ten years ago. These devices utilized bilayer graphene channels to produce on/off ratios on the order of 10^2 at room temperature with the assistance of a 120 V back-gate bias, where the applied electric field opens a small band gap in the bilayer graphene [94]. Following this achievement, single layer 1H-MoS_2 based MOSFETs were fabricated [Fig. 1.8(b)], where the intrinsic 2D semiconductor MoS_2 serves as the channel [5, 95, 96, 97]. These devices offer comparable performance to conventional bulk

Si and GaN based MOSFETs [4, 98, 99], producing on/off current ratios on the order of $\sim 10^8$ and SS values $\sim$70 mV·dec^{-1} [5]. Additionally, alternate MoS_2 based MOSFETs were fabricated with a 1H-MoS_2 channel length below 10 nm enclosed by 1T-MoS_2 metal leads [100]. Recently, dozens of 2D semiconducting materials have been proposed as MOSFET channels, potentially offering a scheme that expands Moore's scaling law for transistors [101].

1.3.3 Magnetic Tunnel Junctions

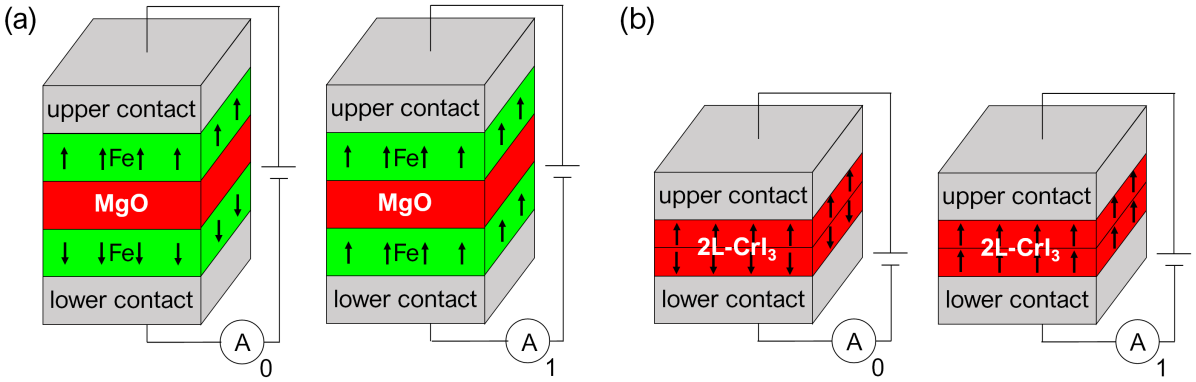

Figure 1.9: (a) Schematic of a conventional iron based MTJ in a antiferromagnetic (left) versus ferromagnetic (right) state, adapted from [6]. (b) Schematic of a 2D material CrI_3 based MTJ in a antiferromagnetic (left) versus ferromagnetic (right) state, adapted from [7]. Note that device dimensions are not drawn to scale.

Magnetic tunnel junctions are modern components found in computer storage and memory devices such as magnetoresistive random-access memory (MRAM) [102]. Similar to the MOSFET, the conventional magnetic tunnel junction (MTJ) is comprised of magnetic source and drain electrodes (typically Fe) separated by a thin semiconducting or insulating barrier such as MgO [Fig. 1.9(a)]. Depending on whether the left and right electrodes are magnetized in the same direction (ferromagnetic) or in opposite (antiferromagnetic) directions, the amount of spin current passing (tunneling) through the barrier is modulated [103]. This modulation in total tunneling current is caused by changes in the number of available spin states in each electrode based on magnetization as demonstrated in Fig. 1.10. Like the on/off ratio performance metric, tunneling magnetoresistance (TMR) measures the relative difference in resistivity (or conductivity) between the ferromagnetic (magnetically aligned electrodes) and antiferromagnetic (magnetically misaligned electrodes) MTJ. Common MTJs are found to produce TMR

values roughly between 100-200% [6, 104, 102, 105], although low temperature devices have achieved TMR values on the order of 10^3% by utilizing electrodes made of cobalt-iron alloys [106].

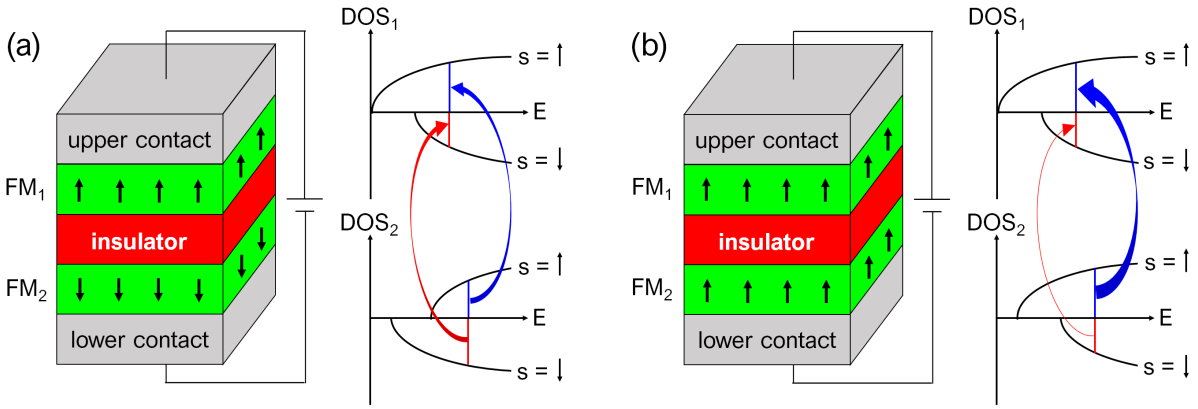

Figure 1.10: Schematic illustrating the relative spin up and down states available within each magnetic lead of a conventional MTJ in the (a) antiferromagnetic and (b) ferromagnetic state, adapted from [6] and [8]. Note that the line width of blue (spin up) and red (spin down) arrows represent the amount of tunneling current.

The discovery of the single layer ferromagnetic semiconductor CrI_3 enabled fundamental studies on the impact of dimensionality on strongly correlated phenomena and offered a desirable building block for 2D based spintronic devices. Recent works have successfully incorporated few-layer CrI_3 within 2D based MTJs at low temperatures [7, 107]. These newly fabricated graphene/CrI_3 based MTJs exploit the magnetic and semiconducting properties of CrI_3, where few-layer CrI_3 serves a dual role as both a magnetic switch and insulating barrier [Fig. 1.9(b)]. Under the Curie temperature (T_C =45 K) of few-layer CrI_3, the magnetic moments (3 μ_B/Cr) in adjacent CrI_3 layers oppose one another, resulting in an interlayer antiferromagnetic state. Through the use of a strong magnetic field ($\sim$1 T), the magnetic moments in adjacent CrI_3 layers align, producing a ferromagnetic state [13]. These ultrathin 2D devices are capable of producing TMR values of 95% for bilayer channels and up to 550% for tetralayer channels [7], comparable values observed in conventional bulk junctions. Additionally, new studies have examined $CrCl_3$ and $CrBr_3$ based devices, where bilayer channels using $CrCl_3$ produce comparable results to CrI_3 based junctions. Unlike $CrCl_3$ and CrI_3, the magnetic state of few-layer $CrBr_3$ does not change under an external magnetic field due to its ferromagnetic ground state [108].

1.3.4 Limitations

Regarding the application of 2D materials within MOSFETs, many of these 2D based devices operate at significantly higher threshold voltages ($\sim$10 volts) compared to conventional bulk devices [109]. Although, through the use of high dielectric thin films in tandem with 2D materials, threshold biases can be reduced by roughly one magnitude [95]. In addition, carrier mobilities in MoS_2 based MOSFET channels are roughly ten times lower than in silicon [5]. Unlike standard bulk MTJ devices, current 2D based magnetic tunnel junctions require sub-100 K temperatures and large external magnetic fields ($\sim$1 T) to alter the magnetic order of the channel material [7, 108]. Several theoretical studies show that various point defects such as vacancies and substitutions can significantly alter local magnetization in monolayer CrI_3, resulting in ferromagnetic to antiferromagnetic phase transitions [110, 111, 112].

Furthermore, graphene leads found in 2D based junctions exhibit perpendicular electron mobilities comparable to silicon and are further limited by their low carrier densities, producing conductivity values perpendicular to their basal plane ($\approx$ 3 S$\cdot$cm^{-1}) [113, 114, 115] roughly 10^5 times lower than in iron [116, 117] at room temperature. Due to the low perpendicular conductivity in graphene, alternative 2D lead materials are desired. Several metallic TMDs such as 2H-$NbSe_2$ demonstrate two orders of magnitude greater perpendicular conductivity ($\approx$ 200 S$\cdot$cm^{-1}) than in graphene, yielding promising electrode candidates [118]. Moreover, this is further illustrated by comparing the disproportionately low density of states (DOS) of graphite with the DOS of 2H-$NbSe_2$ as seen in Fig. 1.11. Apart from large operational costs in 2D based devices, the mass production of 2D materials themselves still remains a challenge [119, 120]. Although limitations currently exist regarding the implementation of 2D materials in practice, 2D materials offer unique properties and unparalleled scalability due to their atomic thicknesses [121].

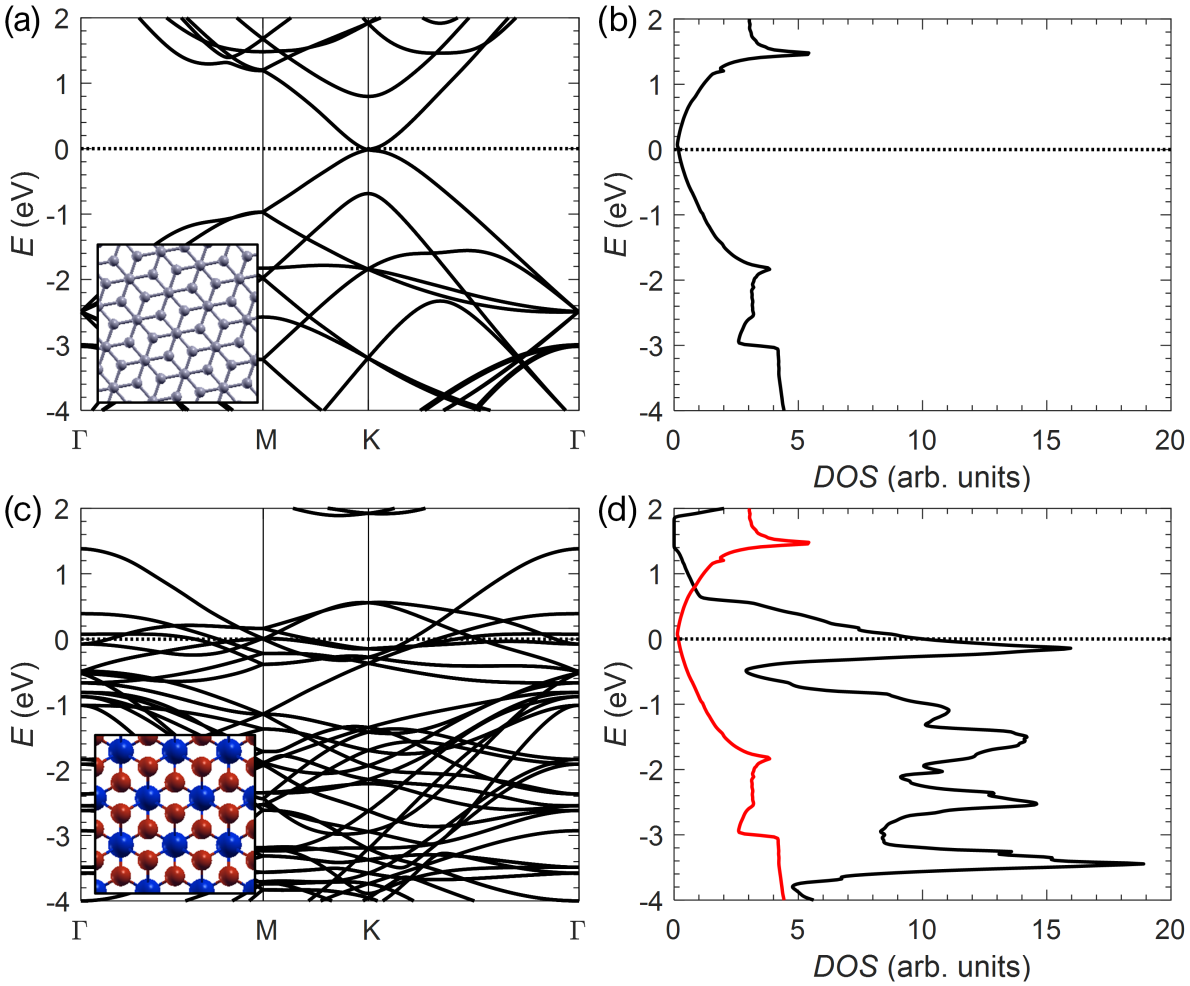

Figure 1.11: Electronic band structure of (a) graphite and its (b) corresponding density of states (DOS). Note that the DOS of graphite vanishes at the Fermi energy (E = 0) or Dirac point. Electronic band structure of (c) 2H-$NbSe_2$ and its (d) corresponding DOS with the DOS of graphite overlaid in red.

Chapter 2

Methodology

2.1 Electronic Band Structure

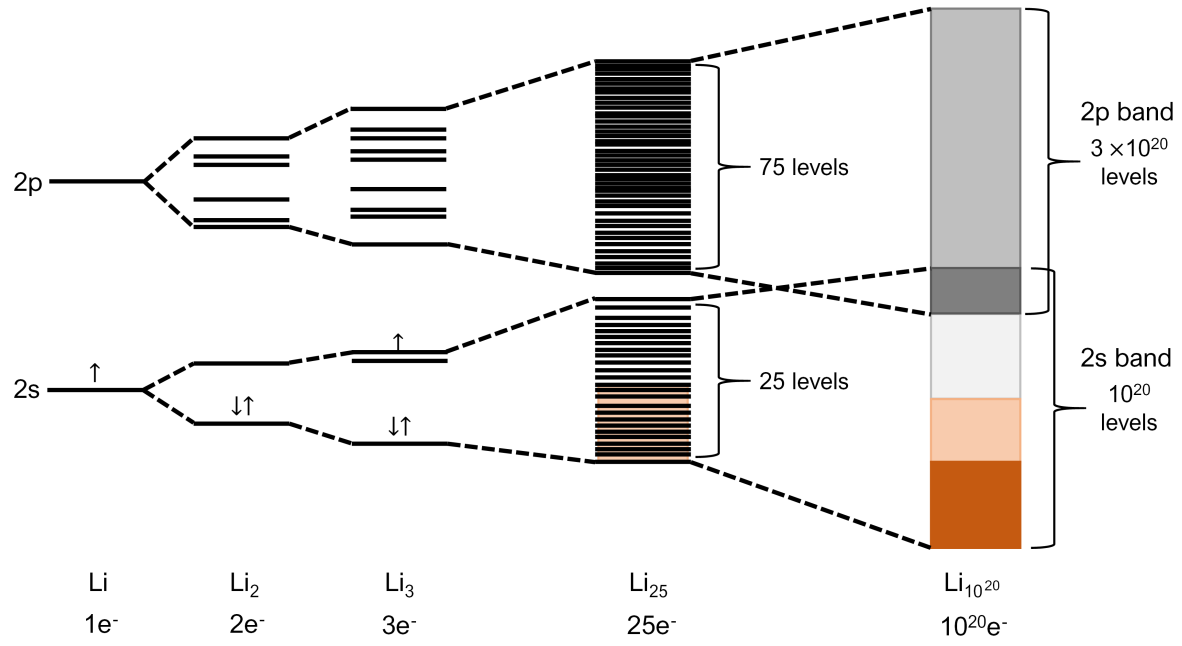

Figure 2.1: Electronic band formation as a result of energy level splitting for increasing numbers of lithium atoms, adapted from [9]. Note that occupied levels are indicated in orange while the unoccupied are indicated in gray, where darker colors refer to more states.

Within an isolated atom, bound electrons posses discrete energies pertaining to atomic orbital occupation. Through the introduction of an additional atom(s) to the system, atomic orbitals begin to interact (overlap), which causes energy level splitting due to the formation of molecular orbitals. As the number of atoms become sufficiently large in a system, such as in a solid crystal, the atomic states broaden or split to such an extent that energy levels within a range appear continuous, resembling a "band" of energy [122]. The formation of electronic

bands is illustrated in Fig. 2.1 for the case of lithium. Note that no gap is formed between the occupied valence bands (orange) and the unoccupied conduction bands (gray) in lithium. Materials that exhibit no band gap at the Fermi energy are referred to as metals, while materials that do exhibit a band gap are referred to as semiconductors or insulators, if the gap is large [123].

2.1.1 k-Space

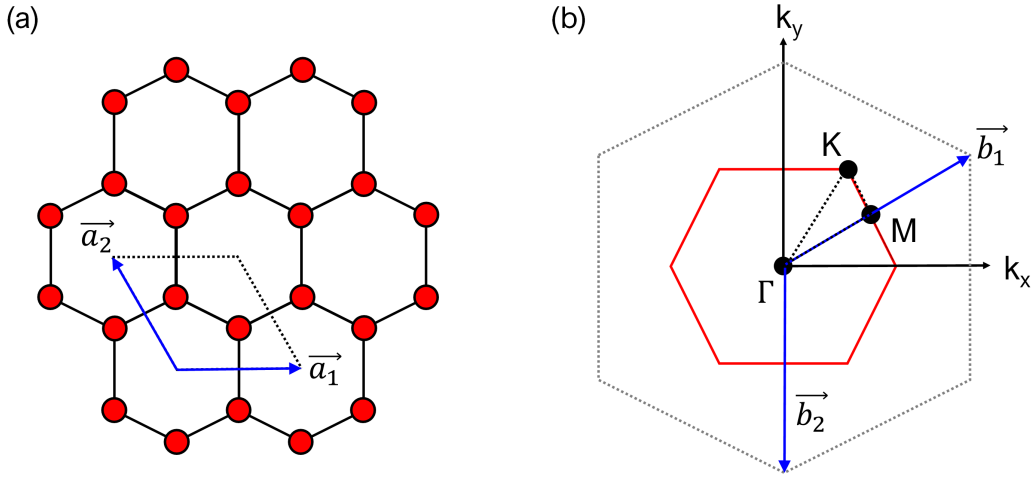

Figure 2.2: (a) Schematic of a 2D hexagonal crystal, where lattice vectors a_1 and a_2 trace two sides of the primitive unit cell (dotted lines), a periodically repeating unit. (b) Hexagonal symmetry expressed in reciprocal space, where reciprocal lattice vectors b_1 and b_2 map out an area in reciprocal space known as the (2D) Brillouin zone, adapted from [10]. The first Brillouin zone (traced in red) features three in-plane symmetry points: Γ, M, and K.

For a perfect crystal system, a group of atoms within a volume (unit cell), defined by a set of lattice parameters (lengths and angles), periodically repeat across the Bravais lattice of the crystal [124]. This is shown in Fig. 2.2(a) for a 2D hexagonal crystal, where lattice vectors a_1 and a_2 mark points along the Bravais lattice in which the unit cell (area within dashed line) repeats. Due to the periodicity of the crystal, the potential and eigenfunctions of the system may be expressed in terms of a translation vector, a sum of displacements that repeat the crystal pattern, imposed by Born–von Karman boundary conditions [125]. As demonstrated in the formalism of Bloch's Theorem, the periodically repeating potential can be transformed using a Fourier series expansion into reciprocal space or "k-space", physically interpreted as crystal momentum space [126]. Similar to position space, atomic information is contained within a

unit cell of k-space known as the Brillouin zone (BZ) [127]. This is illustrated in Fig. 2.2(b) for the hexagonal crystal, where the reciprocal lattice vectors b_1 and b_2 trace two sides of a unit cell. Due to symmetry (periodicity), the rhombohedral cell may be expressed in terms of the first Brillouin zone (red hexagon). A consequence of the system being represented in reciprocal space is that eigenvalues are k-dependent, requiring k-point sampling (evaluation) within the BZ. However, rather than trying to visualize a four-dimensional space, the k-dependent eigenvalues (or bands) are plotted by taking cuts (paths) through k-space between various symmetry points as seen in Fig. 1.11(a) and (c).

2.1.2 Complex Band Structure

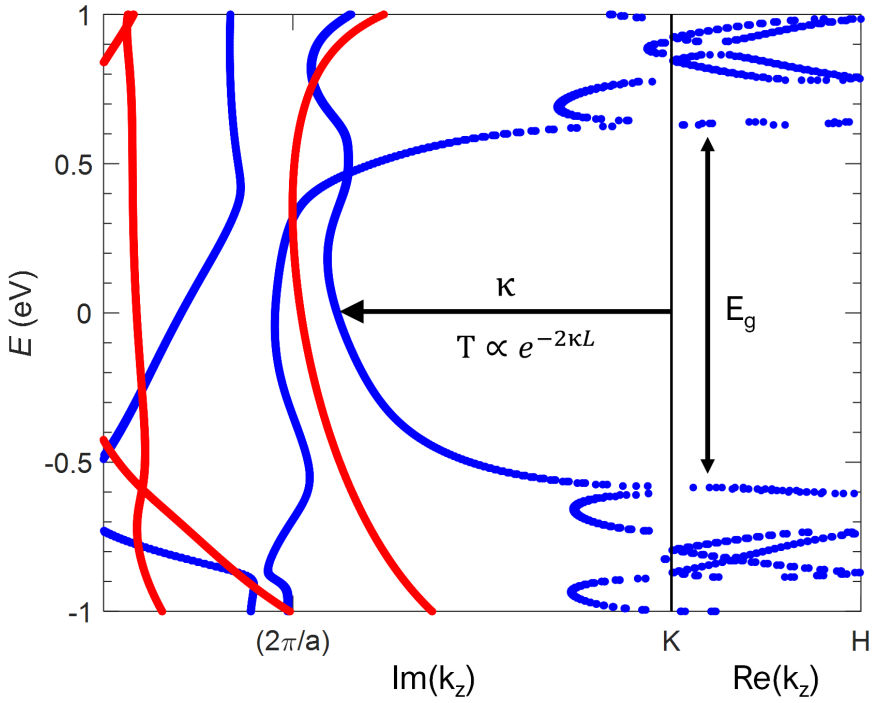

Figure 2.3: The complex band structure of ferromagnetic bulk CrI_3 along the k_z-direction (perpendicular to the basal plane) relative to the K-point for both spin majority (blue) and spin minority (red). Note that spin majority imaginary wavevectors κ within the band gap E_g are shorter than the spin minority wavevectors, resulting in greater spin majority transmission probabilities T through CrI_3 for a distance L.

Beyond the conventional electronic band structure (BS) of a crystal where electron eigenstates are a function of the real wavevector k, the complex band structure (CBS) of the crystal introduces an imaginary wavevector component κ [128], as seen in Fig. 2.3 for the magnetic

semiconductor CrI_3. This generalization of the band structure provides information on the dynamic properties of the system, notably, electron transport. These imaginary or evanescent states govern the likelihood an electron at a fixed energy passes through one unit cell of the crystal to the next, where the imaginary wavevector κ represents the decay constant [129]. In the case of ferromagnetic bulk CrI_3 (Fig. 2.3), imaginary wavevectors κ for spin up (blue) electrons within the CrI_3 band gap are shorter than the spin down (red) wavevectors perpendicular to the K-point, resulting in lower spin up barriers compared to the spin down barriers.

2.2 Hartree-Fock Method

The Hartree-Fock (HF) method approximates the energy of an N-body electron system by utilizing the variation principle, where a single Slater determinant of single particle orbitals is used as the trial wavefunction for the ground state [130, 131, 132, 133, 134]. In order to calculate the energy of the system, the HF method introduces a single particle Fock operator $\hat{F}(1)$, an element in the Fock matrix, which provides the energy of an electron occupying orbital ϕ_i:

$$\epsilon_i =< \phi_i(r)|\hat{F}(1)|\phi_i(r) > \tag{2.1}$$

$$=< \phi_i(r)|\hat{H}^0(1)|\phi_i(r) > + \frac{e^2}{4\pi\epsilon_0}\sum_{j=1}^{N}(2J_{ii} - K_{ij}) \tag{2.2}$$

$$=< \phi_i(r)|\frac{-\hbar^2}{2m_e}\nabla^2 - \frac{e^2}{4\pi\epsilon_0}\sum_{\alpha=1}^{N_\alpha}\frac{Z_\alpha}{|r - R_\alpha|}|\phi_i(r) > + \frac{e^2}{4\pi\epsilon_0}\sum_{j=1}^{N}(2J_{ii} - K_{ij}) \tag{2.3}$$

$$= T_s(\phi_i) + U_{eN}(\phi_i) + U_H(\phi_i) + E_X(\phi_i), \tag{2.4}$$

where $\hat{H}^0(1)$ is the hydrogen-like operator, $J_{ii} =< \phi_i(r)\phi_j(r')|\frac{1}{|r-r'|}|\phi_i(r)\phi_j(r') >$ are the Coulomb integrals, and $K_{ij} =< \phi_i(r)\phi_j(r')|\frac{1}{|r-r'|}|\phi_j(r)\phi_i(r') >$ are the exchange integrals. Moreover, the expectation value of the core operator $\hat{H}^0$ provides the single particle kinetic energy T_s and the Coulomb interaction energy U_{eN} between an electron and N_α atomic nuclei. The electron repulsion integrals (ERI), J_{ii} and K_{ij}, provide the electron-electron Coulomb U_H and exchange E_X energies [135].

2.3 Density Functional Theory

Density Functional Theory (DFT) originates from the semiclassical Thomas-Fermi model [136, 137], which attempts to express the energy of a many-body electronic system in terms of the electron (probability) density n to reduce the number of degrees of freedom (spatial coordinates) required in the solution:

$$E = T_s[n] + U_{eN}[n] + U_H[n] \tag{2.5}$$

$$= \frac{3h^2}{40m_e}\left(\frac{3}{\pi}\right)^{2/3}\int n(r)^{5/3}d^3r + \int n(r)V(r)d^3r + \frac{e^2}{2}\int\int\frac{n(r)n(r')}{|r-r'|}d^3rd^3r', \tag{2.6}$$

where T_s is the non-interacting (single particle) kinetic energy found via statistical mechanics, U_{eN} is the Coulomb interaction between electrons and atomic nuclei, and U_H is the classical electron-electron Coulomb interaction. The DFT framework, however, is succinctly introduced through the Hohenberg–Kohn (H-K) theorems [138], which establish that the ground state energy for an interacting many-body system may be expressed by a universal functional of the density. By invoking the variational principle, the second H-K theorem demonstrates that the ground state wave function coincides with a unique electron density which minimizes the energy of the system. Moreover, the H-K theorems propose a gradient expanded density functional to account for the kinetic and exchange terms. Building upon H-K theory, Kohn–Sham (KS) DFT [139] attempts to decouple the many-body problem by treating the exchange-correlation energy E_{XC} as a correctional term (effective potential):

$$E = T_s[n] + U_{eN}[n] + U_H[n] + E_{XC}[n], \tag{2.7}$$

where $E_{XC}[n] = (T[n] - T_s[n]) + (U_{ee}[n] - U_H[n])$ in which T and U_{ee} represent the exact kinetic and electron-electron interaction energy, respectively. Similar to the Hartree-Fock method, the ground state solution using KS DFT is an expansion of single-particle wavefunctions known as Kohn-Sham orbitals, solutions for independent particles within an effective potential.

2.3.1 Local Density Approximation

The local-density approximation (LDA) of the exchange-correlation energy may be expressed as an explicit functional of the electron density:

$$E_{XC}^{LDA}[n] = \int n(r)\epsilon_{XC}^{HEG}(n(r))d^3r \tag{2.8}$$

$$= \int n(r)\epsilon_{X}^{HEG}(n(r))d^3r + \int n(r)\epsilon_{C}^{HEG}(n(r))d^3r \tag{2.9}$$

$$= E_X^{LDA}[n] + E_C^{LDA}[n], \tag{2.10}$$

where $\epsilon_{XC}^{HEG}(n)$ represents the exchange-correlation energy per particle of a homogeneous electron gas (HEG), a single particle effective potential. Moreover, the exchange-correlation energy functional is separable: $E_{XC}[n]$ = $E_X[n]$ + $E_C[n]$ [140]. Through Dirac's corrections on the Thomas-Fermi model of the HEG, an analytical expression of the LDA exchange functional exists [141]:

$$E_X^{LDA}[n] = -\frac{3}{4}\left(\frac{3}{\pi}\right)^{1/3}\int n(r)^{4/3}d^3r. \tag{2.11}$$

Unlike the exchange energy, exact analytical expressions of the correlation energy for HEG only exist for the low and high electron density limits [142, 143]. In order to estimate the correlation energy at intermediate densities, various studies propose interpolations of quantum Monte Carlo (QMC) results for the HEG [144, 145, 146, 147], such as the Perdew-Wang 1992 (PW92) functional:

$$E_C^{PW92}[n] = -2A(1+\alpha_1 r_s)\ln\left(1+\frac{1}{2A(\beta_1 r_s^{1/2}+\beta_2 r_s+\beta_3 r_s^{3/2}+\beta_4 r_s^{p+1})}\right), \tag{2.12}$$

where $r_s = (4\pi n(r)/3)^{-1/3}$ while β_1, β_2, β_3, β_4, and p are fit parameters [148].

2.3.2 Generalized Gradient Approximation

The generalized gradient approximation (GGA) of the exchange-correlation energy may be expressed as a functional of both the electron density and gradient of the density:

$$E_{XC}^{GGA}[n] = \int n(r)\epsilon_{XC}^{GGA}(n(r), \nabla n(r))d^3r \tag{2.13}$$

$$= \int n(r)\left[\epsilon_{XC}^{HEG}(n(r)) + H(n(r), \nabla n(r))\right]d^3r, \tag{2.14}$$

where $\epsilon_{XC}^{GGA}(n)$ is the gradient expanded single particle exchange-correlation function in which the first-order expansion is assumed to be the exchange-correlation term for a HEG $\epsilon_{XC}^{HEG}(n)$ while the second-order expansion corresponds to a perturbative term $H(n, \nabla n)$. The gradient correction $H(n, \nabla n)$ helps capture inhomogeneity in the electron density, a key feature missing in the LDA. The LDA alone commonly underestimates the exchange energy while overestimating the correlation energy due to the assumption of uniformity [138, 149]. Similar to the LDA, various studies propose viable gradient corrections [150, 151, 152], such as the Perdew–Burke-Ernzerhof (PBE) functional:

$$E_{XC}^{PBE}[n] = \int n(r)\epsilon_{XC}^{HEG}(n(r))F_{XC}(n(r), \nabla n(r))d^3r, \tag{2.15}$$

where F_{XC} is the enhancement factor, a non-trivial gradient expanded correction to LDA that satisfies both the high and low density limits of the HEG [153].

2.3.3 ACBN0 Hubbard Density Functional

The Agapito-Curtarolo-Buongiorno Nardelli (ACBN0) Hubbard density functional [154] is denoted as a pseudohybrid functional that modifies local approximations of the exchange-correlation energy by introducing an effective Hubbard correction (DFT+U), obtained self-consistently. The Hubbard correction introduces two parameters $\bar{U}$ (on site Coulomb term) and $\bar{J}$ (on site exchange term) or more simply the effective Hubbard term $U = \bar{U} - \bar{J}$. This Hubbard correction, in effect, represents a parameterized version of the Hartree-Fock (HF) exchange-correlation. The ACBN0 approach attempts to solve for these Hubbard parameters

by directly calculating the HF Coulomb and exchange terms using the resulting electron density from local approximations of DFT and setting this HF estimate equal to the Hubbard correction. Before computing the electron repulsion integrals (ERI) found in the HF method, the ACBN0 approach projects the electronic density onto pseudo-atomic orbitals (PAO) in order to preserve orbital localization found in HF theory. By factoring in localization effects and reducing the self-interaction error (SIE), the ACBN0 functional improves DFT approximations of the electronic band structures (such as band gaps) of insulators.

2.3.4 Heyd–Scuseria–Ernzerhof Functional

The Heyd–Scuseria–Ernzerhof (HSE) exchange-correlation functional [155] belongs to a class of hybrid functionals that attempt to correct the exchange energy from DFT by hybridizing the Hartree-Fock exchange with local approximations of the exchange energy [156]. HSE is a parameterized expansion of the PBE0 functional which mixes the HF exchange (or Kohn–Sham exchange in the case of a crystal system) with the exchange-correlation energy from PBE. More specifically, the Coulomb operator used to calculate the exchange terms is expanded into a short and long range screened potential as shown below:

$$\frac{1}{r} = \frac{1 - \text{erf}(\omega r)}{r}\bigg|_{SR} + \frac{\text{erf}(\omega r)}{r}\bigg|_{LR}, \tag{2.16}$$

where the decay constant ω is a parameter. Here, the short range screened Coulomb potential is used to calculate the HF exchange energy, enabling higher electron localization and consequently improved approximations for the electronic band structures, particularly, of insulating systems. The full hybrid functional is given by the following expression:

$$E_{XC}^{\omega PBEh} = \alpha E_X^{HF}(\omega)\bigg|_{SR} + (1-\alpha)E_X^{PBE}(\omega)\bigg|_{SR} + E_X^{PBE}(\omega)\bigg|_{LR} + E_C^{PBE}(\omega), \tag{2.17}$$

where α is the mixing parameter [155].

2.4 Transport

The mechanisms behind electronic transport in electronic devices, comprised of a channel material enclosed by two metal contacts or reservoirs, are highly dependent upon the dimensions of the scattering region. More general than the Drude-Sommerfield formulation of the free electron model [157, 158], the semi-classical Boltzmann transport equation predicts diffusive electron current density j_z in microscopic channel devices:

$$j_z = -e \int \frac{d^3\mathbf{k}}{(2\pi)^3} v_z(\mathbf{k}) \left[f_L(E(\mathbf{k})) - f_R(E(\mathbf{k})) \right] \tag{2.18}$$

$$= -e^2 \int \frac{d^3\mathbf{k}}{(2\pi)^3} v_z(\mathbf{k}) \left[\mathcal{E}_z v_z(\mathbf{k}) \tau(E(\mathbf{k})) \left(-\frac{\partial f^{FD}}{\partial E} \right) \right], \tag{2.19}$$

where v_z is the electron drift velocity along the scattering channel while f_L and f_R are the Fermi-Dirac distribution functions of the left and right reservoirs (Fig. 2.4). Through the linear response method, the electron current density may be expressed in terms of a small perturbative field $\mathcal{E}_z$ and a scattering quantity known as the relaxation time τ, the average time between collisions an electron experiences. The relaxation time approximation offered in the Boltzmann approach, however, begins to break down as the length of the device channel approaches several characteristic lengths such as the de Broglie wavelength of the charge carriers, the mean free path, or the phase relaxation length, where the last two quantities represent the average travel distance of an electron before undergoing elastic or inelastic scattering, respectively [159].

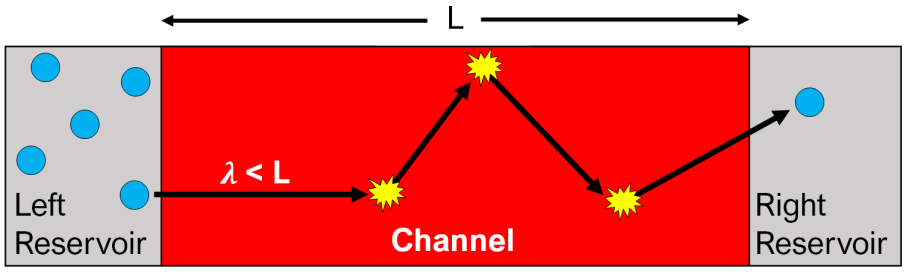

Figure 2.4: Simplified illustration of diffusive transport through a channel with length L, adapted from [11]. Note that the mean free path λ of electrons are smaller than the channel length L, resulting in scattering events (yellow symbols).

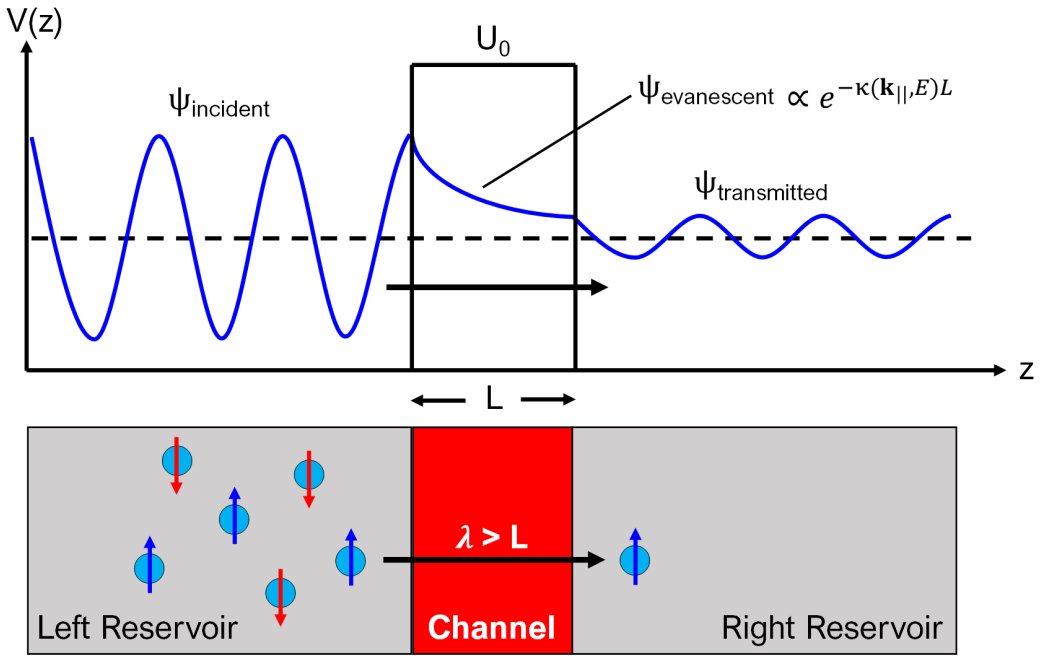

Figure 2.5: Simplified illustration of ballistic transport through a spin dependent barrier U_0 produced by a thin magnetic channel of length L, adapted from [8]. Note that the mean free path λ of electrons are comparable or larger than the channel length L.

In order to determine the current through channels where scattering processes play a negligible role in transport, the Landauer-Büttiker formalism of ballistic transport was developed [160, 161]. Unlike diffusive transport, the Landauer-Büttiker approach treats electron conduction through the channel as a transmission or tunneling problem based on quantum scattering theory (Fig. 2.5), which is given by the Caroli expression [162, 163]:

$$j_z = \frac{-e^2}{(2\pi)^2 h} \int dE \int_{BZ_{||}} d^2\mathbf{k}_{||} \sum_{i,j} t_{i,j}(\mathbf{k}_{||}, E) \left[\frac{\mu_L - \mu_R}{e} \left(-\frac{\partial f^{FD}}{\partial E} \right) \right] \tag{2.20}$$

$$= \sigma_z \left[\frac{\mu_L - \mu_R}{e} \right], \tag{2.21}$$

in which the current density is comprised of planar $\mathbf{k}_{||}$-resolved electron transmission amplitudes $t_{i,j}(\mathbf{k}_{||}, E)$ between subband i in the left reservoir and subband j in the right reservoir, where μ_L and μ_R represent the chemical potentials of the left and right reservoirs, respectively [164, 165]. In general, the conductivity of a magnetic channel following Landauer's formalism

is given by:

$$\sigma_m = \frac{G_0}{A} \sum_{s=\uparrow,\downarrow} T_s^m(E). \tag{2.22}$$

where $G_0 = e^2/h \approx 38.7$ μS represents the conductance quantum [166], A represents the channel's cross-sectional area, s represents the electron spin (majority or minority) channel, and $T_s^m(E)$ represents the average transmission probability corresponding to a spin channel ($\uparrow$ or $\downarrow$) for a system in the magnetic state m. The average transmission probability can be defined by inserting Eq. 2.22 into the definition of Ohm's law in Eq. 2.21 [166, 167, 168]:

$$T_s^m(E) \equiv \frac{A}{(2\pi)^2} \int dE \int_{BZ_{||}} d^2\mathbf{k}_{\|} \sum_{i,j} t_{i,j,s}(\mathbf{k}_{||}, E) \frac{df}{dE}, \tag{2.23}$$

where the transmission probability is an average of the momentum-resolved transmissions over the 2D-BZ.

2.5 Computational Details

Regarding results obtained in the forthcoming Chapters 3-5, first principles calculations (DFT) are carried out using the Quantum Espresso software [169, 170, 171, 172], where the exchange-correlation energy is parameterized by spin polarized generalized gradient approximation (PBE) functionals [173] including dispersion forces (vdW-DF-C09) [174, 175, 176]. Atomic cores are characterized via projector augmented wave (PAW) pseudopotentials [177, 178] with cutoff energies of 50 Ry and 500 Ry regarding the Kohn-Sham wave functions and densities, respectively. Note that these energy cutoffs define the number of Fourier terms (plane-waves) used in each expansion. For magnetic 2D material systems, metal atoms in each layer are assigned a starting magnetization. Additionally, the projected density of states (PDOS) and the electronic band structures of various systems are computed to analyze the results. Due to the large supercells employed in these studies (as large as $\sim$300 atoms or $\sim 10^3$ electrons), we perform all calculations on the Hopper Cluster and the new Easley Cluster (two of Auburn's supercomputers). The remaining computational details are found later within each Chapter.

Chapter 3

CrI_3 Magnetic Tunnel Junction

3.1 Summary and Background

Here we describe the tunneling magnetoresistance (TMR) in graphene/CrI_3/graphene heterostructures using first principles calculations within the density functional theory (DFT) and Landauer's formalism for ballistic transport. Our results reveal that tunneling is the dominant transport mechanism, reconciling atomistic descriptions to experimental observations [7]. Analysis of the band structure of few-layer CrI_3 junctions reveals that the interplay between quantum confinement and interactions between layers is essential to defining band alignments and the resulting tunneling barriers. As a consequence, the effective spin tunneling barriers vary with both thickness and magnetic ordering in the CrI_3 layers. The magnetoresistance values obtained by employing Landauer's formalism to various metamagnetic states in bilayer and trilayer junctions exhibit quantitative agreement with available experimental results [7]. We also discuss limitations in the use of bulk CrI_3 complex band structures to gauge tunneling rates in these ultrathin junctions. The results of this work highlight the dependence of metamagnetic tunneling barrier heights on quantum confinement and interlayer coupling, that may be exploited in magnetic tunnel junctions. Our work is currently published in Physical Review B **101**, 195439 (Ref. [1]) and received a Best Student Finalist Award Poster Presentation at Oak Ridge National Laboratory during the 2019 CNMS User Meeting. Additionally, this work was presented as an oral presentation at the 2019 APS March Meeting.

In 2018, the successful fabrication of few-layer CrI_3 based magnetic tunnel junctions (MTJs) was achieved by Klein et al. (2018). Each device consisted of a graphite/*N*-layer CrI_3/graphite (N = 2, 3, and 4) heterojunction encapsulated by h-BN as illustrated in Fig. 3.1, where layers were sequentially exfoliated from a SiO_2/Si substrate using the stamp-based dry transfer technique (tape) [179]. As discussed in Chapter 1.3.3, a strong external magnetic field was applied to these junctions to suddenly switch the magnetic order (metamagnetic state) of the few-layer CrI_3 channels, altering the electrical resistivity. Tunneling magnetoresistance (TMR) values of 95%, 300%, and 550% were measured in the bilayer, trilayer, and tetralayer junctions, respectively. This original study characterized the change in resistivity using a semiempirical spin filter (barrier) model based on conductance measurements. In addition, the original study provided an electronic band structure calculation; however, the resulting Fermi level resided just above the CrI_3 conduction band edge rather than lying within the CrI_3 band gap (tunneling regime), in contrast to their spin barrier model [7].

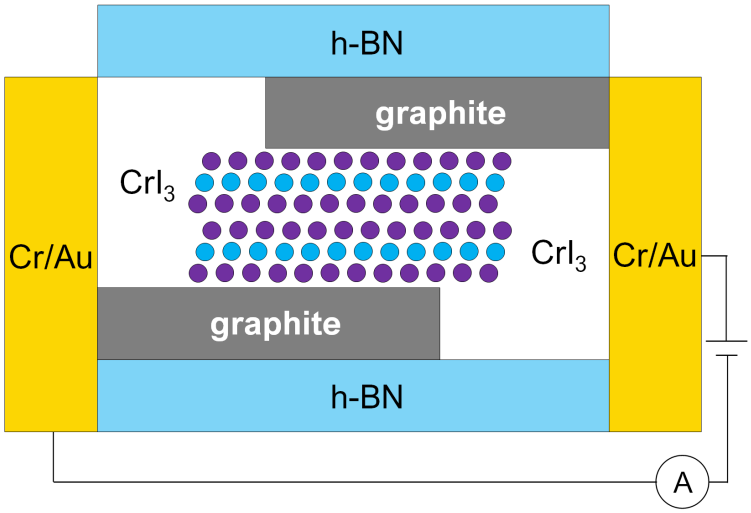

Figure 3.1: Simplified schematic of a graphite/2-layer CrI_3/graphite magnetic tunnel junction [7]. Note that device dimensions are not drawn to scale.

Although promising experiments exist for graphene/CrI_3 MTJs [7], nonetheless, a quantitative link between the heterostructure composition and experimental observations is still missing. For instance, previous calculations fail to explain the observed tunneling-dominated regime as the CrI_3 majority bands cross the graphite leads' Fermi energy [7]. Furthermore,

spin filter models proposed to describe these experiments treat layers as independent and cannot capture quantum confinement effects [180, 181]. Recent work using DFT calculations has shown that 3,000% tunneling magnetoresistance can be attained in CrI_3 based tunnel junctions using Cu leads [182]. However, comprehensive studies examining the composition and magnetic configuration dependence of spin transport properties in these junctions are still missing. For example, the small Fermi surface of graphene leads and quantum confinement are expected to alter these responses. Hence, atomistic descriptions accounting for layer interactions, electrodes, and external fields are required to not only understand and control the mechanisms governing spin transport in these systems [183, 184], but also to design complex heterostructures based on 2D materials [32] exploiting the spin degree of freedom.

3.2 Crystal Structures

The systems considered here are formed by CrI_3 junctions and few-layer graphene electrodes. The magnetic tunnel junction supercells consist of up to three CrI_3 layers arranged by ABC stacking [13]. The epitaxy of these cells accommodates 1×1 CrI_3 layers on $\sqrt{7} \times \sqrt{7}$ graphene where the in-plane lattice constant is set to that of the CrI_3 ($a \approx 6.79$ Å), yielding a 4% lateral tensile strain applied to the few-layer graphene electrodes. By applying strain to the semimetal leads, we ensure the preservation of the CrI_3 band structure (see Fig. 3.7). In order to diminish thickness dependent dispersion found in Bernal stacking [180, 185] and avoid band splitting, graphene layers are turbostratically stacked (rotated every other layer) AB_θ (θ = 21.79^o) to form few-layer graphene electrodes[186, 187, 188], as illustrated in Fig. 3.2. By effectively decoupling the graphene layers through the use of turbostratic stacking, we find that three graphene layers on each side of the junction suffice as the leads, which reduces computational costs. Additionally, periodic boundary conditions are assumed in all three dimensions. The equilibrium configurations for the graphene/CrI_3 heterojunctions are obtained by holding the in-plane lattice constant a fixed while allowing the out-of-plane lattice parameter c of the entire supercell and all atoms to fully relax. Note that these vdW materials are not constrained by conventional epitaxies in practice, rather, these are computational limitations.

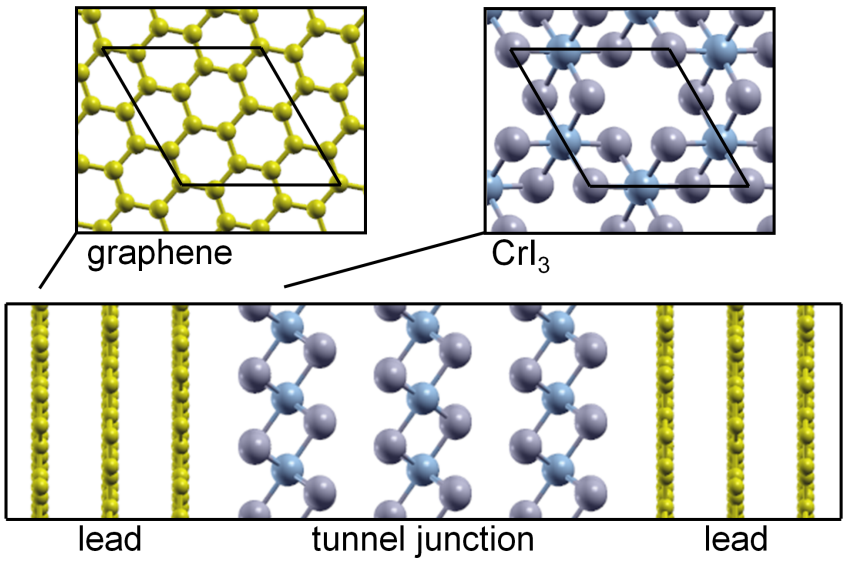

Figure 3.2: Schematic of the supercells: (1×1)-CrI_3/$(\sqrt{7} \times \sqrt{7})$-graphene leads. Solid lines in the different cross-sections mark the unit cell of each layer.

In addition to the computational details described in Chapter 2.5, the 2D Brillouin zone (2D-BZ) is sampled using a 6×6 Monkhorst-Pack mesh [189], where BZ integration is performed using Methfessel-Paxton first-order spreading [190]. Quantum transport calculations are performed using the transportPAO code [191, 192] which allows efficient sampling of the 2D-BZ by producing tight-binding models from the projection of plane-wave pseudopotential wave-functions onto atomic orbitals. For these transport calculations, a turbostratically stacked bilayer of graphene serves as the bulk leads. The convergence thresholds of total energy and forces for ionic minimization is set to their default values of 1.0×10^{-4} Ry and 1.0×10^{-3} Ry$\cdot a_0^{-1}$, respectively. The convergence threshold for self-consistent calculations are set to their default of 1.0×10^{-6} Ry.

The resulting interlayer distances between adjacent CrI_3 layers is approximately 6.44 Å regardless of the system's magnetic configuration while graphene/CrI_3 separations are around 3.54 Å, in good agreement with other studies [13, 182, 193]. For the sake of comparison, atomic structure relaxations of CrI_3 junctions enclosed by AB stacked 3×3 graphene leads with large (9%) compressive strain, explored by a previous study [7], are performed as well.

Unlike graphene/CrI_3 systems with moderate tensile strain that exhibit flat and pristine crystalline interfaces, systems with large compressive strain applied to the graphene leads produce significant buckling in the graphene layers with standard deviations of 0.3 Å as seen in Fig. 3.3.

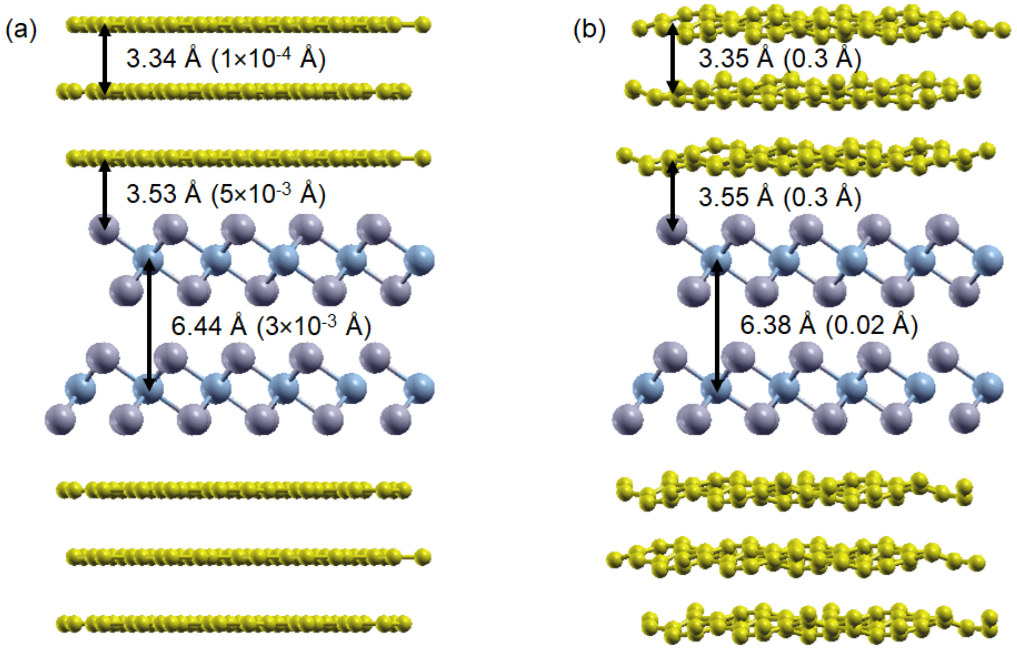

Figure 3.3: (a) Schematic of bilayer CrI_3 junction between $\sqrt{7} \times \sqrt{7}$ turbostratic stacked graphene leads. All layers appear flat with standard deviations – indicated in parenthesis – of $3{\times}10^{-3}$ Å and up to $5{\times}10^{-3}$ Å for CrI_3 and graphene layers, respectively (similar results for $\sqrt{7} \times \sqrt{7}$ AB stacked graphene leads). (b) Schematic of bilayer CrI_3 junction between $3{\times}3$ AB stacked graphene leads. The CrI_3 layers appear flat but the graphene layers display buckling with standard deviations around 0.3 Å.

3.3 Band Structures of Isolated Few-Layer CrI_3

First, the electronic band structures of isolated monolayer, bilayer, and trilayer CrI_3 in several non-equivalent metamagnetic configurations for multilayer structures are analyzed. Note that a bilayer of CrI_3 provides a parallel $\uparrow\uparrow$ (spins in both layers are aligned) and an antiparallel $\uparrow\downarrow$ (spins in each layer oppose each other) magnetic state while the trilayer structure provides a parallel $\uparrow\uparrow\uparrow$ and two antiparallel ($\uparrow\uparrow\downarrow$ and $\uparrow\downarrow\uparrow$) magnetic states. The supercell of each structure includes at least 15 Å of perpendicular vacuum space relative to the CrI_3 plane in order to mitigate the effects of periodic boundary conditions. In order to visualize each layer's contribution to the overall electronic structure, atomic projections for each CrI_3 layer are superimposed on

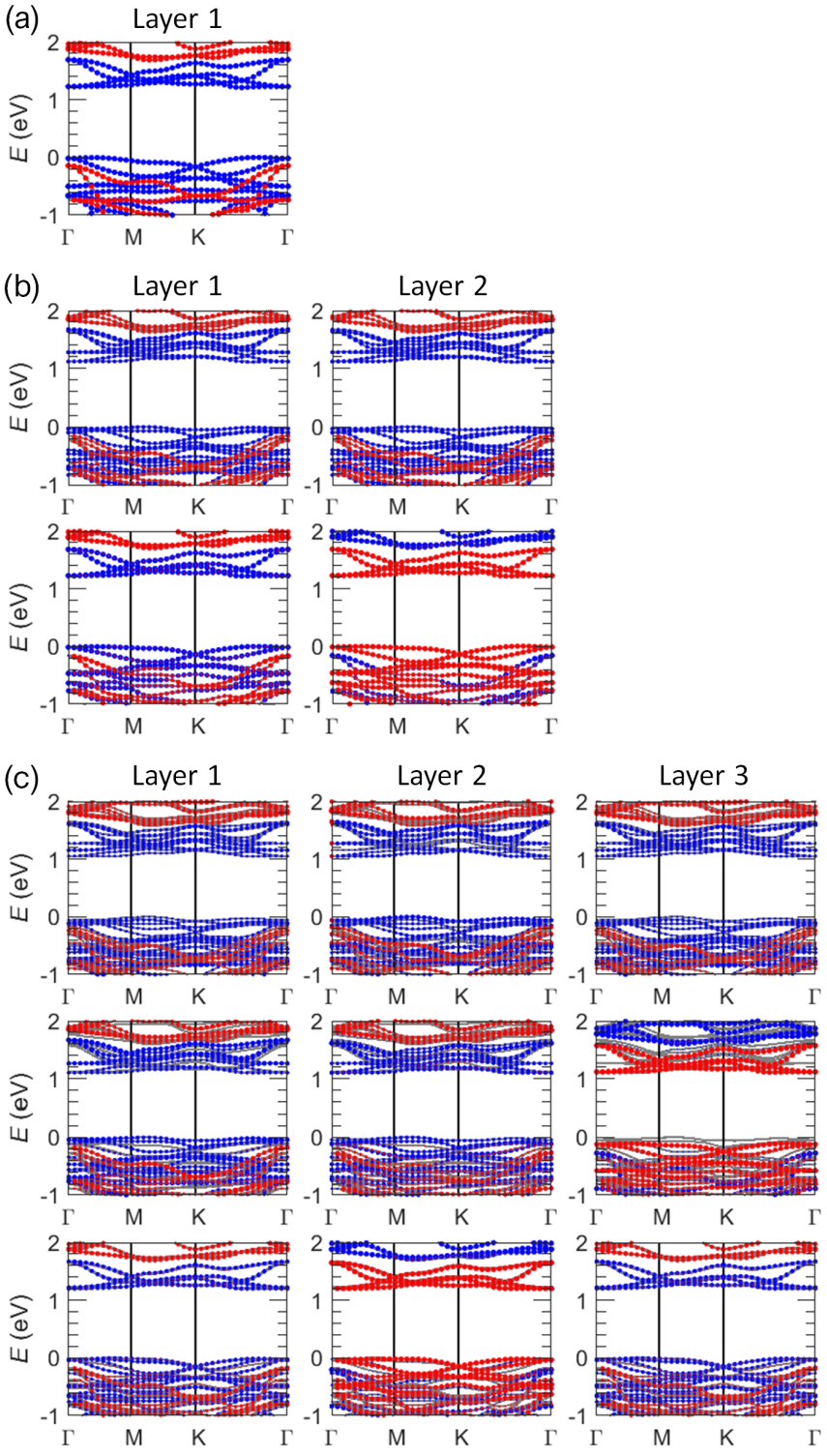

Figure 3.4: (a) Electronic band structure of an isolated monolayer of CrI_3. (b) Electronic band structure of an isolated bilayer of CrI_3 for ↑↑ (top) and ↑↓ (bottom) metamagnetic configurations. (c) Electronic band structure of an isolated trilayer of CrI_3 for ↑↑↑ (top), ↑↑↓ (middle), and ↑↓↑ (bottom) metamagnetic configurations. Decomposition based on projections onto localized atomic orbitals on each of the layers for both spin majority (blue) and minority (red) are plotted (left to right).

the band structures for both spin majority (blue) and minority (red) as seen in Fig. 3.4. This is achieved by projecting the Bloch states (eigenfunctions) $\psi_{n'}(k)$ onto pseudo-atomic orbitals ϕ^{α}_{nlm}, which produces momentum-resolved projections:

$$|c^{\alpha}_{n'nlm}(k)|^2 = \ | < \psi_{n'}(k) \mid \phi^{\alpha}_{nlm} > |^2 \tag{3.1}$$

where α denotes the species, n' denotes the band index while n, l, and m represent the orbital quantum numbers [194, 195]. The size of the projection markers in Fig. 3.4 are scaled based on the summation of all atomic projections constituting each CrI_3 layer for every k-point along the paths of symmetry. Based on these band decompositions, the electronic states from one CrI_3 layer to the next are nearly identical in ferromagnetic (FM) systems. For systems with antiparallel configurations, the spin majority and minority states switch sites from one magnetic layer to an opposing magnetic layer. Consistent with experiments [13, 196], monolayer and antiparallel ($\uparrow\downarrow$ and $\uparrow\downarrow\uparrow$) few-layer CrI_3 band gaps are roughly 1.2 eV. Regarding the alternative magnetic configurations ($\uparrow\uparrow$, $\uparrow\uparrow\uparrow$, and $\uparrow\uparrow\downarrow$), band gaps appear dependent upon the metamagnetic state. FM trilayer CrI_3 produces a band gap roughly 0.2 eV smaller than the monolayer and roughly 0.1 eV smaller than the FM bilayer system. Consistent with prior DFT studies [197, 198, 199] yet contrary to experimental observations, we find that the $\uparrow\uparrow\uparrow$ ($\uparrow\uparrow$) configuration is 34 meV (18 meV) lower than the $\uparrow\downarrow\uparrow$ ($\uparrow\downarrow$) state for trilayer (bilayer) structures [7, 200].

3.4 Band Structures of Graphene/CrI_3 Heterostructures

Similarly, the electronic band structures of few layer CrI_3 based MTJ's in several metamagnetic configurations are computed and decomposed onto atomic orbitals localized on different magnetic layers and colored according to their spin population (blue, majority; red, minority). In this study, we primarily focus on turbostratic (rotational) stacking of semimetal graphene leads as opposed to highly oriented AB stacking. Regardless of graphene stacking (turbostratic or AB) in the $\sqrt{7} \times \sqrt{7}$ leads, single layer CrI_3 within graphene/CrI_3 heterojunctions produces

nearly identical band gaps to that of the isolated case as seen in Figs. 3.5 and 3.4(a), respectively. Furthermore, the graphene Dirac point (DP), easily identifiable at the supercell's K-point for this epitaxy, resides within the CrI_3 band gap. Unlike the turbostratically stacked leads which preserve the linear dispersion of graphene by limiting interlayer interactions, AB stacked electrodes produce parabolic band dispersion which is dependent upon lead thickness as seen in Fig. 3.5(b) [180, 185].

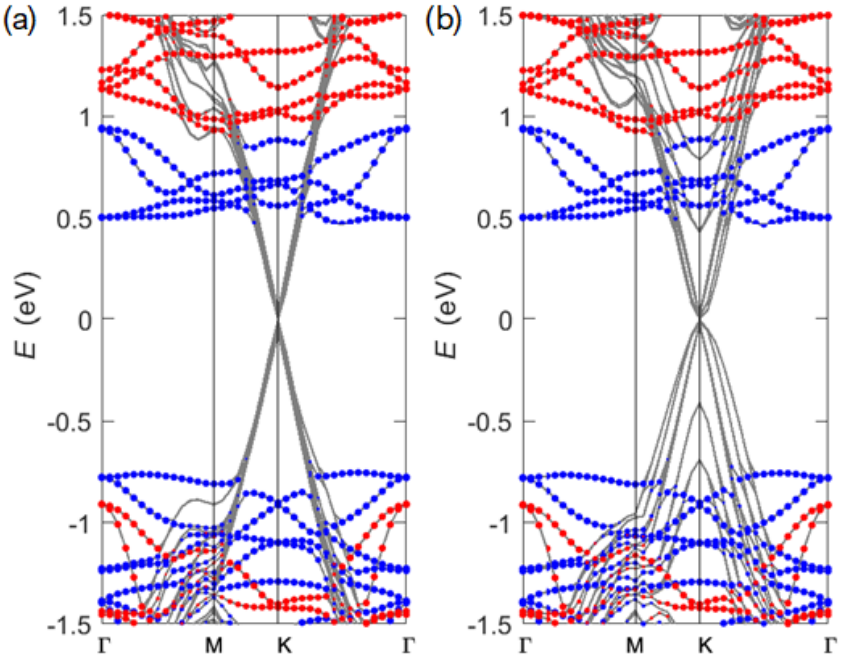

Figure 3.5: (a) Electronic band structure of monolayer CrI_3 between (a) $\sqrt{7} \times \sqrt{7}$ turbostratic and (b) AB stacked graphene leads where atomic projections for both spin majority (blue) and minority (red) are plotted.

The bilayer CrI_3 MTJ with $\sqrt{7} \times \sqrt{7}$ graphene leads produces similar band alignments to the monolayer case as seen in Fig. 3.6(a). However, bilayer MTJs display metamagnetic dependent CrI_3 band gaps similar to the isolated bilayer case, where the band gaps differ by roughly 0.1 eV between antiparallel and parallel configurations. By introducing highly compressed 3×3 AB stacked graphene leads, used in a prior study [7], the Dirac point of graphene lies at the conduction band edge of CrI_3 [Fig. 3.6(b)]. These band alignments are contrary to experimental observations that exhibit electron tunneling due to Schottky contacts [7], cases where the graphene Dirac point resides below the conduction band edge of CrI_3. To further investigate the effects of strain on a graphene/CrI_3 junction, compressive strain is applied to the

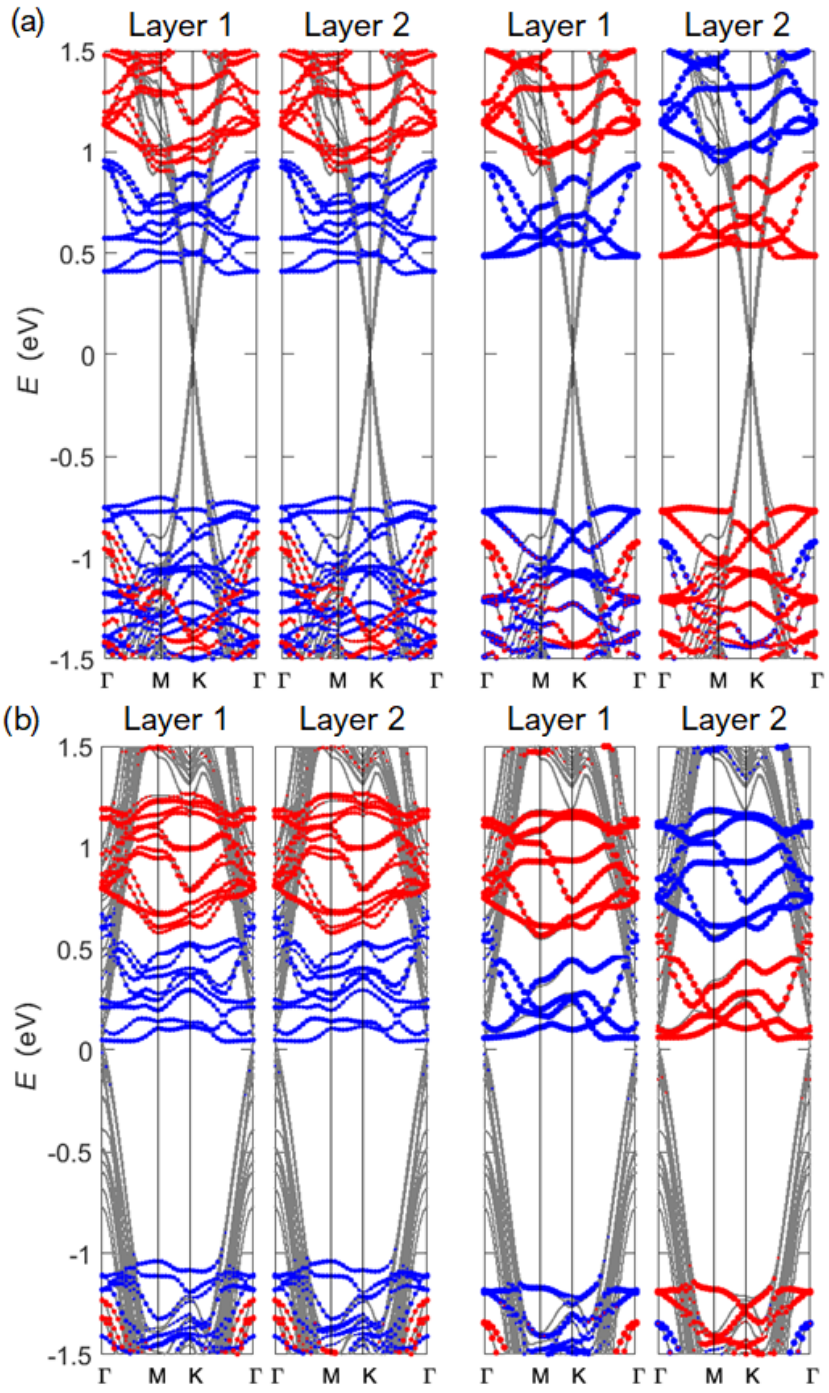

Figure 3.6: (a) Electronic band structure of bilayer CrI_3 between $\sqrt{7}\times\sqrt{7}$ turbostratic graphene leads for $\uparrow\uparrow$ (left) and $\uparrow\downarrow$ (right) metamagnetic configurations. (b) Electronic band structure of bilayer CrI_3 between 3×3 AB stacked graphene leads for $\uparrow\uparrow$ (left) and $\uparrow\downarrow$ (right) metamagnetic configurations. Atomic projections for both spin majority (blue) and minority (red) are plotted for each layer.

CrI_3 layer itself rather than the graphene electrode material. The compression of the CrI_3 layer produces distortions in the CrI_3 band structure and a small reduction of the band gap (Fig. 3.7).

As shown in a prior study [201], reduction in the CrI_3 band gap due to compressive strain is caused by small downward energy shifts in Cr d-states and hybridization of the I p-states.

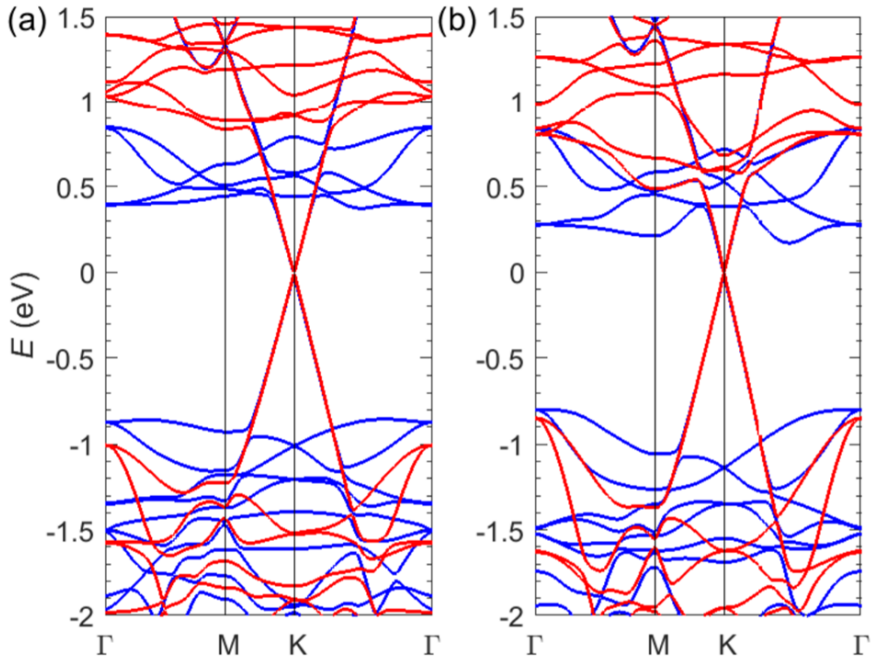

Figure 3.7: Electronic band structure of monolayer CrI_3/monolayer $\sqrt{7} \times \sqrt{7}$ graphene with (a) total tensile strain on graphene ($a = 6.79$ Å for the supercell) and with (b) total compressive strain on CrI_3 ($a = 6.51$ Å for the supercell). In these band structures, the spin majority (minority) are represented in blue (red).

Similar to the monolayer and bilayer junctions, results for the 2D band structures of trilayer CrI_3 MTJs with different metamagnetic states (Fig. 3.8) indicate that tunneling is the governing transport mechanism in the magnetic junctions. In all cases, the Fermi level (E = 0), located at the tip of the Dirac cone, lies between the CrI_3 conduction and valence bands. The few-layer CrI_3 band gaps (Fig. 3.8) are comparable to both experimental and DFT+U values [202, 203, 200, 196]. Moreover, bulk CrI_3 electronic dispersion and graphene/CrI_3 band alignments attained using a pseudohybrid Hubbard density functional (ACBN0) are similar to those of DFT alone [Fig. 3.9(b)-(e)] [154]. Yet other approaches beyond DFT [Fig. 3.9(a)] predict larger gaps [193, 204] that may impact the resulting transmissions probabilities and related quantities (TMR and polarization) in these systems. We also point out that the parallel metamagnetic configurations appear to be more stable than the antiparallel ones. For instance, the ↑↑↑ (↑↑) system is 23 meV (12 meV) lower than ↑↓↑ (↑↓) counterpart for trilayer (bilayer) systems.

Despite being consistent with previous works within DFT [197, 198, 199], experimental measurements found that the antiferromagnetic state is the most stable in few-layer CrI_3 [7, 200], which remains an open question.

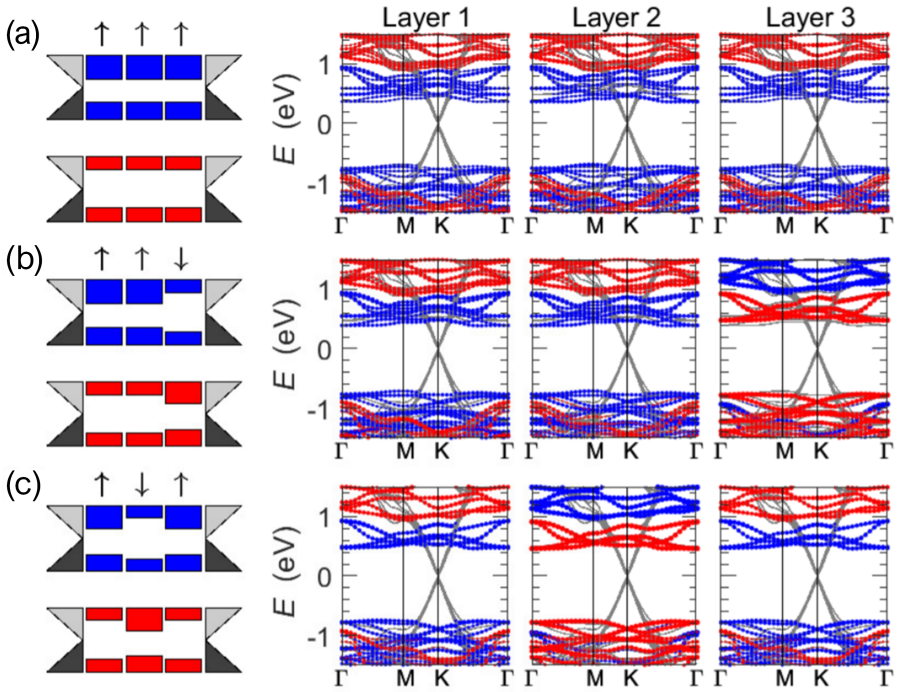

Figure 3.8: Band diagrams and corresponding band structures in trilayer graphene/trilayer CrI_3/trilayer graphene junctions for various metamagnetic states: (a) ↑↑↑ state; (b) ↑↑↓ state; and (c) ↑↓↑ state. In each subpanel, Bloch states are projected onto localized atomic orbitals of different CrI_3 layers in the MTJ, allowing the band alignments to be identified for the spin majority (blue) and minority (red) populations. In all cases, graphene electrodes preserve the linear dispersion of the monolayer (no gap) and the Fermi level resides within the band gap of CrI_3, demonstrating that tunneling transport is the dominant mechanism.

While the coupling between layers does not form gap states at the graphene/CrI_3 interface, it is sufficient to alter field-modulated transport. We exemplify this using the trilayer CrI_3 case (Fig. 3.8) that offers three different metamagnetic states (↑↑↑, ↑↑↓ and ↑↓↑) which yield more diverse tunneling resistances than configurations in the bilayer junctions (↑↑ and ↑↓). In the case of the parallel trilayer configuration (↑↑↑), the obtained band gap for the spin majority (minority) is approximately 0.05 eV (0.02 eV) smaller than the parallel bilayer configuration and 0.17 eV (0.07 eV) smaller than the monolayer. Similar to other layered systems [181, 205], we find that band gaps depend on thickness although not as strongly as in transition metal dichalcogenides.

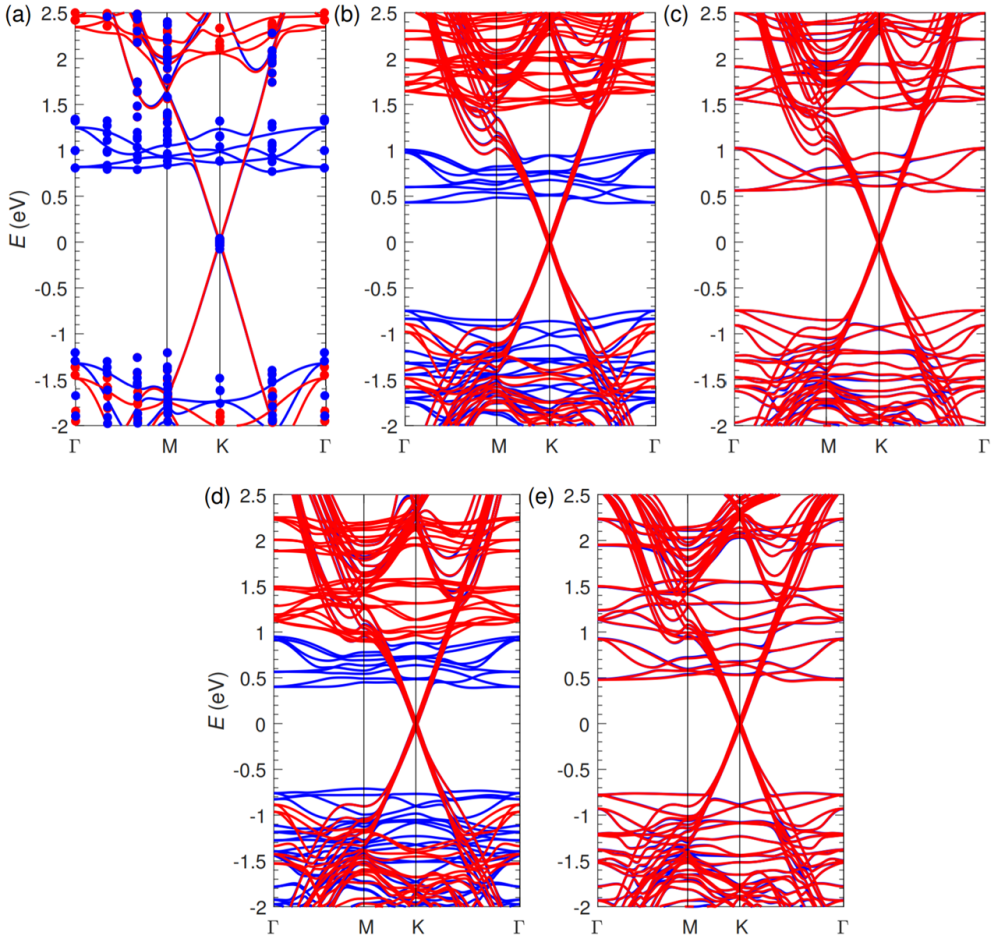

Figure 3.9: (a) Band structure of the monolayer graphene/monolayer CrI_3 HSE calculation ($\alpha = 0.25$). For comparison, the HSE results of the full bilayer CrI_3/graphene junction in the ↑↑ metamagnetic state (circles) is also plotted. (b) Band structure of bilayer CrI_3/graphene junction in the ↑↑ state using ACBN0 ($U_{eff}^{Cr} = 0.9$ eV, $U_{eff}^{I} = 1.7$ eV, $U_{eff}^{C} = 3.0$ eV) and (c) in the ↑↓ state using ACBN0 ($U_{eff}^{Cr} = 0.6$ eV, $U_{eff}^{I} = 1.6$ eV, $U_{eff}^{C} = 3.0$ eV). (d) Band structure of bilayer CrI_3/graphene junction in the ↑↑ state using PBE and (e) in the ↑↓ state using PBE for both spin majority (blue) and minority (red).

Notwithstanding the weak thickness dependence, external magnetic fields allow for the modulation of band alignments, as depicted in Fig. 3.8. For large magnetic fields, interlayer coupling is strengthened when the magnetization of all CrI_3 layers is parallel, forming smaller band gaps (tunneling barriers) than in cases where the magnetization of adjacent layers is opposite. As magnetic fields diminish and one of the layers flips its magnetization, band gaps exhibit an increase, which varies depending on the metamagnetic state. For instance, the conduction band edge of the CrI_3 spin majority population in the ↑↑↓ configuration is sensibly closer to the Fermi level than in the ↑↓↑ case as a result of the stronger magnetic coupling between the

first two layers [199]. Interlayer coupling, albeit weak, precludes junctions with the same total magnetization ($|M| = 6\mu_B$ per layer) yet different magnetic ordering from being treated as equivalent spin barriers, as illustrated by schematics found in Fig. 3.8. Consequently, the effects of non-equivalent spin barriers is later manifested in transport calculations.

3.5 Ballistic Transport

In order to characterize quantum transport in these junctions, the conductance is computed from the transmission probability of states in the few-layer graphene leads through the scattering region containing the 2D magnetic junction. *A priori*, transport across junctions is ballistic and occurs mainly via tunneling [206] as thermionic-field emission [207, 208] appears to be negligible. Due to experimental conditions corresponding to the spin transport measurements ($T \sim 4$ K and high-quality junctions), contributions from phonons or spin-flip mechanisms are omitted. In this context, zero-bias conductance per unit area (which accounts for the present metal electrodes) is computed from the transmission probability following Landauer's formalism [166, 167, 168] defined in Eq. 2.22 where $G_0/A \approx 97$ S/μm^2. The transmission probability $T_s^m(E)$ corresponding to a spin channel s ($\uparrow$ or $\downarrow$) for the system in a metamagnetic state m is calculated according to Eq. 2.23. Note that thermionic emission of either electrons or holes as well as tunneling or hopping mechanisms are implicit in Eq. 2.23.

Tunneling current in these systems is a combination of available states in the electrodes and their tunneling probability. In Fig. 3.10, we plot the spin and momentum resolved transmission probability $t_s^m(\mathbf{k}_\parallel, E)$ found in Eq. 2.23 for the trilayer CrI_3 in metamagnetic states ($\uparrow\uparrow\uparrow$, $\uparrow\uparrow\downarrow$, and $\uparrow\downarrow\uparrow$) that produce distinct tunneling currents. It is important to note that due to the peculiar dispersion of graphene, contributions to transport around the Fermi energy originate in a small portion of reciprocal space near the K-point, requiring high k-point sampling. These transport calculations are then sampled using a fine $\mathbf{k}_\parallel$-grid (120×120) [191, 192]. In all cases, this low density of states in the electrodes unpropitiously yields low conductance values. Net transmissions increase as the energy moves away from the Dirac point due to the expanded circular Fermi contour of the graphene electrodes. These enhancements are asymmetric because the CrI_3 conduction bands reside closer to the Fermi level than the valence bands. As

a result, net transmissions significantly increase at higher energies, consistent with recent experiments that employ dual-gated graphene/CrI_3 devices which augment carrier concentrations within the graphene electrodes [203, 107, 209]. We note that the absence of threefold rotation near the K-point is likely due to spatially dependent interactions at the graphene/CrI_3 interfaces [210, 211, 212].

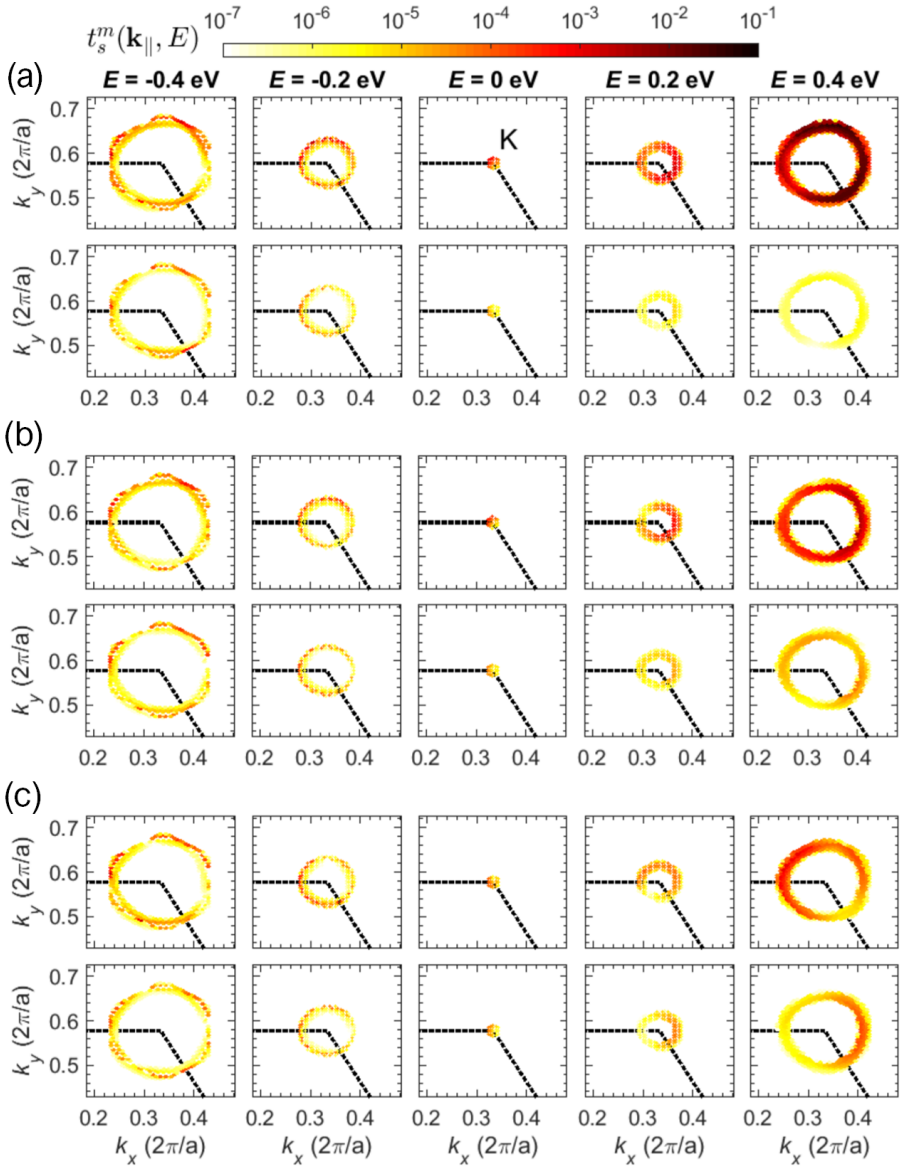

Figure 3.10: Spin and momentum-resolved transmission profiles [$t_s^m(\mathbf{k}_\parallel, E)$] near the supercell K-point for trilayer CrI_3 between graphene leads for several metamagnetic states: (a) ↑↑↑; (b) ↑↑↓; and (c) ↑↓↑. In each set of plots, the top (bottom) row corresponds to the spin majority (minority) channel and columns (from left to right) correspond to energies E = -0.4, -0.2, 0.0, 0.2 and 0.4 eV. The dashed line denotes a corner of the hexagonal Brillouin zone. Logarithmic scale is provided on top.

At fixed energies, transmission profiles show a strong dependence on the metamagnetic state m, even if they have the same total magnetization. The ↑↑↑ case shows the strongest (weakest) transmission for the spin majority (minority). As one of the layers flips its magnetization, the transmissions of spin populations change differently depending on the location of the layer with opposite magnetization. The ↑↑↓-configuration exhibits a larger transmission than the ↑↓↑ case due to smaller spin majority barriers (band gaps) produced in the first two layers through the enhanced coupling between the adjacent layers [Fig. 3.8(b)].

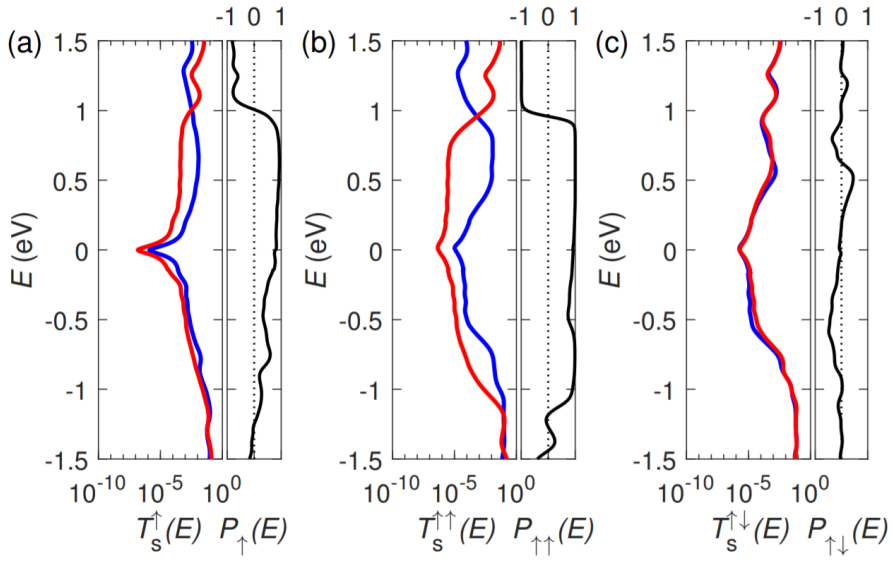

Figure 3.11: Transmission probabilities (left) and the spin polarization in the current (right) for (a) monolayer CrI_3, (b) bilayer CrI_3 in the ↑↑ metamagnetic configuration, and (c) bilayer CrI_3 in the ↑↓ metamagnetic configuration between $\sqrt{7} \times \sqrt{7}$ turbostratic graphene leads for spin majority (blue) and minority (red).

Next, the net transmissions T_s^m through CrI_3 MTJs as a function of the electron energy for non-equivalent metamagnetic configurations m are produced. We apply Fermi-Dirac smoothing to all transmission curves with a broadening term of k_BT = 0.01 eV. For monolayer and bilayer junctions, transmissions for both spin up (blue) and down (red) channels exhibit a dip near the Fermi level. This reduction, due to the vanishing DOS in graphene [213], is overcome when carrier energies move toward the CrI_3 band edges. Due to the inequivalent spin barriers present in the monolayer or parallel bilayer MTJ, spin minority tunneling current is significantly lower than the spin majority current for energies within the CrI_3 band gap. Contrarily,

comparable spin minority and majority currents are seen in the antiparallel bilayer MTJ, where charge carriers encounter similar spin barriers [Fig. 3.11].

For a given metamagnetic state m, we also compute the spin polarization of the tunneling current as:

$$P_m = \frac{T_\uparrow^m - T_\downarrow^m}{T_\uparrow^m + T_\downarrow^m}. \tag{3.2}$$

A high spin polarization is attained for the the monolayer ($P_\uparrow \approx 0.79$) and parallel bilayer configuration ($P_{\uparrow\uparrow} \approx 0.92$) while a near zero spin polarization is attained for the antiparallel bilayer MTJ ($P_{\uparrow\downarrow} \sim 0$) at the Fermi level as seen in Fig. 3.11. Note that systems which demonstrate high spin polarization in the tunneling current behave as efficient spin filters [184]. Due to asymmetry between the graphene/CrI_3 interfaces on both sides of the antiparallel bilayer junction, nonzero polarization is observed close to the CrI_3 band edges [Fig. 3.11(c)].

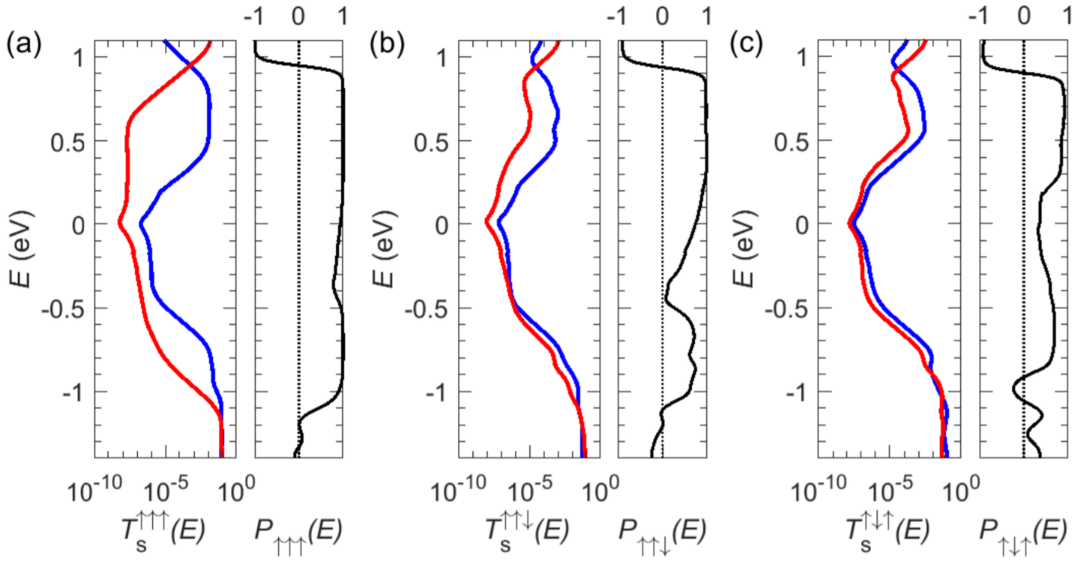

Figure 3.12: Transport analysis of trilayer CrI_3 tunneling junctions in different metamagnetic states: (a) ↑↑↑, (b) ↑↑↓, and (c) ↑↓↑. For each case, we plot (from left to right) the transmission $T_s^m(E)$ in logarithmic scale; the polarization of the tunneling current; and the bulk CrI_3 CBS along the tunneling direction for both spin majority (blue) and minority (red) carriers.

The net transmissions T_s^m through trilayer CrI_3 junctions for the three metamagnetic configurations m are produced in Fig. 3.12. Like the monolayer and bilayer cases, the parallel trilayer junction produces the highest spin polarization in the tunneling current. Consistent with the profiles in Fig. 3.10, the difference between the spin majority and minority tunneling probabilities shrinks when more adjacent layers have opposite magnetization. Near the

Fermi level and within the band gap, the strong polarization of the spin current through the parallel configuration ↑↑↑ ($P_{\uparrow\uparrow\uparrow} \approx 0.94$) diminishes as one of the layers flips its magnetization ($P_{\uparrow\uparrow\downarrow} \approx 0.73$ and $P_{\uparrow\downarrow\uparrow} \approx 0.35$). We note that spin current in these last two configurations remains polarized due to the odd number of CrI_3 layers.

3.6 Complex Band Structures

In MTJ's, the energy dependent decay rates of evanescent wave functions can be estimated from the junction's complex band structure (CBS) [183, 184]. For the different magnetic configurations of the trilayer case, we compute the bulk CrI_3 CBS along the Γ-A, M-L, and K-H directions, all perpendicular to the 2D plane (imaginary and real). In order to compute the CBS of the antiparallel (↑↓↑) configuration, we use a six layer supercell (↑↓↑↓↑↓) to avoid unintended stacking (↑↓↑↑↓↑) due to the periodic boundary conditions. Note that band alignments in the bulk CBS are set to reflect those obtained in graphene/CrI_3 junctions (Fig. 3.13). For all metamagnetic configurations and symmetry points, we notice that the slowest decaying evanescent states for spin majority and minority populations exhibit weak energy dependence near the middle of the band gap and substantial dependence close to the band edges. Furthermore, spin majority evanescent states in ferromagnetic (↑↑↑) CrI_3 decay slower than the spin minority states within the gap along the M-L and K-H directions due to their shorter (less negative) decay constants κ, enabling greater spin majority tunneling.

We find that trilayer MTJ net transmission curves as shown in Fig. 3.12 deviate from the bulk CrI_3 CBS along the K-H direction. Due to the $(\sqrt{7} \times \sqrt{7})$-graphene/$(1 \times 1)$-$CrI_3$ epitaxy found in the trilayer junctions, graphene states reside about the K-point. Although spin majority transmissions seen for the junction (↑↑↑ configuration) resemble the slowest decaying spin majority evanescent states in bulk CrI_3 in the ↑↑↑ configuration, spin minority transmissions are fairly different to those of the spin minority within the band gap while exceptionally different near the band edges (Fig. 3.12). The use of the CBS to estimate decay rates for few-layer CrI_3 channels poses important limitations which we attribute to size effects as well as coupling to the electrodes [214] in these ultrathin junctions. For instance, the CBS of the antiparallel configuration should *a priori* yield a tunneling current with no spin polarization. However,

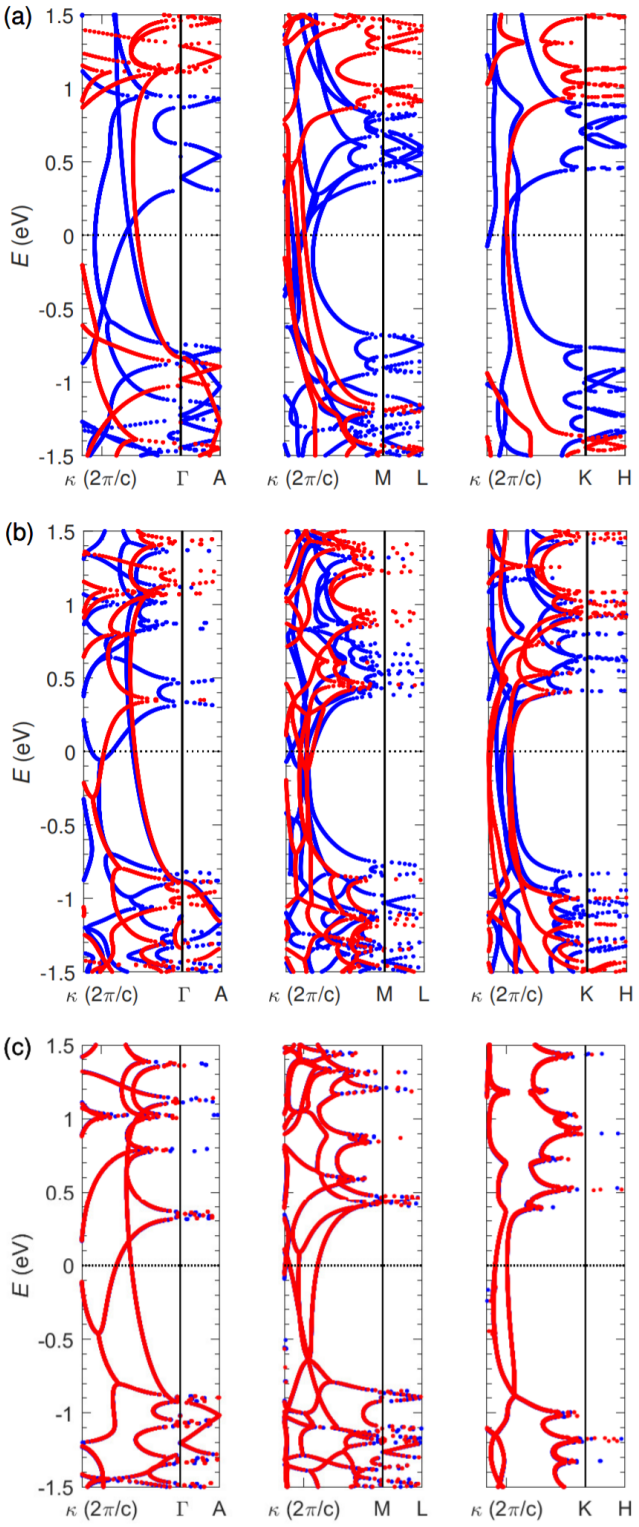

Figure 3.13: Complex band structures for bulk ABC stacked CrI_3 in (a) ↑↑↑, (b) ↑↑↓, and (c) ↑↓↑ metamagnetic configurations for spin majority (blue) and minority (red). Different subpanels correspond to different symmetry points perpendicular to the basal plane of CrI_3 (left to right): Γ-A, M-L and K-H. The unit cell used for the ↑↓↑ state contains 6 layers (↑↓↑↓↑↓).

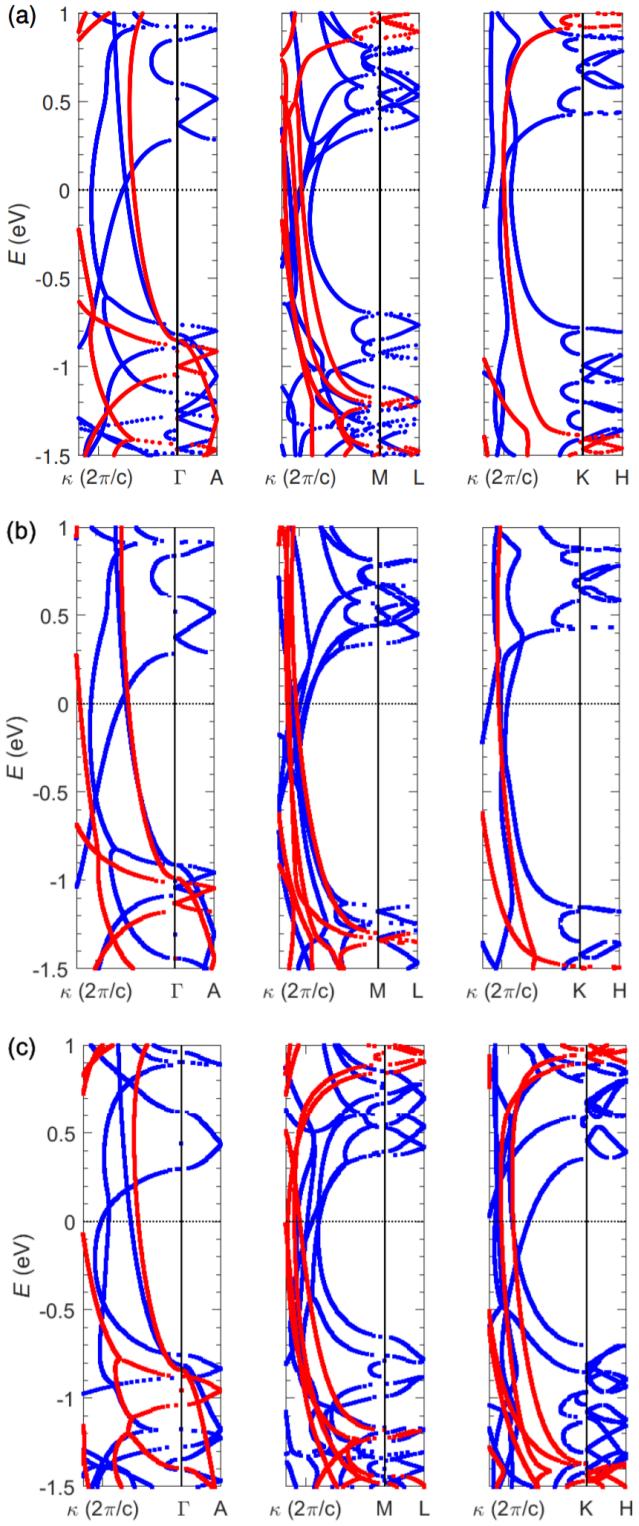

Figure 3.14: Spin-dependent complex band structure of (a) ABC stacked CrI_3, (b) ABC stacked CrI_3 using GGA+U ($U_{eff}^{Cr} > 6$ eV), and (c) AB stacked CrI_3 at symmetry points of hexagonal lattices: Γ, M and K, where blue (red) lines correspond to the spin majority (minority) for the parallel metamagnetic states (↑↑↑ and ↑↑).

when the system has an odd number of layers in the antiparallel configuration, the CrI_3 net magnetization is nonzero and, in return, a spin-polorized current is produced [Fig. 3.12(c)].

Although our electronic band structure calculations appear to be in agreement with experiments [13, 196], local approximations within DFT commonly underestimate band gaps [138, 149]. In order to address this, we compute bulk CrI_3 CBS derived from a GGA+U approach which yields comparable complex wave-vectors to conventional PBE near the junction's Fermi level [Fig. 3.14(b)], suggesting minor corrections to our results. By artificially expanding the CrI_3 band gap by applying a substantial effective Hubbard term to the Cr atoms, we demonstrate that evanescent states close to the majority conduction band edge are largely preserved, regardless of the formation of larger majority and minority band gaps in CrI_3.

Lastly, in order to investigate the effects of quantum confinement (size effects) on the evanescent states of bilayer systems, we examine the CBS of bulk CrI_3 with the alternative AB stacking order. The supercell of bulk CrI_3 with AB stacking is comprised of two CrI_3 layers. Based on the results of AB stacked CrI_3 as seen in Fig. 3.14(c), we find deviations between the CBS of bulk CrI_3 with alternate stacking orders. Complex wave-vectors relative to the K-point differ significantly in conventional ABC stacked CrI_3 compared to AB stacked structures, where an even greater disparity exists between spin majority and minority complex wave-vectors close to the band edges. As a result, spin majority transmission in AB stacked CrI_3 are expected to be greater about the K-point compared to standard ABC stacked CrI_3.

3.7 Tunneling Magnetoresistance

The tunneling magnetoresistance (TMR) for an arbitrary metamagnetic state m is defined:

$$\text{TMR}_m = \frac{\sigma^m - \sigma^{AP}}{\sigma^{AP}} \tag{3.3}$$

$$= \frac{(T_\uparrow^m + T_\downarrow^m) - (T_\uparrow^{AP} + T_\downarrow^{AP})}{T_\uparrow^{AP} + T_\downarrow^{AP}}, \tag{3.4}$$

where the antiparallel (AP) configurations correspond to the $\uparrow\downarrow$ and $\uparrow\downarrow\uparrow$ states for the bilayer and trilayer cases, respectively. Magnetoresistances based on the parallel configurations determined in this study ($\text{TMR}_{\uparrow\uparrow} \approx 170\%$ and $\text{TMR}_{\uparrow\uparrow\uparrow} \approx 350\%$) are in good agreement with

experiments ($TMR_{\uparrow\uparrow} \approx 95\%$ and $TMR_{\uparrow\uparrow\uparrow} \approx 300\%$) [7]. A difference in tunneling magnetoresistance ($TMR_{\uparrow\uparrow\downarrow} \approx 70\%$) is evident between the two antiparallel states with the same net magnetization, $\uparrow\uparrow\downarrow$ and $\uparrow\downarrow\uparrow$ (Fig. 3.15), which we associate to the increase in conductance observed experimentally at intermediate fields ($TMR_{\uparrow\uparrow\downarrow} \sim 50\%$) [7]. Thereby, these variations in effective spin barriers may provide a method to probe the dynamics of metamagnetic configurations in the system during the switching process via external fields. The TMR increase for energies above the Fermi level is due to an enhanced transmission of Bloch states near the conduction band edge of CrI_3. This phenomenon allows for the modulations of the TMR by a few orders of magnitude as recently demonstrated in dual-gated TMJ's [203, 107, 209]. Overall, weak layer-layer coupling plays a crucial role regarding electron transport prediction and intermediate state identification in these 2D layer channels.

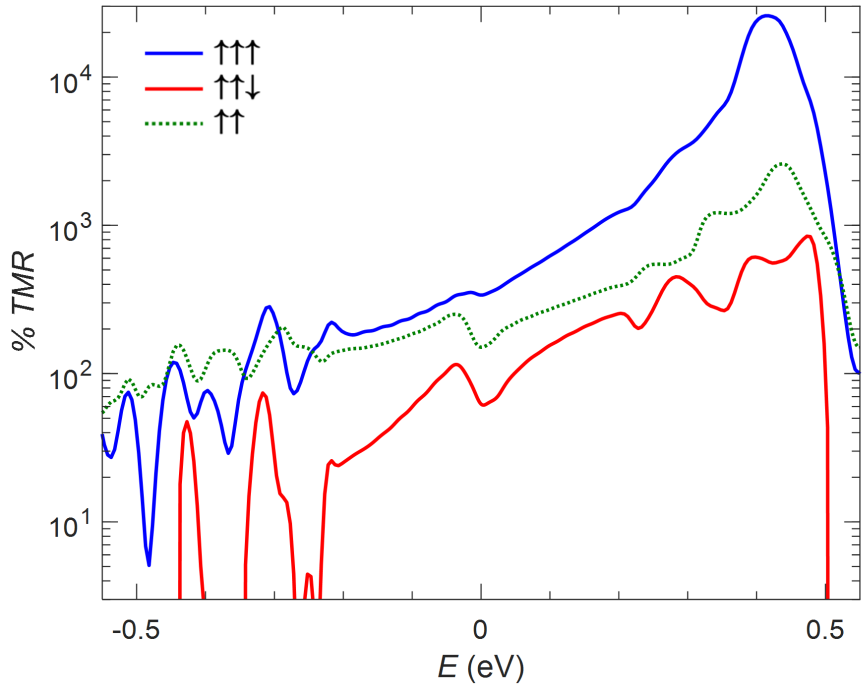

Figure 3.15: Tunneling magnetoresistances [Eq. 3.4] for graphene/CrI_3 MTJs as a function of energy for both trilayer ($TMR_{\uparrow\uparrow\uparrow}$ and $TMR_{\uparrow\uparrow\downarrow}$) and bilayer ($TMR_{\uparrow\uparrow}$) systems.

In order to estimate the TMR of tunnel junctions in different metamagnetic states regardless of epitaxy, the CBS may be employed, provided that the band alignments between junction and electrodes are known. To produce these estimates, we approximate the transmission for a

channel of length L in the metamagnetic state m as:

$$\widetilde{T}_s^m(E) = \frac{A}{(2\pi)^2} \int_{\text{2D}-\text{BZ}} d^2\mathbf{k}_\parallel \sum_i e^{-2\kappa_{i,s}^m(\mathbf{k}_\parallel, E)L}, \tag{3.5}$$

where $\kappa_{i,s}^m(\mathbf{k}_\parallel, E)$ are the imaginary components of the complex bands i at energy E, where all transmission contributions are averaged over the full 2D Brillouin zone. In Fig. 3.16 we compare the TMR for ABC stacked CrI_3 obtained using Eq. 3.5 to the actual values obtained from Landauer's formalism for the graphene/trilayer CrI_3 heterojunction. We note that we obtain comparable estimates for the $TMR_{\uparrow\uparrow\uparrow}$ near the conduction band edge by sampling the full BZ of the complex band structure; however, we observe departures in energy ranges close to the valence band (Fig. 3.16). This suggests that these TMR values may persist for other epitaxies with similar band alignments.

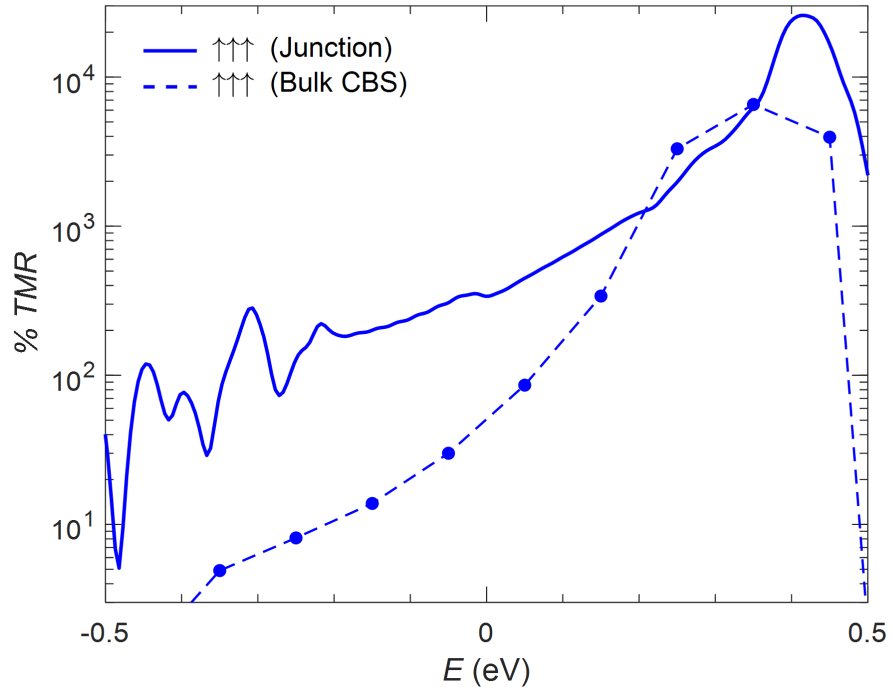

Figure 3.16: A comparison between the $TMR_{\uparrow\uparrow\uparrow}$ in the trilayer CrI_3 junction obtained from the ballistic transmission (solid lines) versus estimates derived from the bulk CBS (dashed line).

Chapter 4

Graphene/CrX_3 Heterojunctions

4.1 Summary and Background

In this chapter, we probe the electronic properties of turbostratically stacked N-layer (N = 1, 2, 3) graphene/CrX_3 (X = F, Cl, Br, I) heterojunctions via first principles calculations within DFT+U, where pseudohybrid Hubbard density functionals are utilized to improve band estimates over conventional DFT. We find that graphene (Gr)/CrX_3 systems with lighter halides promote greater charge transfer from graphene sheets. As the number of graphene layers increase, CrX_3 band gaps slightly shrink while charge screening is observed in the neighboring graphene layers. Furthermore, an increase in graphene layers switches Gr/CrX_3 Ohmic heterojunctions into Schottky contacts, where no external field or strain is required. In regards to Gr/CrF_3 junctions, charge transfer to the CrF_3 layer induces band splitting. Moreover, Bernal stacked Gr/CrF_3 junctions display graphene band gaps of 173 meV and 104 meV in bilayer and trilayer graphene systems, respectively. A portion of this work was uploaded as a presentation at the 2020 APS March Meeting due to its cancellation over the COVID-19 pandemic.

Apart from investigating exotic magnetic tunnel junction materials [215, 216], recent theoretical studies have explored alternative metal interfaces [182, 217] or 2D material insertion (vdW engineering) [218, 219] in metal/CrX_3 (X = Br, I) heterojunctions to modify device properties such as tunneling magnetoresistance (TMR). Although a number of theoretical studies exist that attempt to characterize graphene (Gr)/CrX_3 (X = Cl, Br, I) heterojunctions [220, 193, 221, 222, 223, 1, 224, 225], a comprehensive overview of few-layer Gr/CrX_3 (X = F, Cl, Br, I) junctions is still missing. Namely, band alignments in N-layer (N = 1, 2, 3)

Gr/CrX_3 structures are yet to be fully explored. Although band alignments in multilayer metal-semiconductor heterojunctions are commonly approximated based on monolayer/monolayer junctions, this strategy overlooks thickness dependent effects due to quantum confinement.

4.2 Crystal Structures

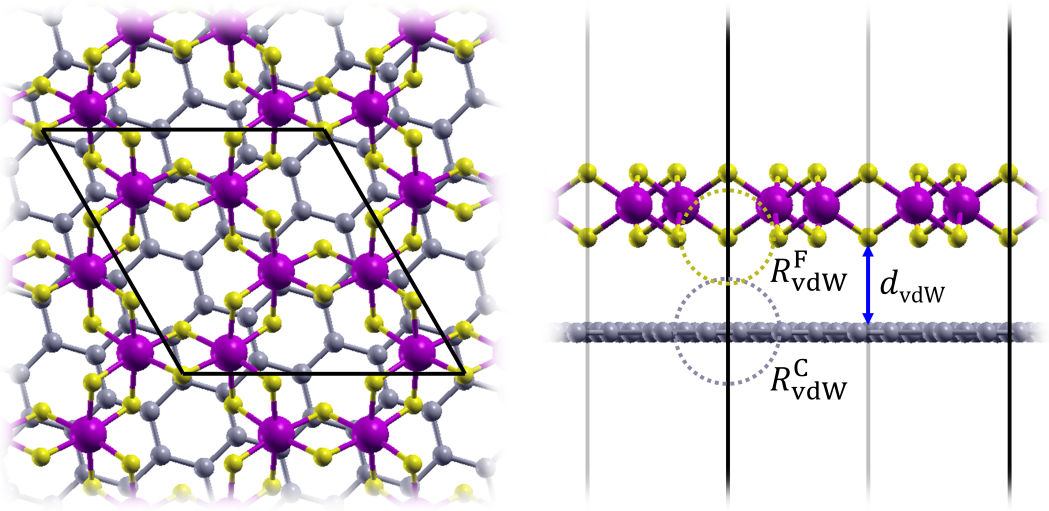

Figure 4.1: Top and side schematic of the $\sqrt{13} \times \sqrt{13}$-Gr/$\sqrt{3} \times \sqrt{3}$-$CrF_3$ supercell. Solid lines in the different cross-sections mark the unit cell of each layer.

The epitaxy for each Gr/CrX_3 heterostructure is selected based on minimizing the strain imposed by lattice mismatches between graphene and CrX_3. In order to ensure commensurate Gr/CrX_3 supercells and preserve CrX_3 band structures, low amounts of strain ($<2\%$) are permitted in the graphene layers (Table 4.1). For few-layer Gr/CrX_3 junctions, graphene layers are turbostratically stacked [186, 188, 187] to avoid band splitting and reduce thickness dependent dispersion seen in Bernal stacked graphene [180, 185]. Due to out-of-plane periodic boundary conditions, heterojunctions include at least 15 Å vacuum space. Moreover, equilibrium configurations are reached via atomic relaxation, while the in-plane CrX_3 lattice constant a is held fixed.

In addition to the computational details described in Chapter 2.5, the 2D-BZ in the two smallest heterojunction supercells are sampled using a 12×12 Monkhorst-Pack mesh [189] while the two largest cells are sampled using a 6×6 mesh (see Table 4.1), where BZ integration is performed using the tetrahedron method [226, 227]. The effective Hubbard terms in DFT+U

calculations are determined self-consistently by utilizing the ACBN0 pseudohybrid Hubbard density functional [154]. The convergence thresholds of total energy and forces for ionic minimization is set to their default values of 1.0×10^{-4} Ry and 1.0×10^{-3} Ry·a_0^{-1}, respectively. The convergence threshold for self-consistent calculations are set to 1.0×10^{-8} Ry. All electronic band structures are plotted using the PAOFLOW utility [228].

Table 4.1: CrX_3 (X = F, Cl, Br, I) PBE (experimental) lattice constants a, effective CrX_3 unit cells (UCs) in Gr/CrX_3 epitaxies, effective Gr unit cells in Gr/CrX_3 epitaxies, and vdW gaps d_{vdW} ($\approx R^{\text{C}}_{\text{vdW}} + R^{\text{X}}_{\text{vdW}}$) between graphene and CrX_3.

Gr/CrX_3	a (Å) [229, 71, 74, 13]	CrX_3 UCs	Gr UCs	d_{vdW} (Å) [230]
CrF_3	5.11 (4.99)	3	13	2.98 (2.93-3.17)
$CrCl_3$	5.91 (5.94)	7	39	3.27 (3.28-3.45)
$CrBr_3$	6.26 (6.30)	3	19	3.39 (3.40-3.55)
CrI_3	6.79 (6.87)	4	31	3.52 (3.57-3.68)

Below their respective critical temperatures T_c, CrX_3 layers adopt the R$\bar{3}$ hexagonal structure. In Table 4.1, we provide the calculated CrX_3 lattice parameters a, in good agreement with experimental bulk values [229, 71, 74, 13]. By introducing graphene to monolayer CrX_3, the two layers in the resulting 1L-Gr/CrX_3 junction appear flat with a vdW gap roughly equal to the sum of vdW radii for C and the respective halide X (Table 4.1), demonstrating largely vdW interlayer interactions as opposed to chemical bonding [193, 224].

4.3 Graphene/CrX_3 Junctions

We present the resulting electronic BS and projected density of states (PDOS) side-by-side of each 1L-Gr/CrX_3 junction in Fig. 4.2 using the PBE functional and in Fig. 4.3 using the pseudohybrid ACBN0 functional. Compared to their respective isolated CrX_3 monolayers, the majority spin CrX_3 conduction bands, which are composed of mainly Cr d-states and halide p-states [196], appear largely preserved in all 1L-Gr/CrX$_3$ structures. The CrX_3 DFT (PBE) band gaps are negligibly affected after the introduction of a graphene layer. Through the implementation of ACBN0 corrections, the presence of graphene on monolayer CrX_3 causes both the minority and majority CrX_3 band gaps to slightly shrink, apart from the majority gap of CrI_3 which largely remains unperturbed (Fig. 4.3). Similarly observed in Gr/MoS_2 junctions [231],

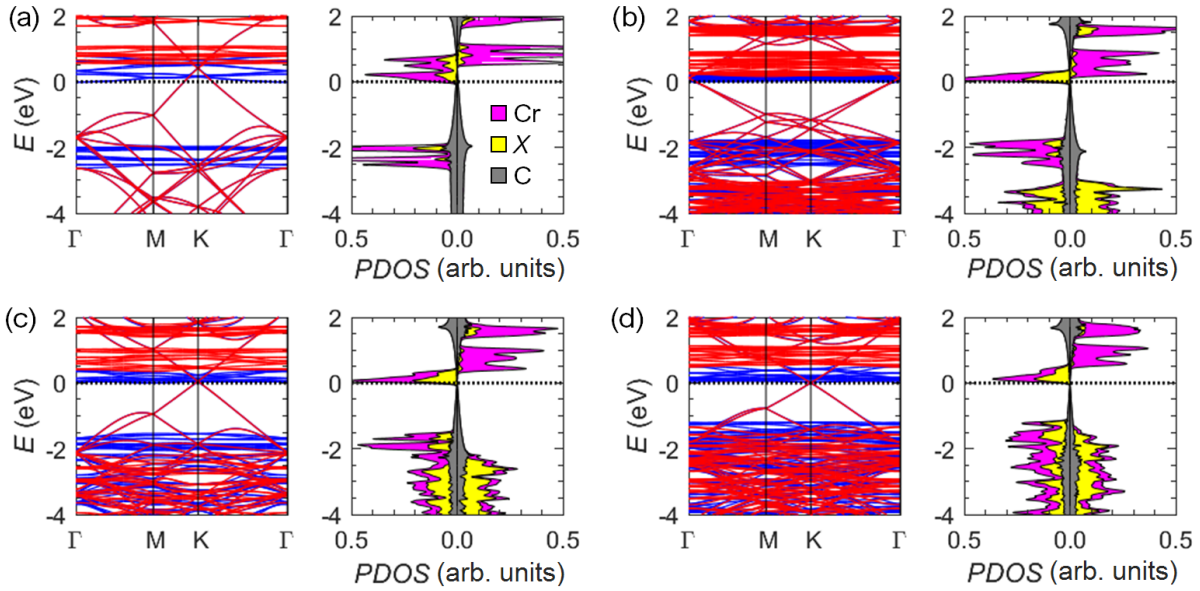

Figure 4.2: Electronic band structure and PDOS of (a) 1L-Gr/CrF_3, (b) 1L-Gr/$CrCl_3$, (c) 1L-Gr/$CrBr_3$, and (d) 1L-Gr/CrI_3 under the PBE approximation. Both the spin majority (blue; left) and minority (red; right) are plotted (bands; PDOS). Note that the PDOS of each system is normalized by the respective CrX_3 supercell area.

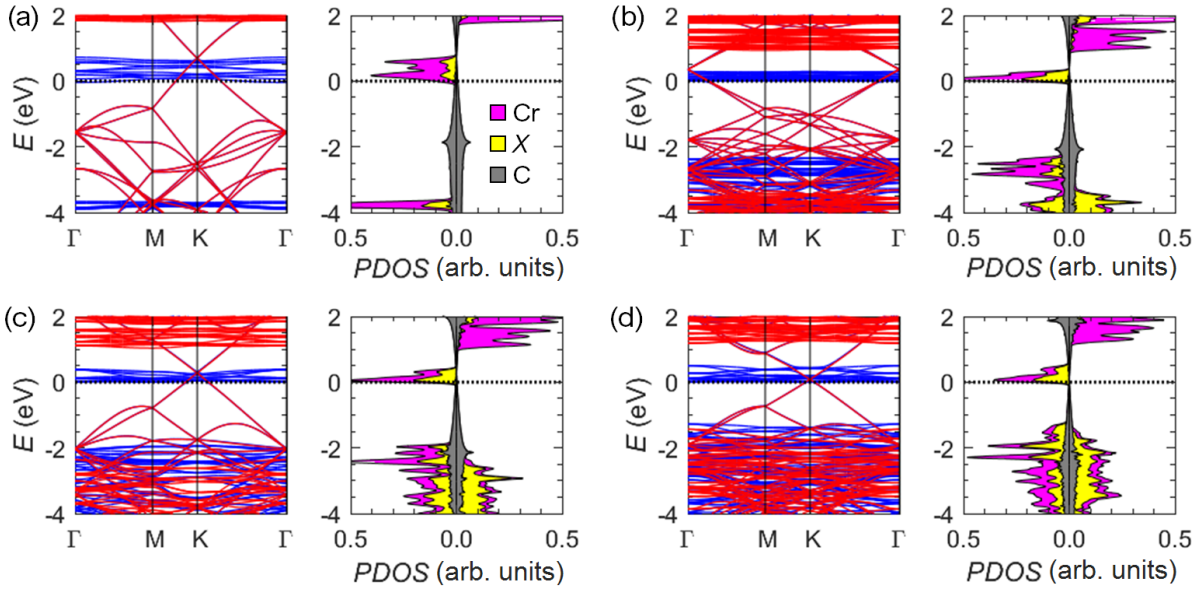

Figure 4.3: Electronic band structure and PDOS of (a) 1L-Gr/CrF_3, (b) 1L-Gr/$CrCl_3$, (c) 1L-Gr/$CrBr_3$, and (d) 1L-Gr/CrI_3 under the ACBN0 description. Both the spin majority (blue; left) and minority (red; right) are plotted (bands; PDOS). Note that the PDOS of each system is normalized by the respective CrX_3 supercell area.

semimetal graphene charge screening reduces the semiconductor bandgap through induced energy level shifts. Moreover, the majority conduction band edge (CBE) of all CrX_3 reside at the Fermi level while the DP of graphene in these 1L-Gr/CrX_3 junctions lie above the CBE due to

charge transfer. Band alignments attained via the ACBN0 method display significantly greater p-doping of the graphene states compared to PBE results, where ACBN0 alignments for CrI_3 are in good agreement with prior GGA+U and HSE calculations [193].

All 1L-Gr/CrX_3 junctions are found to exhibit partial charge transfer from graphene, in which charge accumulates not only at the CrX_3 layer but extends within the Gr/CrX_3 vdW gap as illustrated in previous studies of 1L-Gr/CrX_3 (X = Cl, Br, I) junctions [193, 221, 223, 224, 225]. Additionally, inhomogeneous layers of charge form at graphene surfaces, leading to the formation of interface dependent dipoles between the two charged sheets [222, 223]. Consequently, the formation of out-of-plane dipoles produce small upward shifts in the CrX_3 CBE and valence band edge (VBE) relative to vacuum [232, 233]. Through the use of a strong external electric field [223] or large out-of-plane compressive strain [193, 221], past theoretical studies have demonstrated band modification in 1L-Gr/CrX_3 (X = Br, I) junctions, where these Ohmic systems are switched to Schottky contacts. Although band manipulation using the aforementioned extensive electrical and mechanical techniques offers phenomenal responses and insight, these processes are not viable in conventional devices.

4.4 Multilayer-Graphene/CrX_3 Junctions

In order to quantify the effects due to lead thickness, bilayer (2L-Gr) and trilayer (3L-Gr) graphene contacts are analyzed in addition to a full 4L-Gr/2L-CrF_3/4L-Gr MTJ. Like the 1L-Gr/CrX_3 junctions, the majority CBE of CrX_3 reside near the Fermi energy within 2L-Gr/CrX_3 and 3L-Gr/CrX_3 (X = F, Cl, Br) heterostructures, except the majority CBE of CrI_3 which lies above the Fermi level (Fig. 4.5 and 4.6). Based on ACBN0 descriptions, both the minority and majority CrX_3 band gaps continue to moderately shrink as the number of graphene layers increase, excluding the majority gap of CrI_3 which remains consistent [Fig. 4.4(c)-(d)]. Similarly demonstrated in single-layer MoS_2 [234], the CrX_3 electronic states are fairly susceptible to the electrostatic environment as a result of quantum confinement [235]. In all multilayer Gr/CrX_3 systems, graphene layers display charge screening, where the DP of outermost graphene layers lie the lowest in energy (Fig. 4.5 and 4.6). Unlike the outer two graphene layers in 3L-Gr/CrX_3

junctions, the graphene layer adjacent to the halides appears to behave as a buffer layer, where the DP of the adjacent graphene layer resides at significantly higher energies (Fig. 4.5 and 4.6).

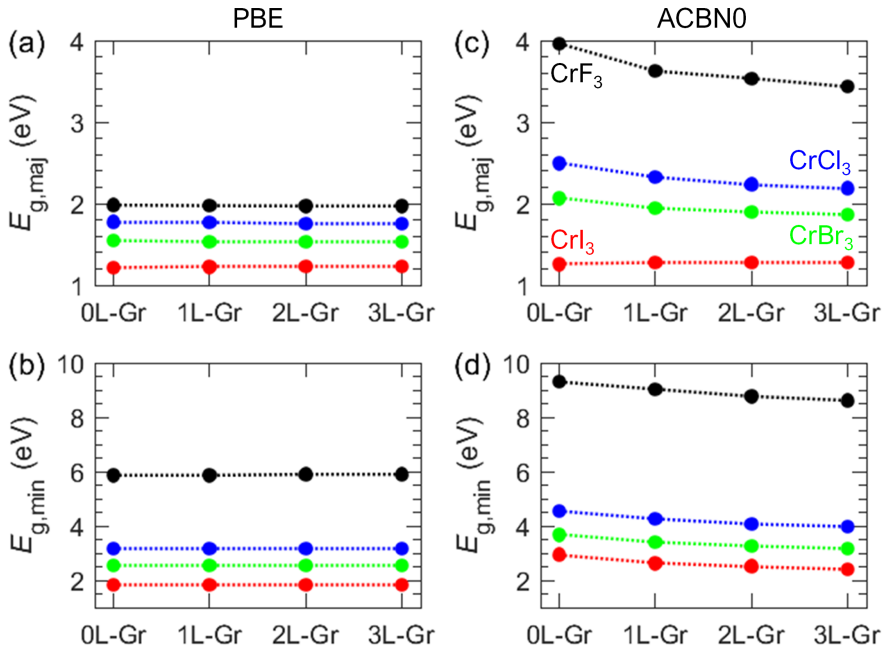

Figure 4.4: Electronic band gaps of (a) PBE majority states, (b) PBE minority states, (c) ACBN0 majority states, and (d) ACBN0 minority states.

For multilayer Gr/CrI_3 structures, the CrI_3 majority CBE no longer lies at the Fermi level as the graphene DP falls within the CrI_3 band gap as shown in Figs. 4.5(d) and 4.6(d). Unlike the lighter halide systems, CrI_3 holds an electron affinity (EA) comparable to the work function (WF) of graphene [193]. Through the addition of graphene layers, the Gr/CrI_3 junction readily switches from an Ohmic contact to a Schottky contact, which would account for electron tunneling observed in Gr/CrI_3 based MTJ experiments [236, 237, 203, 209]. Moreover, a Schottky contact in 1L-Gr/CrI_3 junctions may be reached by applying ($\sim$4%) tensile strain to the graphene layer as demonstrated in our previous study [1]. Similar to the Gr/CrI_3 systems, the alternative multilayer Gr/CrX_3 (X = F, Cl, Br) junctions begin to transition into Schottky contacts [Fig. 4.5(a)-(c) and Fig. 4.6(a)-(c)]. For the 4L-Gr/2L-CrF_3/4L-Gr MTJ (Fig. 4.7), a Schottky barrier is formed between semi-bulk graphene and the CrF_3 channel. Here we demonstrate that Gr/CrX_3 Schottky contacts can be achieved through graphene WF engineering as opposed to the employment of strong external forces.

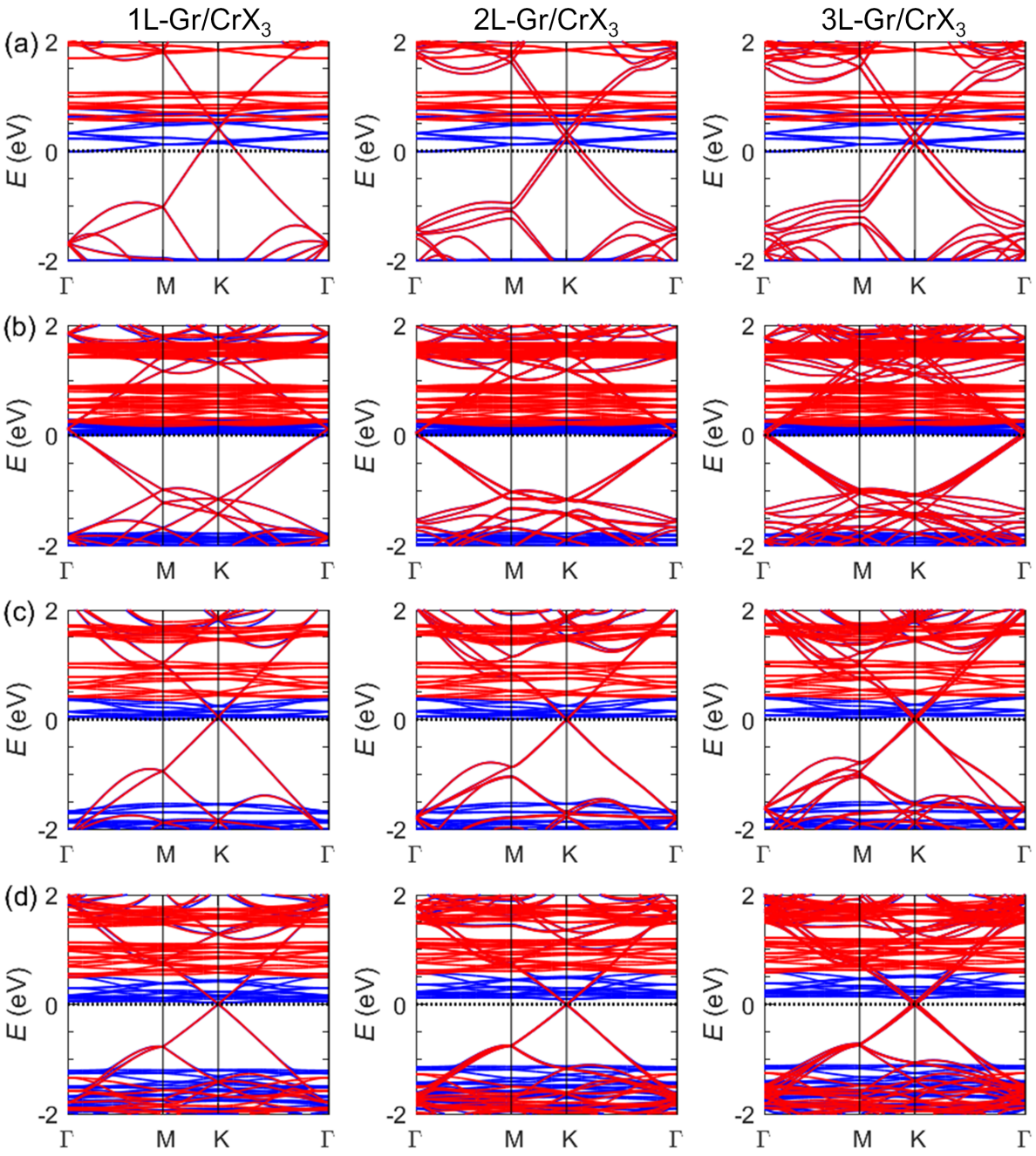

Figure 4.5: Electronic band structure of (a) NL-Gr/CrF_3, (b) NL-Gr/$CrCl_3$, (c) NL-Gr/$CrBr_3$, and (d) NL-Gr/CrI_3 under the PBE approximation for N = 1, 2, and 3 (left to right). Both spin majority (blue) and minority (red) are plotted.

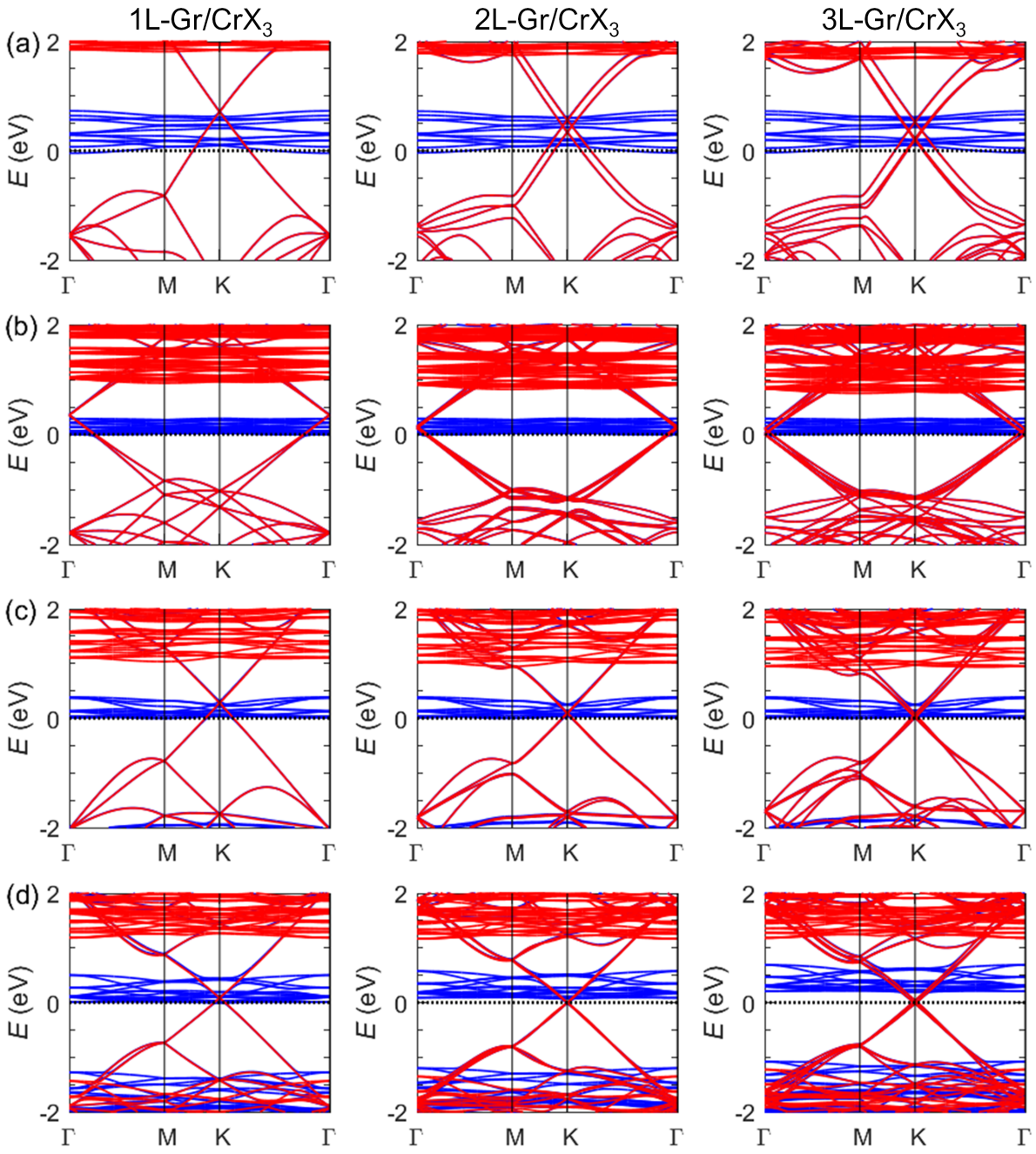

Figure 4.6: Electronic band structure of (a) NL-Gr/CrF_3, (b) NL-Gr/$CrCl_3$, (c) NL-Gr/$CrBr_3$, and (d) NL-Gr/CrI_3 under ACBN0 descriptions for N = 1, 2, and 3 (left to right). Both spin majority (blue) and minority (red) are plotted.

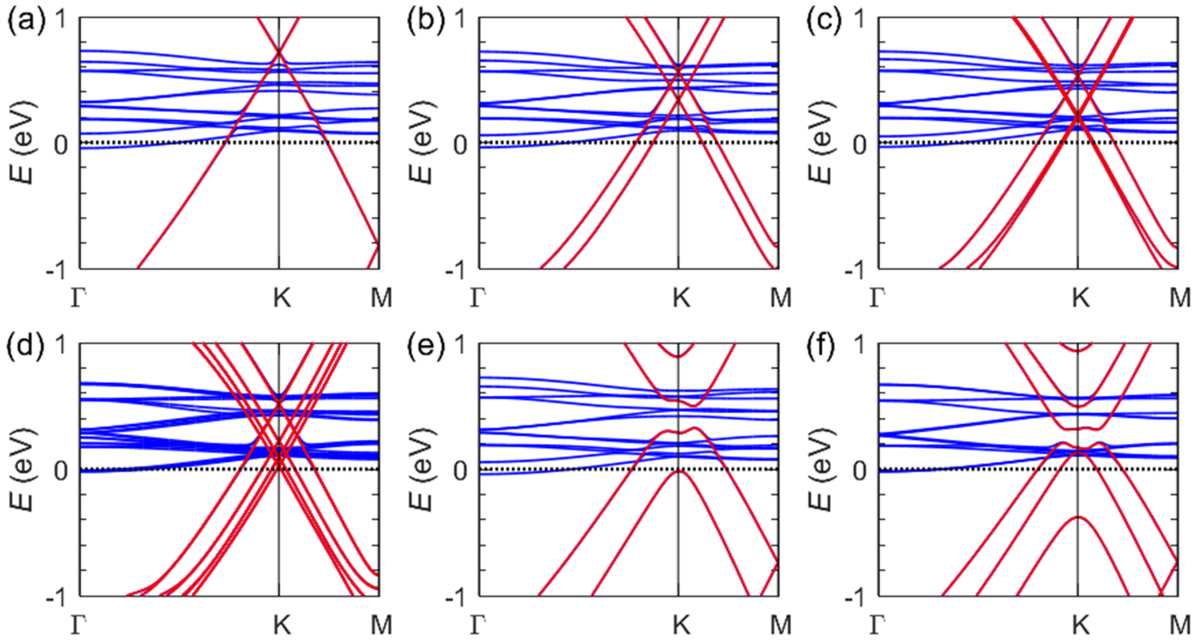

Figure 4.7: Electronic band structure of (a) 1L-Gr/CrF_3, (b) 2L-Gr/CrF_3, (c) 3L-Gr/CrF_3, (d) 4L-Gr/2L-CrF_3/4L-Gr, (e) AB-Gr/CrF_3, and (f) ABA-Gr/CrF_3 under ACBN0 descriptions. Both spin majority (blue) and minority (red) are plotted.

In terms of doping, lighter halide systems promote the greatest charge transfer from graphene due in part to their larger electron affinities, based on PBE and ACBN0 approximations found in Table 4.2. We observe graphene p-doping as high as $\sim 10^{13}$ e/cm^2 in Gr/CrF_3 heterojunctions [Fig. 4.6(a)]. Due to the sizable charge transfer in Gr/CrF_3 systems under the ACBN0 method, significant valence and conduction band splitting as large as 116 meV is observed in the 1L-Gr/CrF_3 junction as shown in Fig. 4.7(a). This electronic configuration is a product of Hubbard and crystal field splitting induced by conduction band occupation, where the degeneracy of Cr d_{zx} and d_{zy} states are broken above the CBE (Fig. 4.8) [238]. Moreover, band splitting in the 1L-Gr/CrF_3 structure is augmented via the Stark effect due to the presence of out-of-plane dipoles. As the number of graphene layers grow in multilayer Gr/CrF_3 junctions, CrF_3 band splitting is successively suppressed [Fig. 4.7(a)-(c)] due to diminishing charge transfer. For the alternative Gr/CrX_3 (X = Cl, Br, I) systems, negligible band splitting is observed.

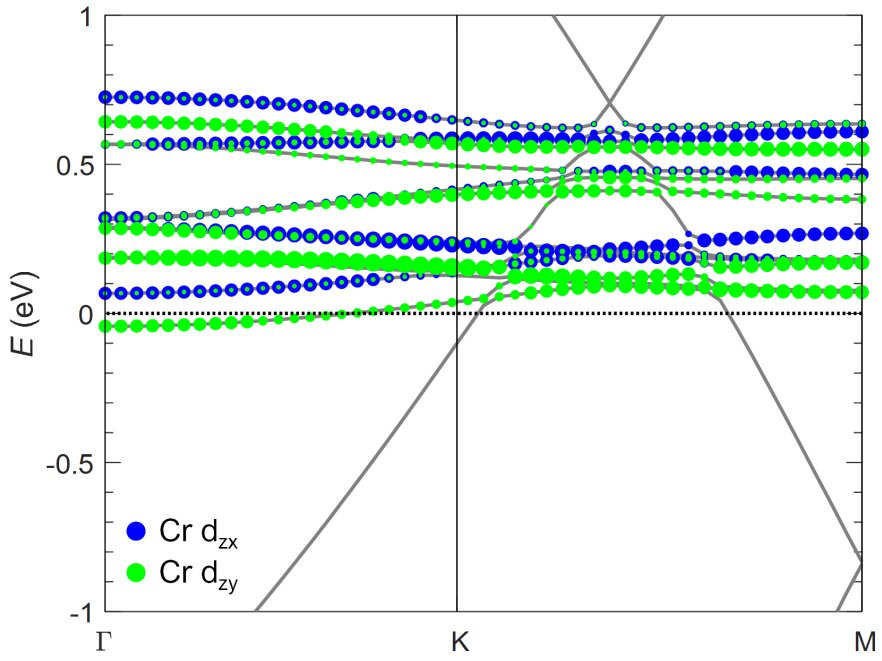

Figure 4.8: Electronic band structure of 1L-Gr/CrF_3 with superimposed Cr d_{zx} (blue) and d_{zy} (green) projections.

In addition to turbostratically stacked graphene contacts, we explore Bernal stacked (AB and ABA)-Gr/CrF_3 heterojunctions as seen in Fig. 4.7(e)-(f). Besides the thickness dependent dispersion of graphene, both AB-Gr/CrF_3 and ABA-Gr/CrF_3 junctions generate sizable band gaps of 173 meV and 104 meV in the few-layer graphene, respectively. Previous studies have demonstrated graphene band gap formation in Gr/CrI_3 junctions via strong external electric fields [223] or in-plane strain [225]; however, Bernal stacked Gr/CrF_3 heterojunctions require no external force to induce graphene band gaps. Instead, graphene band openings within AB-Gr/CrF_3 and ABA-Gr/CrF_3 junctions stem from large charge screening in the graphene layers due to substantial charge transfer to the CrF_3 layer.

Table 4.2: CrX_3 (X = F, Cl, Br, I) PBE (ACBN0) electron affinities E_{EA}, graphene PBE (ACBN0) WF in Gr/CrX_3 epitaxies, monolayer CrX_3 PBE (ACBN0) band gaps, and experimental bulk CrX_3 band gaps [12, 13]. Note that electron affinities are calculated based on energy differences between the CBE of CrX_3 and vacuum levels.

Gr/CrX_3	E_{EA} (eV)	Gr WF (eV)	E_g (eV)	Bulk Exp. E_g (eV)
CrF_3	6.93 (7.82)	4.33 (5.04)	1.98 (3.96)	-
$CrCl_3$	4.88 (6.42)	4.51 (5.20)	1.78 (2.49)	2.3
$CrBr_3$	4.72 (6.05)	4.45 (5.15)	1.54 (2.06)	2.1
CrI_3	4.55 (5.69)	4.28 (5.00)	1.21 (1.26)	1.2

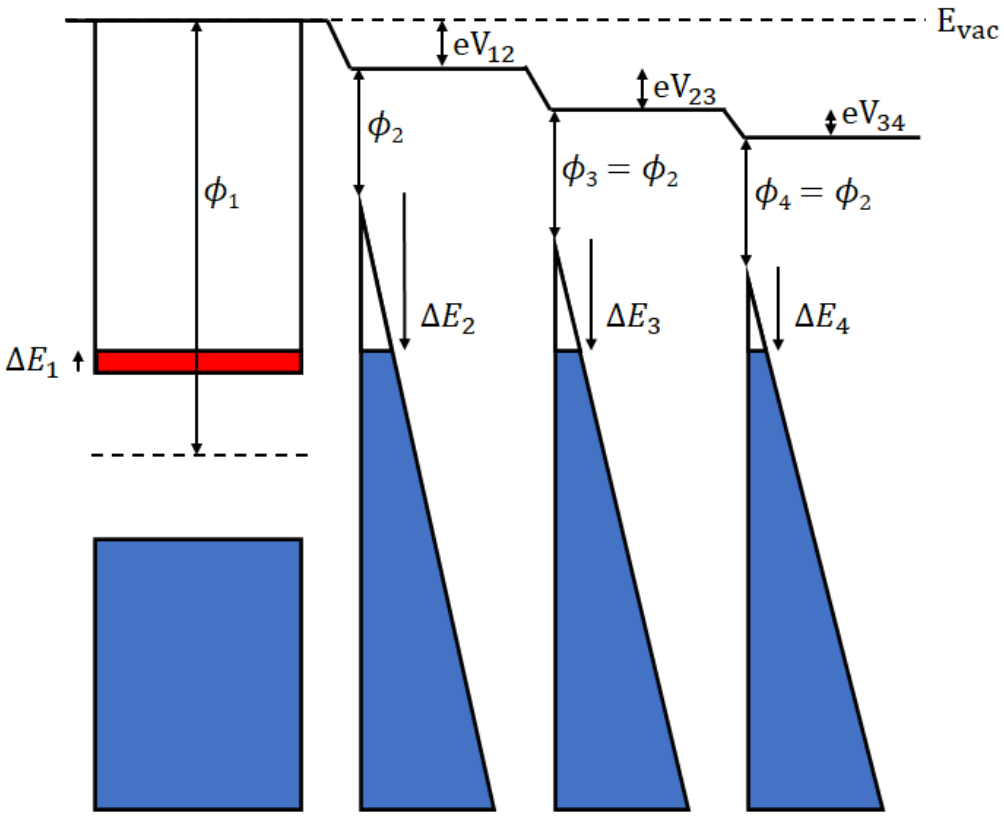

Figure 4.9: Electrostatic band alignment model between CrX_3 (leftmost) and three layers of graphene, where V_{12}, V_{23}, and V_{34} represent voltage drops from one layer to the next.

Foreknowledge of heterojunction band alignments are crucial in the development of novel devices. In order to approximate the band alignments in the Gr/CrX_3 heterojunctions we apply an electrostatic based model, which treats the graphene and CrX_3 layers similar to capacitors in series [239] as seen in Fig. 4.9. Using the chemical potential equalization principle, the band offsets ΔE of layer i and the successive layer $i+1$ may be described through the following:

$$(e\phi_i + \Delta E_i) - (e\phi_{i+1} + \Delta E_{i+1}) + \frac{e^2 L_{i,i+1}}{\kappa_{i,i+1}\epsilon_0} \sum_{j=1}^{i} \Delta N_j = 0 \tag{4.1}$$

where ϕ represents the work function of each layer while the last expression describes the voltage drop across layers, in which L represents the interlayer distance, κ represents the dielectric constant, and ΔN represents the charge on the layer. Note that Eq. 4.1 provides a system of

$N_L - 1$ equations where N_L defines the total number of layers in the junction. Furthermore, an additional equation may be defined based on the conservation of charge:

$$\sum_{j=1}^{N_L} \Delta N_j = 0 \tag{4.2}$$

where the total charge for all layers must equal zero. Lastly, the charge transfer from each sheet can be approximated at low temperatures:

$$\Delta N_j \sim \int_{E_F=0}^{\Delta E_j} g_j(E) dE \tag{4.3}$$

where $g(E)$ represents the density of states of an isolated layer. For small energy shifts ΔE, the DOS of graphene is characterized by its linear dispersion:

$$g_{\text{Gr}}(E) \approx \frac{2}{\pi \hbar^2 v_F^2} |E| \tag{4.4}$$

where $v_F \sim 10^6$ m/s denotes the Fermi velocity of graphene [240]. The charge transfer from the CrX_3 layer may be expressed as a polynomial expansion:

$$\Delta N_{\text{CrX}_3}(E) = \sum_{m=1}^{\infty} C_m E^m \tag{4.5}$$

where the coefficients C_m are fitting parameters of the integrated DOS (IDOS). We find that a simple linear fit ($N_{\text{CrX}_3}(E) \approx C_1 E$) as seen in Fig. 4.10(b) provides consistent results to higher degree approximations in the Gr/CrX_3 systems, where energy shifts occur mainly in graphene due to its disproportionately low DOS compared to the conduction band states of CrX_3. Moreover, we find that generalizing the definitions above to take into account temperature produces negligible changes in energy shifts for temperatures under the critical temperatures of CrX_3.

Band alignments in all Gr/CrX_3 heterojunctions are calculated by solving for the band offsets ΔE in Eq. 4.1 using work functions ϕ of isolated layers derived from PBE and ACBN0 methods (Table 4.2). For graphene, the work function is defined as the energy difference between the Fermi energy and the vacuum level, while the work function of monolayer CrX_3 is

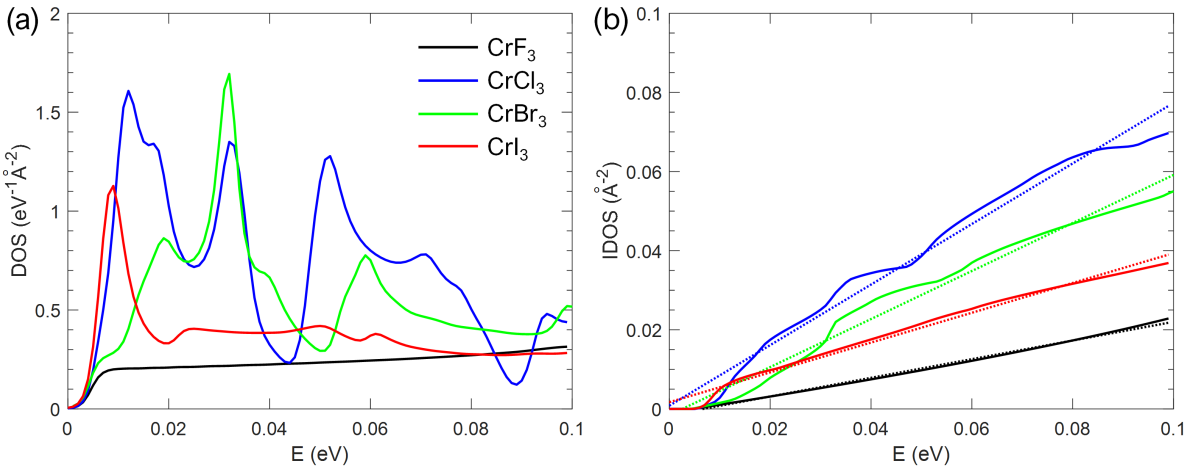

Figure 4.10: (a) Monolayer CrX_3 DOS close to the conduction band edge. (b) Integrated DOS (IDOS) of monolayer CrX_3 relative to the Fermi level.

defined as the energy difference between its midgap energy and the vacuum level. Note that the vacuum energy in each system is calculated based on the planar average of the electrostatic potential. The resulting band alignment predictions are plotted below PBE and ACBN0 results shown in Figs. 4.11 and 4.12, respectively. By treating layers in Gr/CrX_3 junctions as capacitors in series, the band alignment model helps capture overall charge screening trends in the graphene layers. For the Gr/CrF_3 heterojunctions, the band alignment model produces comparable results to that of PBE or ACBN0 methods. Model prediction begins to break down for systems with heavier halides due to substantial decreases in charge transfer. One of several assumptions made in the band alignment model is that charged layers within a junction behave as uniformly charged planes. This approximation fails in systems characterized predominantly by interface (spatially) dependent dipole interactions, key descriptions captured via *ab initio* calculations.

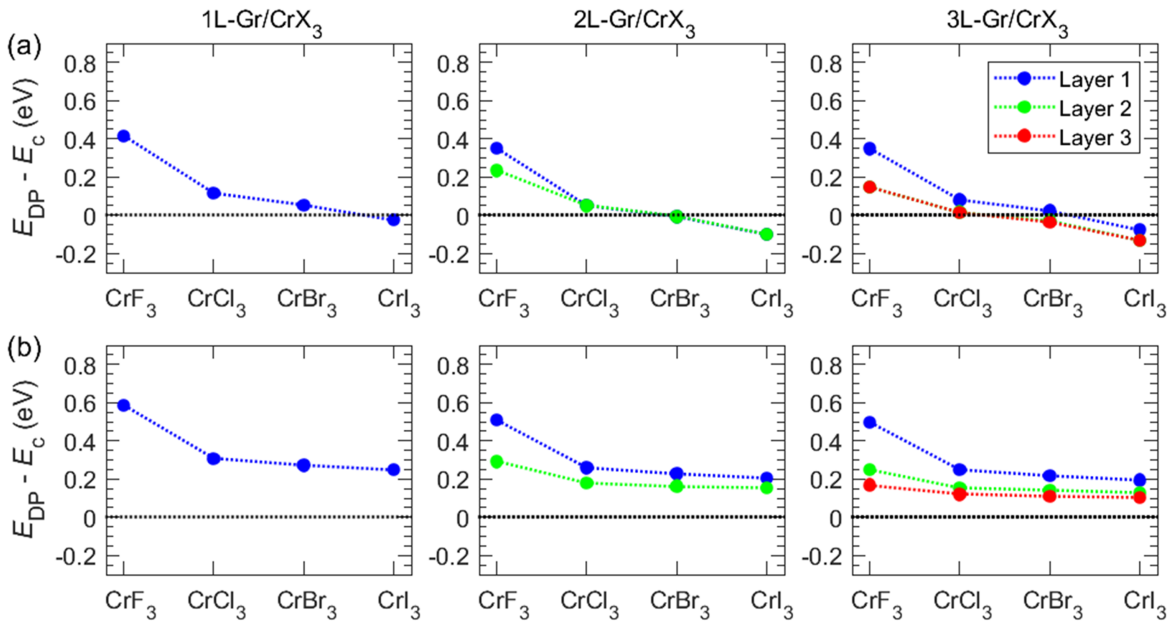

Figure 4.11: Band alignments between graphene Dirac point(s) and CrX_3 CBE determined via (c) PBE results or (d) electrostatic model for NL-Gr/CrX_3 junctions (N = 1, 2, 3).

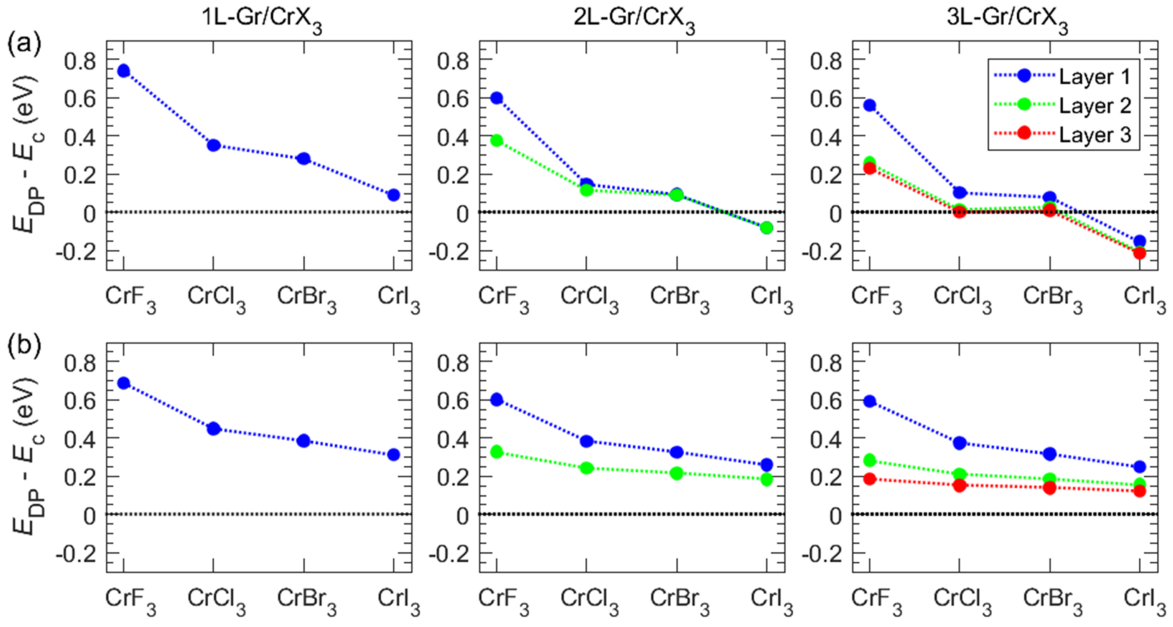

Figure 4.12: Band alignments between graphene Dirac point(s) and CrX_3 CBE determined via (c) ACBN0 results or (d) electrostatic model for NL-Gr/CrX_3 junctions (N = 1, 2, 3).

Chapter 5

Transition Metal Dichalcogenide/CrX_3 Heterojunctions

5.1 Summary and Background

Regarding the material contained in this chapter, we are the first to probe tunneling magnetoresistance (TMR) in MSe$_2$/CrX_3 (M = Nb and Ta; X = Cl and I) and 2H-TaS$_2$/CrI$_3$ based magnetic tunnel junctions (MTJs) using first principles calculations within the DFT and Landauer's formalism for ballistic transport. Close to the Fermi level, 2H-MSe$_2$/2L-CrI$_3$ (M = Nb and Ta) junctions produce roughly 10^3 times greater transmission than in graphene/2L-CrI$_3$ MTJs. Moreover, we produce average transmission estimates through ideal N-layer (N = 2, 3, and 4) CrX_3 (X = Br and I) junctions using the complex wavevectors from bulk. Based on complex band structure (CBS) transmission estimates, we discover two promising electrode candidates (1T-TaSe$_2$ and 2H-TaS$_2$) for CrI$_3$ based junctions, enabling TMR values on the order of 10^2% or greater in bilayer and tetralayer systems. Additionally, analysis of layer resolved projected density of states (PDOS) of 2H-MSe$_2$/CrX_3 (M = Nb and Ta; X = Cl and I) junctions reveals the formation of metal-induced gap states (MIGS) in CrX_3 caused by interlayer coupling, which significantly alters transmissions through these devices at energies above the Fermi level. This work was presented as an oral presentation at the 2021 APS March Meeting.

Recent MTJ experiments based on graphene/N-layer CrX_3 (N = 2, 6, 8, 10, and 12; X = Cl, Br, and I) heterostructures have demonstrated TMR values ranging between 50-200% for bilayer junctions and upwards of 10^6% in multilayer CrI$_3$ channels below 2 K. Although colossal TMR is achievable in these devices, graphene leads in concert with the CrX_3 channel yield low current densities of $\sim$0.1 mA·cm^{-2} at near-zero bias and $\sim$100 mA·cm^{-2} at high

bias [108]. In a recent theoretical study, the use of Cu leads has been proposed [182], which estimates nearly 100% spin majority transmission in Copper/bilayer-Cr_3 junctions with TMR values on the order of 10^3%. Due to their vast properties and atomic thicknesses, transition metal dichalcogenides (TMDs) such as magnetic 1T-VX_2 (X = Se and Te) and 2H-MoS_2 have also been proposed by theoretical studies as lead or channel materials in 2D based MTJs capable of TMR on the order of 10^2% [241, 242, 243]. Apart from controlling the magnetic order of 1T-VSe_2 in theoretical 1T-VSe_2/CrI_3 junctions, exfoliation of 1T-VSe_2 flakes remains a challenge since 1T-VSe_2 is highly unstable in air [244]. Current experimental work on the incorporation of TMD layers is limited to their use as channel materials, producing low TMR values on the order of 0.1% to 10% [245, 246, 247, 248, 249].

5.2 Crystal Structures

The systems considered here are formed by CrX_3 (X = Cl and I) channels and few-layer TMD electrodes, where the thickest tunnel junctions consist of four CrI_3 layers arranged by ABC stacking. The epitaxy of these cells accommodates (1×1)-CrI_3 layers on (2×2)-MSe$_2$ (M = Nb and Ta) or (1×1)-$CrCl_3$ on $(\sqrt{3} \times \sqrt{3})$-$MSe_2$ (M = Nb and Ta), where the in-plane lattice constant is set to that of the CrX_3 (see Table 4.1), yielding roughly 1% (3%) or less lateral strain applied to the few-layer MSe$_2$ (2H-TaS_2) electrodes. Three TMD layers on each side of the junction serve as the leads for the heterostructure, as illustrated in Fig. 5.1. Additionally, periodic boundary conditions are assumed in all three dimensions. The equilibrium configurations for all TMD/CrX_3 heterojunctions are obtained by holding the in-plane lattice constant a fixed while allowing the out-of-plane lattice parameter c of the entire supercell and all atoms to fully relax.

In addition to the computational details described in Chapter 2.5, the 2D-BZ is sampled using a 12×12 Monkhorst-Pack mesh [190], where BZ integration is performed using Methfessel-Paxton first-order spreading [190]. Similar to Chapter 3, quantum transport calculations are performed using the transportPAO code[191, 192], where two (one) TMD layers in the 2H (1T) phase serve as the bulk leads. The convergence thresholds of total energy and forces for ionic

minimization is set to their default values of 1.0×10^{-4} Ry and 1.0×10^{-3} Ry·a_0^{-1}, respectively. The convergence threshold for self-consistent calculations are set to 1.0×10^{-8} Ry.

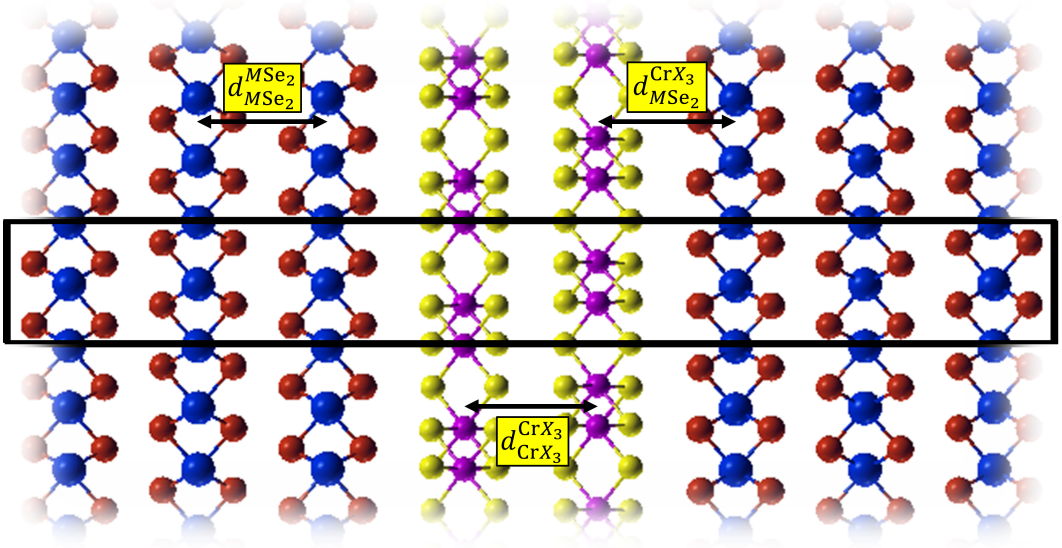

Figure 5.1: Schematic of a (2×2)-MSe$_2$/(1×1)-CrI$_3$ magnetic tunnel junction, where solid lines mark the supercell of the structure.

We calculate the average interlayer distances between adjacent CrX_3 (TMD) layers within TMD/2L-CrX_3 heterojunctions. Note that interlayer distances are computed as the difference between average in-plane heights of Cr (or M = Nb and Ta) atoms with the average in-plane heights of metal atoms in the adjacent layer. As seen in Table 5.1 for bilayer MTJs, the resulting interlayer distances $d^{CrI_3}_{CrI_3}$ between adjacent bilayer CrI$_3$ layers between MSe$_2$ or 1T-TaS$_2$ leads are nearly identical to those found in Gr/2L-CrI$_3$ junctions. The interlayer distances $d^{CrCl_3}_{CrCl_3}$ between adjacent bilayer CrCl$_3$ layers within 2H-MSe$_2$ (M = Nb and Ta) leads are close to 0.8 Å smaller than distances between CrI$_3$ layers due to the smaller vdW radius of chlorine [230]. Furthermore, the average interlayer distances d^{TMD}_{TMD} between adjacent MSe$_2$ (M = Nb and Ta) or 1T-TaS$_2$ layers are comparable to experimental bulk values [14, 15, 16, 17]. Lastly, average interlayer distances $d^{TMD}_{CrI_3}$ between CrI$_3$ and 2H-NbSe$_2$ are roughly 0.1 Å smaller than distances between CrI$_3$ and TaSe$_2$ layers.

Table 5.1: Number of CrX_3 unit cells (UCs) in TMD/CrX_3 epitaxies, number of TMD unit cells in TMD/CrX_3 epitaxies, interlayer distances between adjacent CrX_3 layers $d^{\mathrm{Cr}X_3}_{\mathrm{Cr}X_3}$, average interlayer distances via PBE+vdW results (experimental bulk value [14, 15, 16, 17]) between adjacent TMD layers $d^{\mathrm{TMD}}_{\mathrm{TMD}}$, and average interlayer distances between CrX_3 and TMD layers $d^{\mathrm{Cr}X_3}_{\mathrm{TMD}}$. All interlayer distances are calculated based on bilayer CrX_3 junctions.

CrX_3	TMD	CrX_3 UCs	TMD UCs	$d^{\mathrm{Cr}X_3}_{\mathrm{Cr}X_3}$ (Å)	$d^{\mathrm{TMD}}_{\mathrm{TMD}}$ (Å)	$d^{\mathrm{Cr}X_3}_{\mathrm{TMD}}$ (Å)
CrI_3	2H-$NbSe_2$	1	4	6.35	6.15 (6.27)	6.55
CrI_3	2H-$TaSe_2$	1	4	6.47	6.21 (6.35)	6.67
CrI_3	1T-$TaSe_2$	1	4	6.39	6.19 (6.27)	6.66
CrI_3	2H-TaS_2	1	4	6.43	5.85 (6.05)	6.44
$CrCl_3$	2H-$NbSe_2$	1	3	5.67	6.16 (6.27)	6.35
$CrCl_3$	2H-$TaSe_2$	1	3	5.60	6.24 (6.35)	6.32

5.3 2H-MSe$_2$/2L-CrX_3 Electronic Structures

First, the electronic band structures of (2×2)-bulk 2H-$NbSe_2$ and 2H-$TaSe_2$ which serve as MTJ electrodes, are analyzed as shown in Fig. 5.2 (left). We find that 2H-$NbSe_2$ and 2H-$TaSe_2$ are both metallic and do not display spin polarization (i.e., spin majority and minority states overlap one another), as similarly found in prior studies [250, 251, 252, 253, 254]. Furthermore, bulk 2H-$NbSe_2$ and 2H-$TaSe_2$ produce similar band structures in which flat bands just above the Fermi energy are visible at the Γ-point. These flat (heavy) bands correspond to small spikes in the DOS at those energy levels as seen in Fig. 5.2 (right). In addition, bulk 2H-$NbSe_2$ and 2H-$TaSe_2$ offer comparable DOS close to the Fermi level, drastically larger than the vanishing states (red) of graphene based leads. As a result, significantly higher current is expected to be produced in TMD/CrX_3 heterojunctions compared to Gr/CrX_3 based devices.

In Fig. 5.3 (left), we present the 2D electronic band structures of the 2H-$NbSe_2$/2L-CrI_3 MTJ in the (a) $\uparrow\uparrow$ and (b) $\uparrow\downarrow$ metamagnetic configurations for both spin majority (blue) and minority (red) states. For both junction configurations, the Fermi level resides within the CrI_3 band gap (tunneling regime). Moreover, the CrI_3 conduction bands are visible in each case above 0.7 eV. As similarly observed in the Gr/2L-CrI_3 junction, the conduction band edge (CBE) of CrI_3 in the antiparallel heterojuntion [Fig. 5.3(b)] lies roughly 0.1 eV higher in energy than in the parallel configuration. Furthermore, the 2D band structures of the 2H-$NbSe_2$/2L-CrI_3 MTJ in the (a) $\uparrow\uparrow$ and (b) $\uparrow\downarrow$ metamagnetic configurations are plotted in Fig. 5.4 (left). Like the 2H-$NbSe_2$/2L-CrI_3 MTJ, the resulting Fermi level falls within the CrI_3 band gap for

2H-$NbSe_2$/2L-CrI_3 heterojunctions, where the CBE of CrI_3 in the antiparallel configuration lies $\sim$0.1 eV higher in energy compared to the parallel configuration.

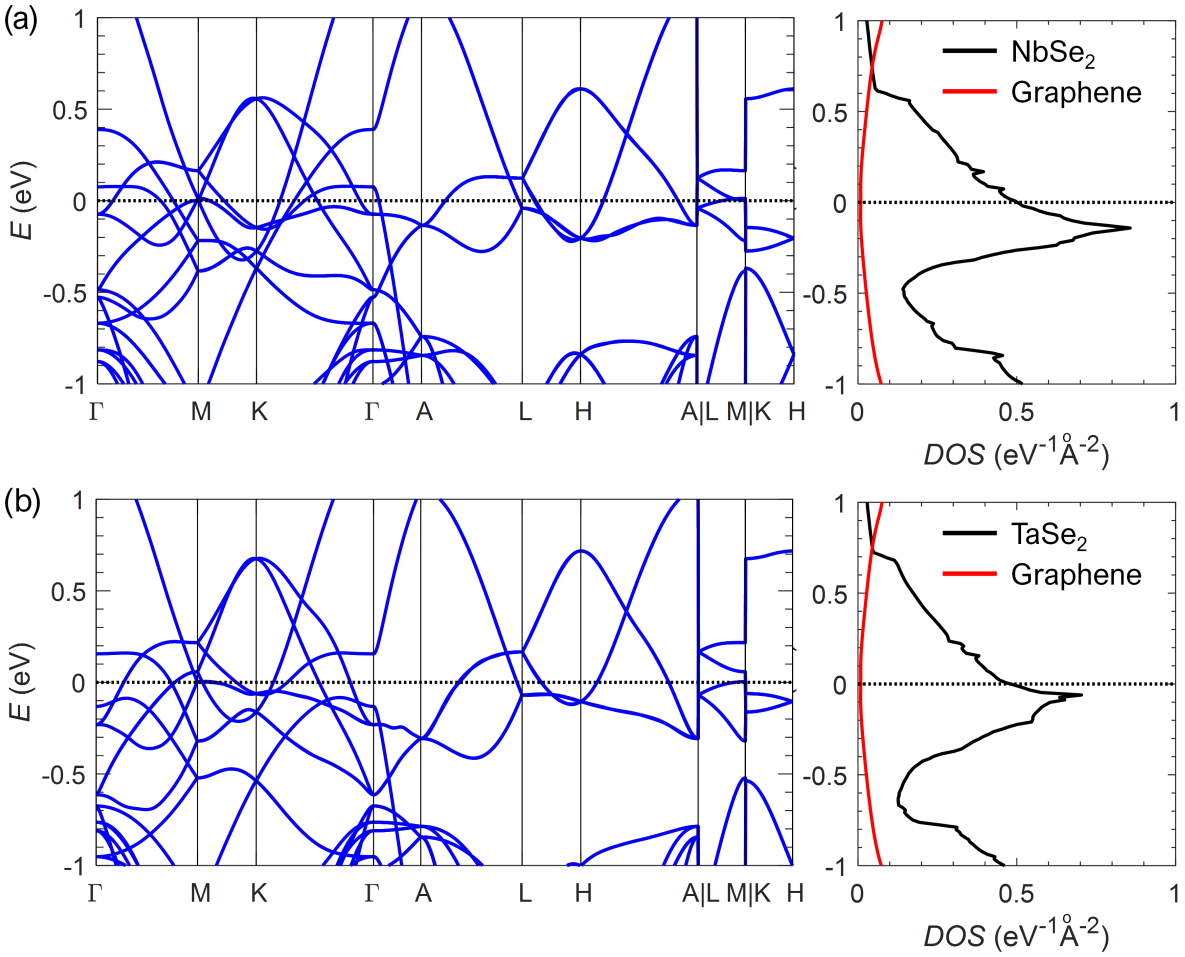

Figure 5.2: (a) Electronic band structure of (2×2)-bulk 2H-$NbSe_2$ (left) for spin majority (blue) and the total density of states (right). (b) Electronic band structure of (2×2)-bulk 2H-$TaSe_2$ (left) for spin majority (blue) and the total density of states (right). The density of states (DOS) of turbostratic graphene (red) is plotted alongside each TMD (black), where the DOS is normalized based on the area of each unit cell containing two layers.

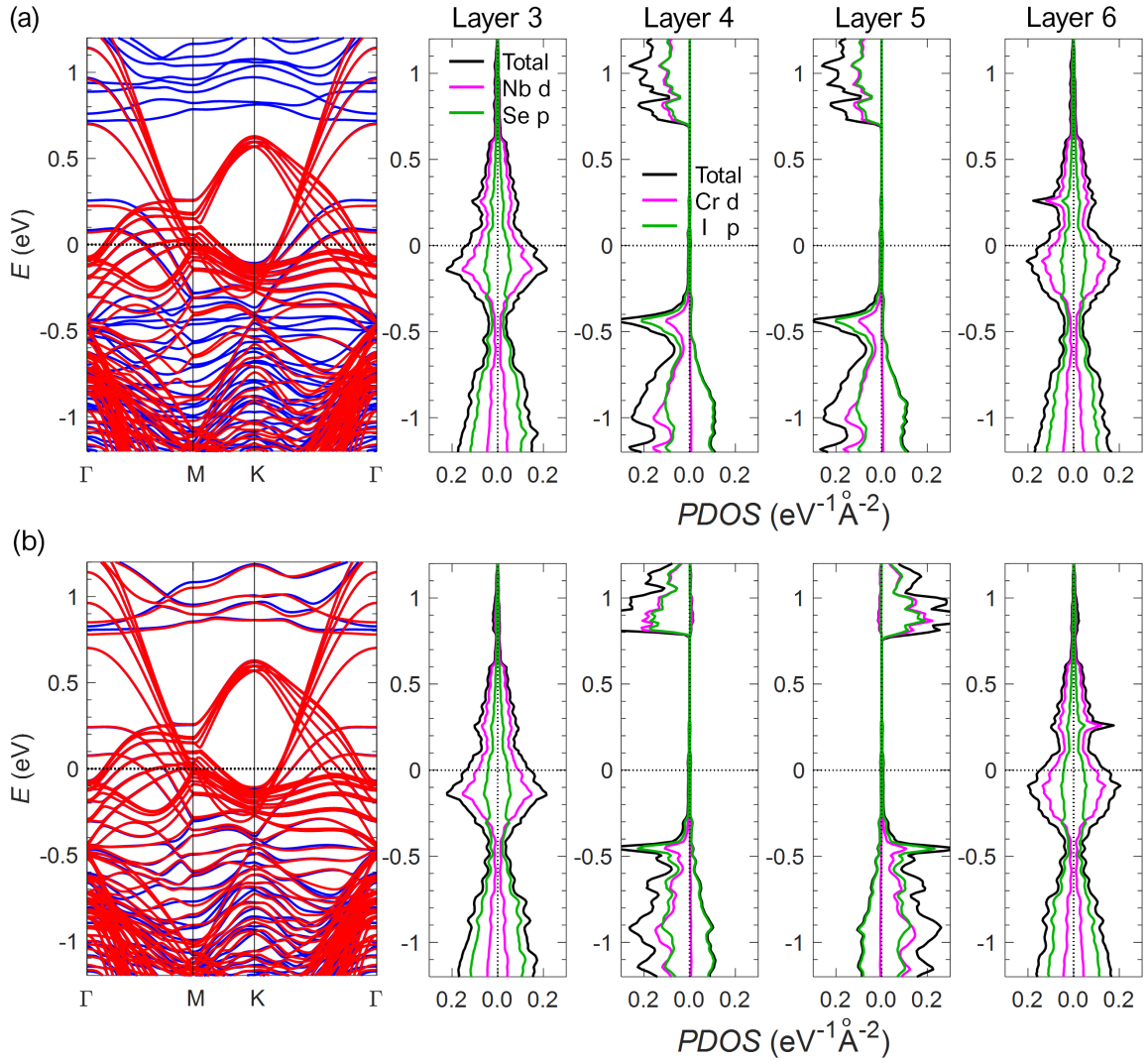

Figure 5.3: Electronic band structures (left) and layer resolved PDOS (right) of the 2H-$NbSe_2$/CrI_3 MTJ in the (a) parallel ↑↑ and (b) antiparallel ↑↓ configurations. Both spin majority (blue; left) and minority (red; right) states are plotted in band structures and the PDOS. Note that the PDOS are normalized based on the area of the junction.

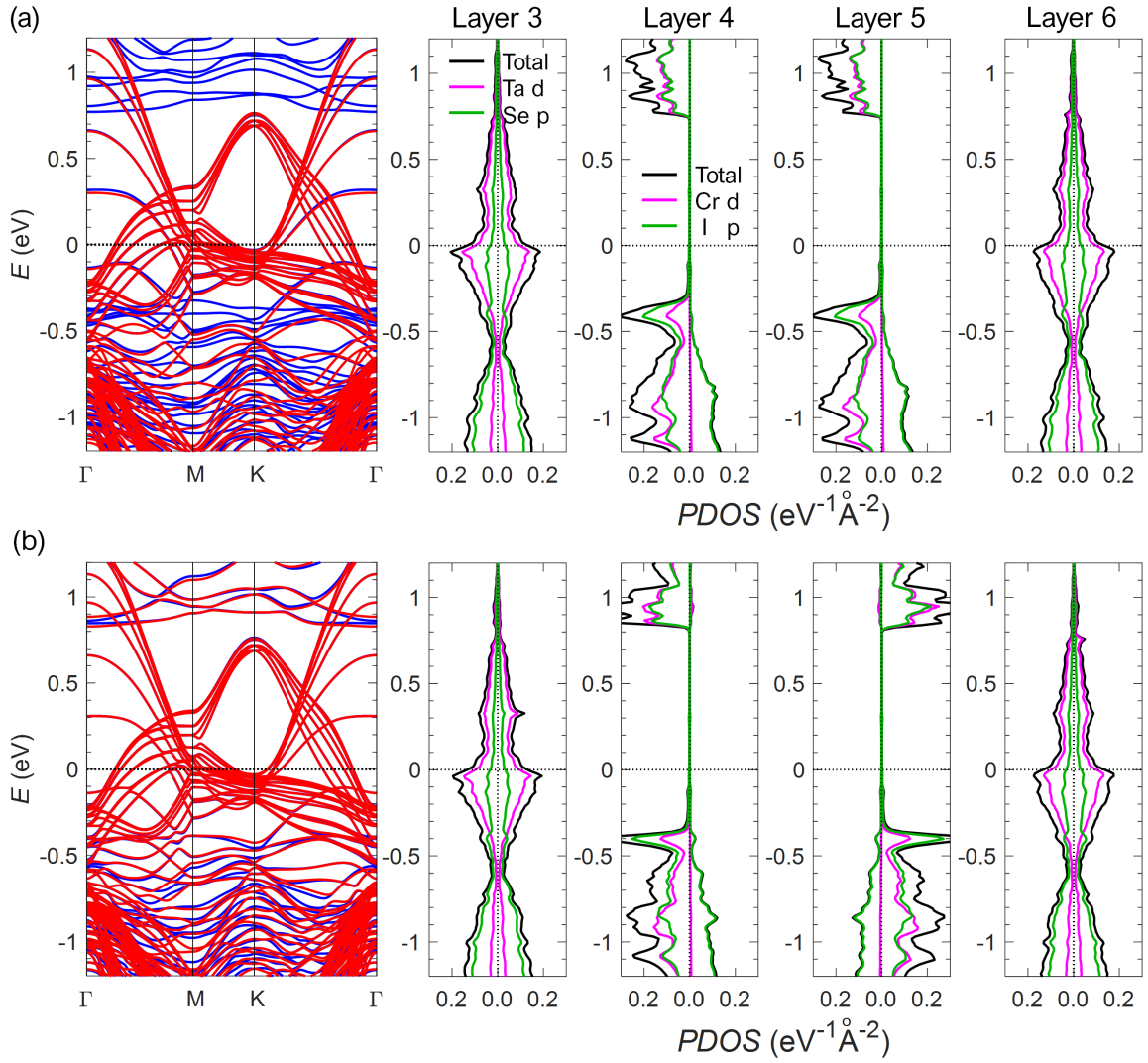

Figure 5.4: Electronic band structures (left) and layer resolved PDOS (right) of the 2H-$TaSe_2/CrI_3$ MTJ in the (a) parallel ↑↑ and (b) antiparallel ↑↓ configurations. Both spin majority (blue; left) and minority (red; right) states are plotted in band structures and the PDOS. Note that the PDOS are normalized based on the area of the junction.

To visualize the resulting band alignments produced in MSe$_2$/2L-CrI$_3$ (M = Nb and Ta) magnetic tunnel junctions, layer resolved PDOS are computed using the PAOFLOW utility [228], presented on the right-hand side of Fig. 5.3 and Fig. 5.4. As described in Chapter 3.3, this is achieved by summing projections onto pseudo-atomic orbitals for elements residing in layers 3, 4, 5, and 6 at MSe$_2$/2L-CrI$_3$ interfaces, where the sum of all projections (black), the sum of metal d-states (magenta), and the sum of chalcogen or halogen p-states (green) are plotted for each layer. In 2H-MSe$_2$/2L-CrI$_3$ heterojunctions, the Fermi energies reside $\sim$0.3 eV above the valence band edge (VBE) of CrI$_3$ for systems in either the $\uparrow\uparrow$ or $\uparrow\downarrow$ metamagnetic state (Fig. 5.3 and Fig. 5.4). As similarly observed in Gr/2L-CrI$_3$ based MTJs, CrI$_3$ band gaps within the parallel ($\uparrow\uparrow$) configuration are roughly 0.1 eV smaller than in the antiparallel ($\uparrow\downarrow$) configuration for 2H-MSe$_2$/2L-CrI$_3$ MTJs due to stronger magnetic coupling.

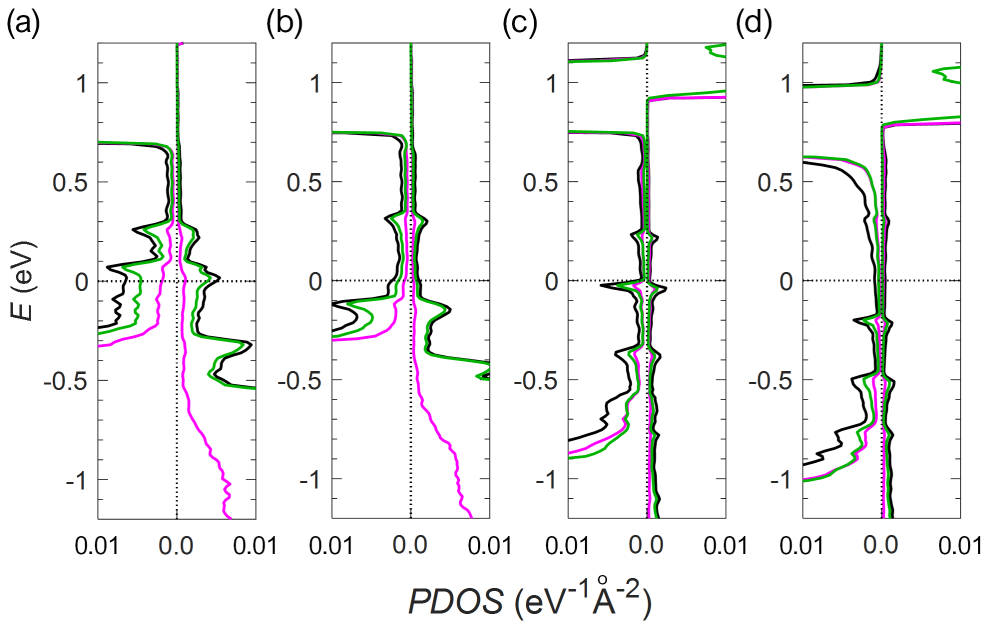

Figure 5.5: A zoomed in view of MIGS present in CrX_3 (Layer 5) induced at (a) 2H-NbSe$_2$/CrI$_3$, (b) 2H-TaSe$_2$/CrI$_3$, (c) 2H-NbSe$_2$/CrCl$_3$, and (d) 2H-TaSe$_2$/CrCl$_3$ interfaces for parallel MTJ configurations. Note that the PDOS are normalized based on the area of the junction.

As demonstrated in the layer resolved PDOS of the 2H-NbSe$_2$/2L-CrI$_3$ heterojunction (Fig. 5.3), weak interlayer coupling exist between the 2H-NbSe$_2$ and CrI$_3$ layers close to the

2H-$NbSe_2$/CrI_3 interfaces. The overlapping of states between the metal and the adjacent semiconductor results in the formation of metal-induced gap states (MIGS) at the 2H-$NbSe_2$/2L-CrI_3 interface [255], a feature also observed in metal/2H-MoS_2 interfaces with vdW separations [256, 257]. Gap states in 2H-$NbSe_2$/2L-CrI_3 junctions visibly extend from the bottom of the VBE of CrI_3 and beyond the Fermi level as seen in Fig. 5.5(a). These low density MIGS are comprised of mainly I p-states followed by Cr d-states. Moreover, enhancements in the DOS of $NbSe_2$ layers are visible between 0.2-0.3 eV due to heavy bands that pass through the Γ-point (Fig. 5.3). Additionally, spatial asymmetry between the left and right 2H-$NbSe_2$/CrI_3 interfaces, due to stacking orders, produces differing interfacial interactions on each side of the CrI_3 channel. Like 2H-$NbSe_2$/CrI_3 junctions, the formation of low density MIGS at 2H-$TaSe_2$/CrI_3 interfaces exist but to a lesser extent. Gap states in 2H-$TaSe_2$/2L-CrI_3 junctions visibly extend roughly 0.3 eV above the VBE of CrI_3 before tapering [Fig. 5.5(b)]. Similar to 2H-$NbSe_2$/2L-CrI_3 junctions, enhancements in the DOS of $TaSe_2$ layers are visible between 0.3-0.4 eV due to heavy bands that pass through the Γ-point (Fig. 5.4).

Additionally, we present in Fig. 5.6 and Fig. 5.7 the 2D electronic band structures and layer resolved PDOS of 2H-$M$$Se_2$/2L-$CrCl_3$ MTJs (M = Nb and Ta) in the (a) $\uparrow\uparrow$ and (b) $\uparrow\downarrow$ metamagnetic configurations for both spin majority (blue; left) and minority (red; right) states. Note that ($\sqrt{3} \times \sqrt{3}$)-$M$$Se_2$ (M = Nb and Ta) leads are used in 2H-$M$$Se_2$/2L-$CrCl_3$ junctions to mitigate the effects of strain. We find that the Fermi energies in 2H-$NbSe_2$/2L-$CrCl_3$ heterojunctions reside nearly 1.0 eV above the VBE of $CrCl_3$ (Fig. 5.6) while the Fermi energies in 2H-$TaSe_2$/2L-$CrCl_3$ junctions reside closer to 1.1 eV above the VBE (Fig. 5.7). The $CrCl_3$ conduction bands are visible 0.7 eV above the Fermi level in all cases. Similar to the bilayer CrI_3 based junctions, 2H-$NbSe_2$ and $TaSe_2$ leads display coupling with the $CrCl_3$ channels, albeit fairly weaker [Fig. 5.5(c)-(d)].

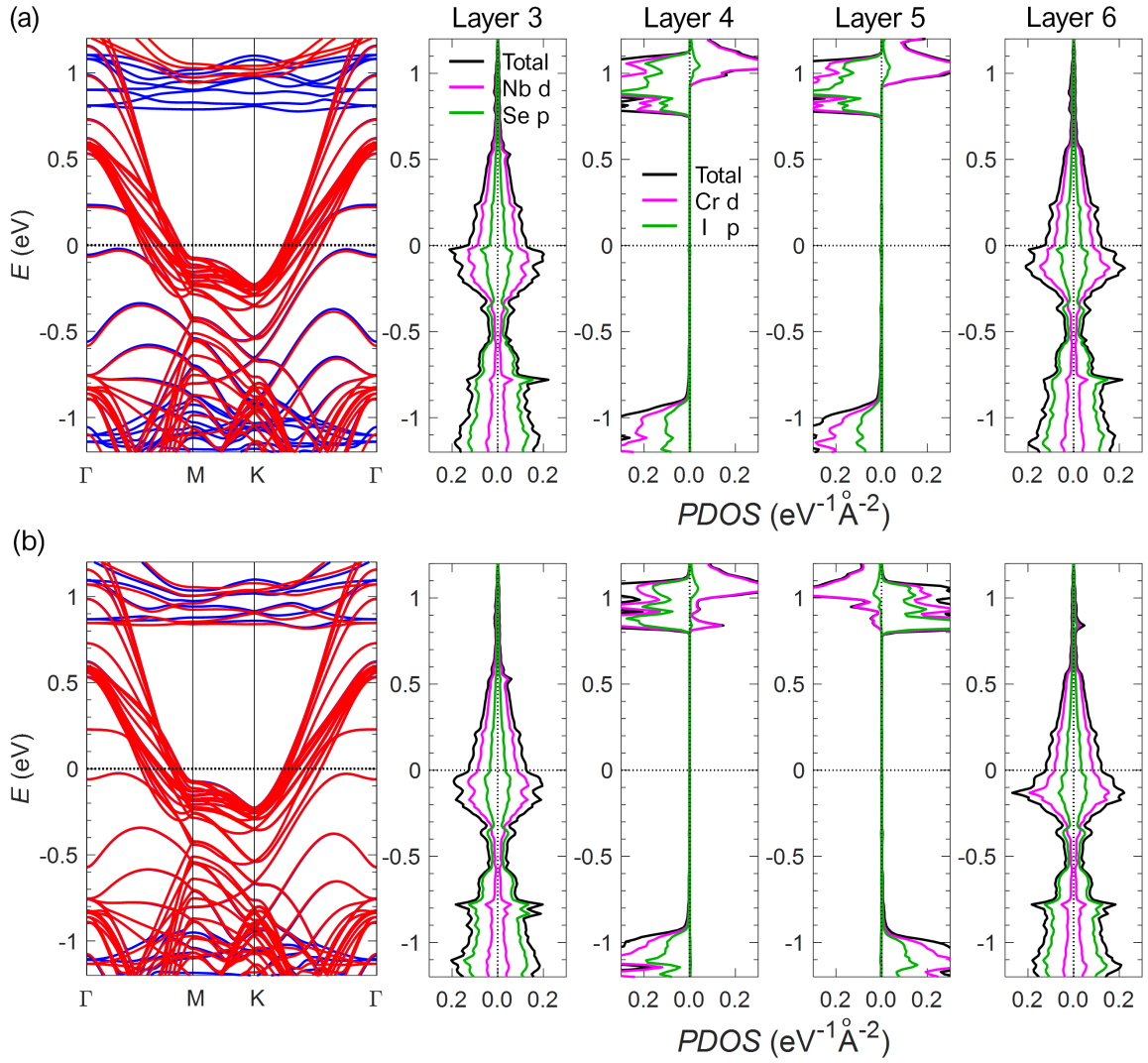

Figure 5.6: Electronic band structures (left) and layer resolved PDOS (right) of the 2H-$NbSe_2$/$CrCl_3$ MTJ in the (a) parallel ↑↑ and (b) antiparallel ↑↓ configurations. Both spin majority (blue; left) and minority (red; right) states are plotted in band structures and the PDOS. Note that the PDOS are normalized based on the area of the junction.

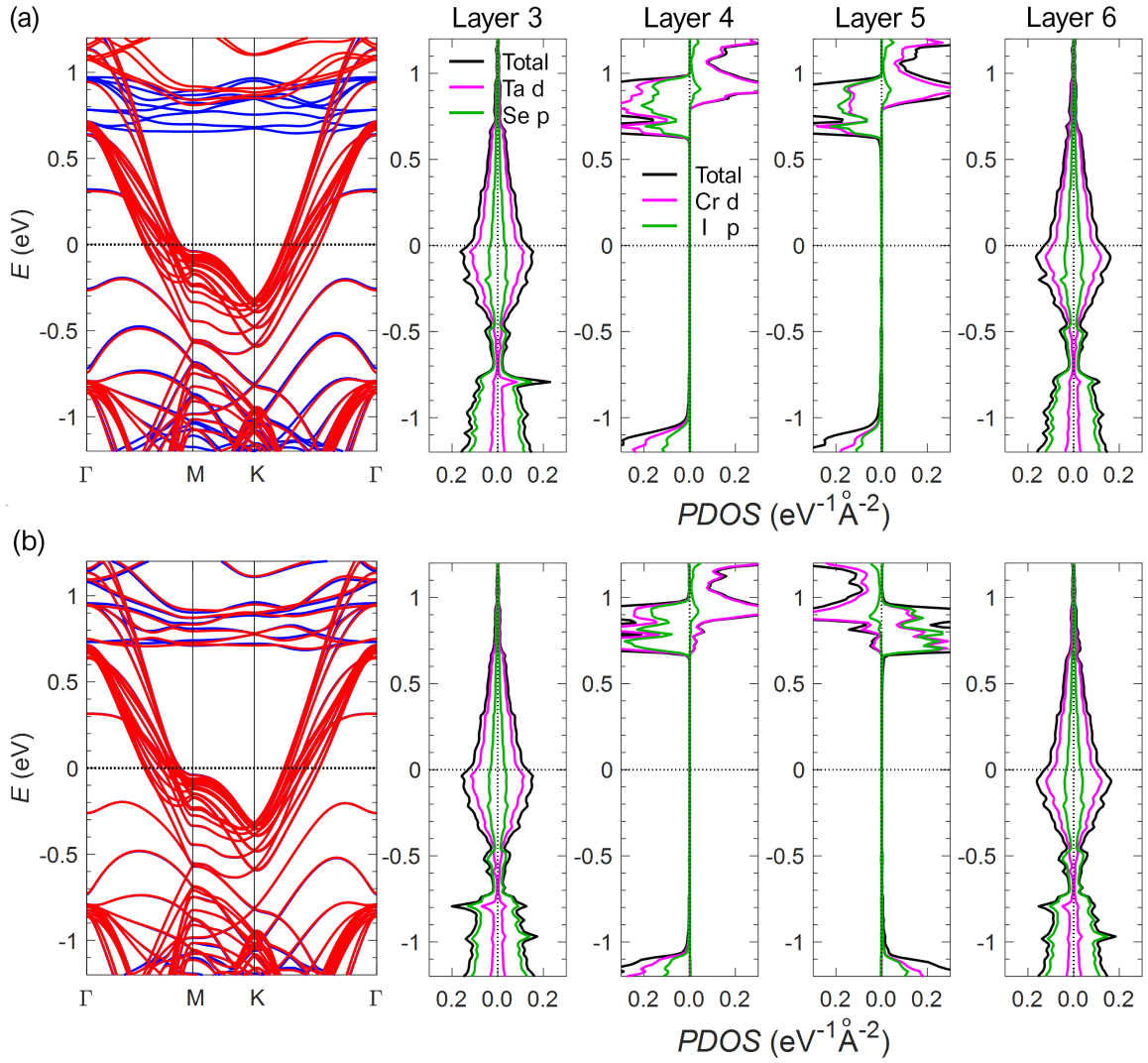

Figure 5.7: Electronic band structures (left) and layer resolved PDOS (right) of the 2H-$TaSe_2$/$CrCl_3$ MTJ in the (a) parallel ↑↑ and (b) antiparallel ↑↓ configurations. Both spin majority (blue; left) and minority (red; right) states are plotted in band structures and the PDOS. Note that the PDOS are normalized based on the area of the junction.

5.4 Transport in 2H-MSe$_2$/CrX_3 Junctions

In Fig. 5.8, we initially examine the available $\mathbf{k}_{\parallel}$-resolved transmission channels (modes) in bulk (2×2)-NbSe$_2$ and 2H-TaSe$_2$ to gauge ideal transmissions. Contrary to the small contours offered by graphene around the K-point, both 2H-NbSe$_2$ and 2H-TaSe$_2$ leads produce states that occupy a vast majority of the hexagonal BZ near the Fermi energy. At the Fermi level, both TMD leads offer the largest transmission about the Γ-point (roughly three modes on average). For increasing energies, available momentum-resolved transmission channels begin to vanish near the K-points followed by diminishes near the M-points for both TMD leads. These vanishing modes consequently produce drops in average transmission as a function of energy.

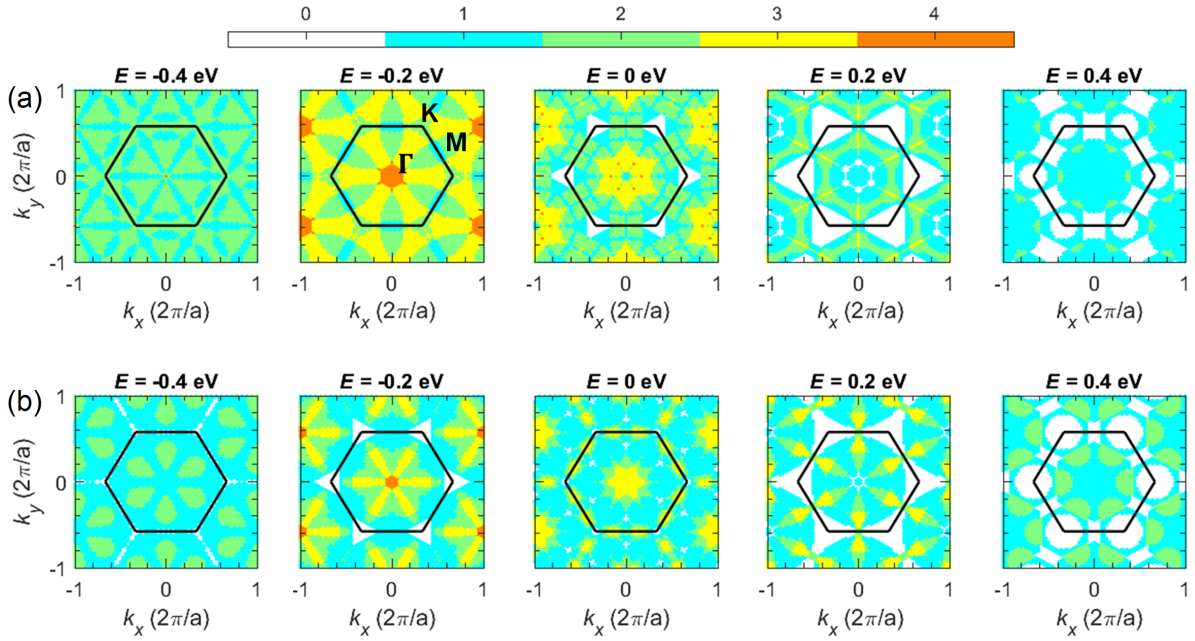

Figure 5.8: Momentum-resolved subband transmissions (modes) across the full hexagonal Brillouin zone (outlined in black) for bulk (a) 2H-NbSe$_2$ and (b) 2H-TaSe$_2$. In each set of plots, the columns (from left to right) correspond to energies E = -0.4, -0.2, 0.0, 0.2 and 0.4 eV. Note that a (2×2)-MSe$_2$ cell is used to match the unit cell of CrI$_3$.

In order to characterize quantum transport in 2H-MSe$_2$/2L-CrX_3 junctions, the conductance is computed from the transmission probability of states in the few-layer 2H-MSe$_2$ leads through the CrX_3 scattering region. As discussed prior in Chapter 3.5, the tunneling current in these systems is a combination of available states in the electrodes and their respective tunneling probabilities. Moreover, the conductance per unit area is computed from the transmission

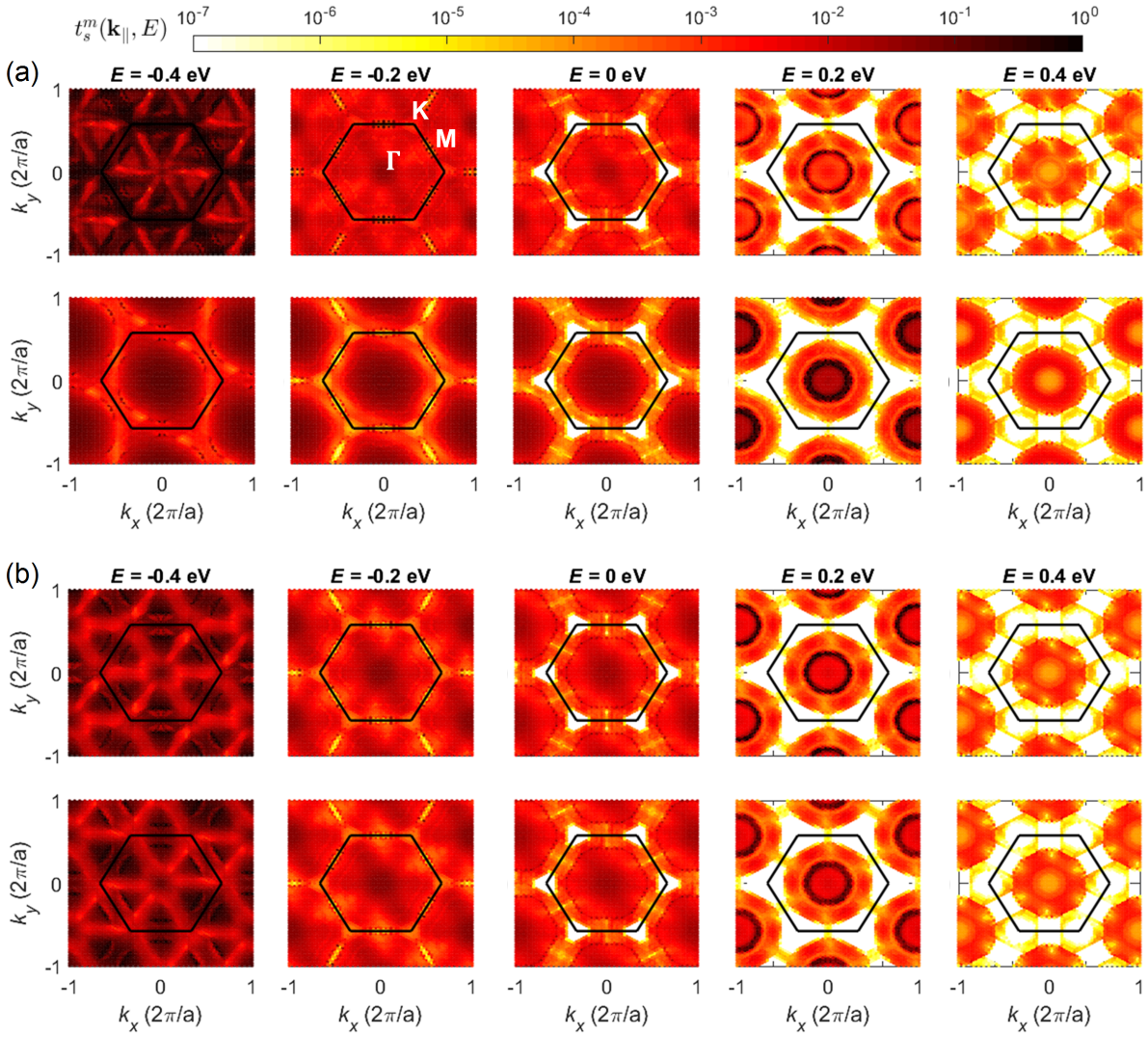

Figure 5.9: Spin and momentum-resolved transmission profiles $[t_s^m(\mathbf{k}_\parallel, E)]$ across the full hexagonal Brillouin zone (outlined in black) for 2H-$NbSe_2$/2L-CrI_3 MTJs in the (a) parallel ($\uparrow\uparrow$) and (b) antiparallel ($\uparrow\downarrow$) configurations. In each set of plots, the top (bottom) row corresponds to the spin majority (minority) channel and columns (from left to right) correspond to energies E = -0.4, -0.2, 0.0, 0.2 and 0.4 eV. A logarithmic scale is provided on top.

probability defined in Eq. 2.22 where $G_0/A \approx 97$ S/μm^2. The transmission probability $T_s^m(E)$ corresponding to a spin channel ($s = \uparrow$ or $\downarrow$) for the system in a metamagnetic state m is calculated according to Eq. 2.23, where all transmissions are standardized based on the unit cell area of CrI_3 over the unit cell area of the heterojunction (A_{CrI_3}/A_{MTJ}).

In Fig. 5.9, we plot the spin and momentum-resolved transmission probabilities $t_s^m(\mathbf{k}_\parallel, E)$ found in Eq. 2.23 for 2H-$NbSe_2$/2L-CrI_3 junctions in the $\uparrow\uparrow$ and $\uparrow\downarrow$ metamagnetic states. Note that these transport calculations are sampled using a 36×36 $\mathbf{k}_\parallel$-grid [191, 192]. For increasing

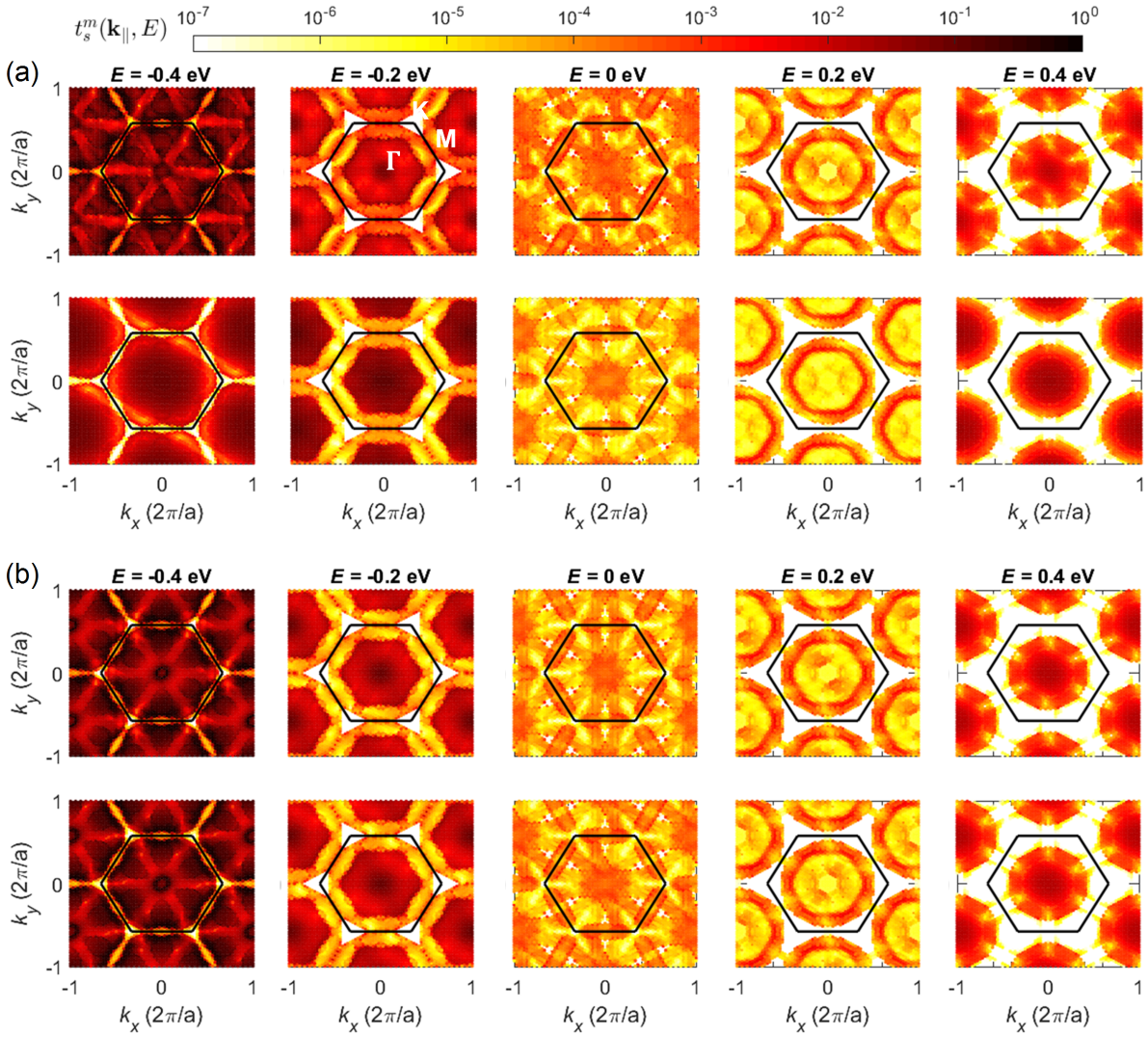

Figure 5.10: Spin and momentum-resolved transmission profiles $[t_s^m(\mathbf{k}_\parallel, E)]$ across the full hexagonal Brillouin zone (outlined in black) for 2H-$TaSe_2$/2L-CrI_3 MTJs in the (a) parallel ($\uparrow\uparrow$) and (b) antiparallel ($\uparrow\downarrow$) configurations. In each set of plots, the top (bottom) row corresponds to the spin majority (minority) channel and columns (from left to right) correspond to energies E = -0.4, -0.2, 0.0, 0.2 and 0.4 eV. A logarithmic scale is provided on top.

energies, momentum-resolved transmissions in 2H-$NbSe_2$/2L-CrI_3 junctions begin to diminish near the K-points followed by the M-points, a consequence of the vanishing modes in the bulk electrodes (Fig. 5.8). Due to the coupling between the TMD leads and the CrI_3 channel, large transmission values encompass the Γ-point at energies close to 0.2 eV, where heavy $NbSe_2$ bands cross (Fig. 5.3). As seen in several energy slices plotted in Fig. 5.9(a), spin minority transmissions in the parallel junction prevail over the spin majority transmissions at or surrounding the Γ-point. As previously demonstrated in the CBS of ferromagnetic CrI_3 in Chapter 3.6 Fig. 3.14 (or upcoming Fig. 5.13), larger spin majority barriers exist along the Γ-A

(perpendicular) direction compared to the spin minority. For the antiparallel (↑↓) configuration [Fig. 5.9(b)], spin minority and majority transmissions are nearly identical; although, small deviations exist due to asymmetric interfaces.

Again, we plot the spin and momentum-resolved transmission probabilities $t_s^m(\mathbf{k}_\parallel, E)$ for 2H-$TaSe_2$/2L-CrI_3 junctions, found in Fig. 5.10. Although the momentum resolved transmissions resemble those in 2H-$NbSe_2$/2L-CrI_3 heterojunctions, spin minority and majority transmissions in 2H-$TaSe_2$/2L-CrI_3 junctions are significantly lower near the Fermi energy. For 2H-$TaSe_2$/2L-CrI_3 junctions in either the ↑↑ or ↑↓ metamagnetic configuration, significant increase in spin transmissions at the Γ-point are observed at higher energies (0.3-0.4 eV) due to heavy $TaSe_2$ bands. Similarly found in 2H-$NbSe_2$/2L-CrI_3 junctions, spin minority and majority transmissions are nearly identical in antiparallel 2H-$TaSe_2$/2L-CrI_3 junctions [Fig. 5.10(b)].

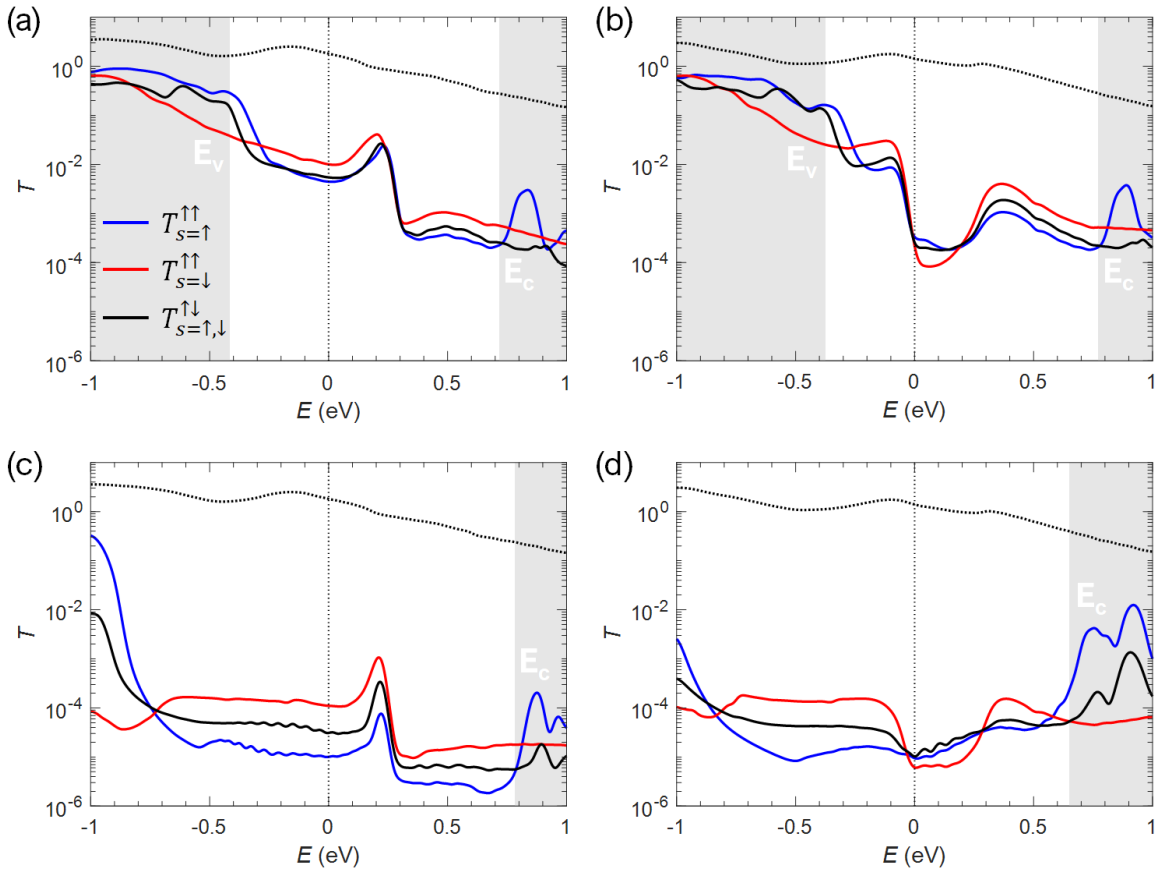

Figure 5.11: Transmission probabilities through (a) 2H-$NbSe_2$/2L-CrI_3, (b) 2H-$TaSe_2$/2L-CrI_3, (c) 2H-$NbSe_2$/2L-$CrCl_3$, and (d) 2H-$TaSe_2$/2L-$CrCl_3$ based MTJs in the parallel ↑↑ (blue; red) and antiparallel ↑↓ (black) configurations, where all transmissions are normalized by A_{CrI_3}/A_{MTJ}. The corresponding bulk 2H-MSe_2 transmission is marked by a dotted line. Both the valence (E_v) and conductance (E_c) band edges of CrX_3 are denoted.

Next, the net spin transmissions $T_s^m(E)$ through bilayer CrI_3 MTJs as a function of the electron energy for parallel and antiparallel configurations are produced in Fig. 5.11 using Eq. 2.23, where the CrX_3 band edges are marked for convenience. We plot both spin up (blue) and down (red) channels for junctions in the ↑↑ configuration, while we average spin channels (black) for the ↑↓ configuration due to minor differences between spin transmissions. Additionally, we apply Fermi-Dirac smoothing to all transmission curves with a broadening term of $k_BT = 0.01$ eV.

Regarding 2H-MSe$_2$/2L-CrI_3 (M = Nb and Ta) junctions in the ↑↑ or ↑↓-state [Fig. 5.11(a)-(b)], net transmissions drop beyond the VBE of CrI_3 and into the gap. Apart from transmission drops due the semiconducting barrier, spin transmissions exhibit an overall downward trend for increasing energy due to the vanishing modes in the electrodes. As seen by the dotted lines in Fig. 5.11(a)-(b), spin transmissions in bulk 2H-$NbSe_2$ and 2H-$TaSe_2$ electrodes slowly diminish over energy. Moreover, spikes in spin majority (blue) transmissions occur just above the CrI_3 CBE in parallel (↑↑) junctions, while minority (red) transmissions prevail throughout most of the gap. For energies just above the Fermi level (∼0.2 eV), spin transmissions dramatically increase in 2H-$NbSe_2$/2L-CrI_3 heterojunctions [Fig. 5.11(a)]. Contrarily, spin transmissions dramatically dip in 2H-$TaSe_2$/2L-CrI_3 junctions for energies just above the Fermi level [Fig. 5.11(b)]. As mentioned prior, the increase in spin transmissions just above the Fermi energy in 2H-$NbSe_2$/2L-CrI_3 junctions is due to coupling between the leads and channel, which results in MIGS. Just above the Fermi level in 2H-$TaSe_2$/2L-CrI_3 junctions, a dip in available transmission modes in the $TaSe_2$ electrode itself [dotted line in Fig. 5.11(b)] is further accentuated by the CrI_3 barrier, producing large drops in spin transmissions.

For the 2H-MSe$_2$/2L-$CrCl_3$ junctions [Fig. 5.11(c)-(d)], spin transmissions significantly drop beyond the VBE of $CrCl_3$ and into the gap. As demonstrated in the 2H-$NbSe_2$/2L-CrI_3 system, the 2H-$NbSe_2$/2L-$CrCl_3$ junction in the ↑↑ or ↑↓-state exhibits spikes in spin transmissions just above (∼0.2 eV) the Fermi energy due the presence of MIGS [Fig. 5.11(c)]. Likewise, 2H-$TaSe_2$/2L-$CrCl_3$ junctions display dips in spin transmission above the Fermi level caused by vanishing modes in the electrode [Fig. 5.11(d)]. The disparity between spin majority (blue)

and minority (red) transmission in parallel (↑↑) 2H-MSe$_2$/2L-CrX_3 junctions increases by substituting bilayer CrI_3 with bilayer $CrCl_3$ channels. Furthermore, 2H-MSe$_2$/2L-CrI_3 junctions are capable of producing 100 times greater transmission than 2H-MSe$_2$/2L-$CrCl_3$ junctions and nearly 1,000 times greater transmission than Gr/2L-CrI_3 junctions [Fig. 3.11(b)-(c)].

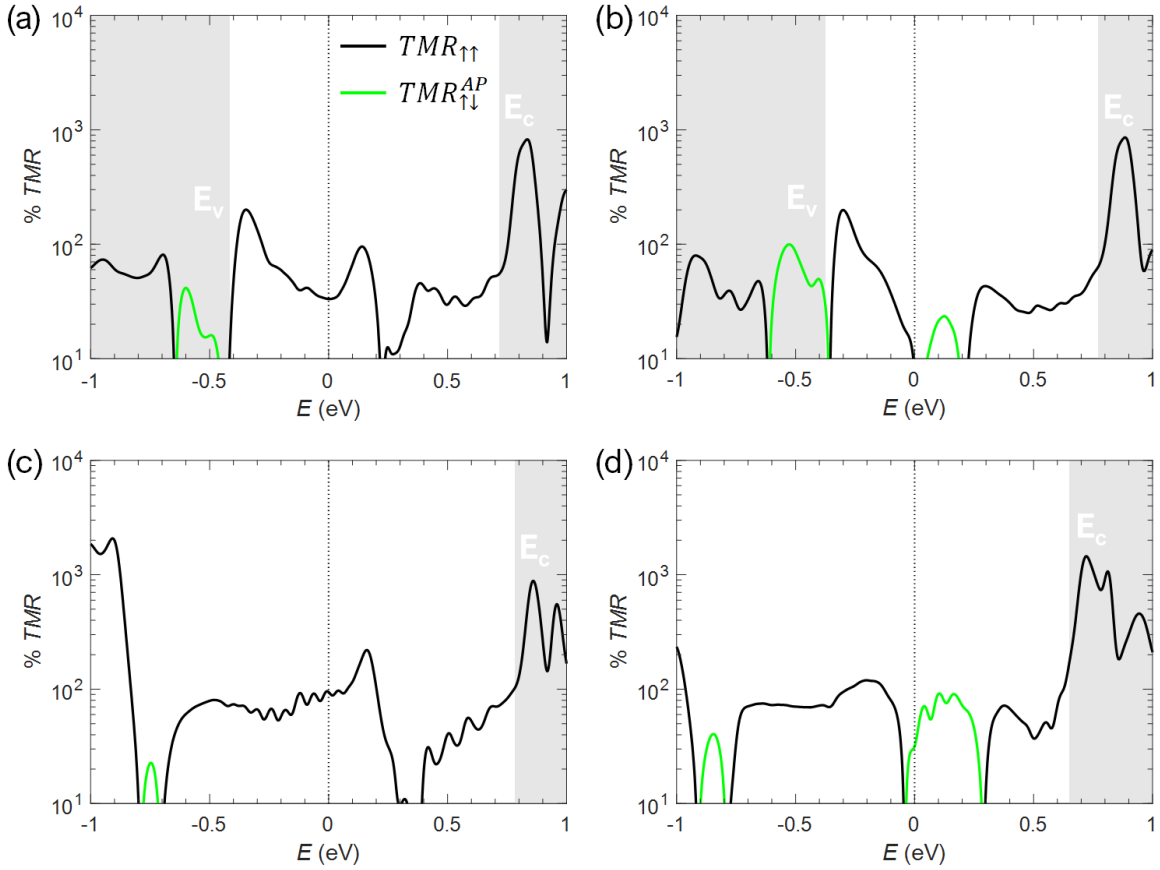

Figure 5.12: TMR values in (a) 2H-NbSe$_2$/2L-CrI_3, (b) 2H-TaSe$_2$/2L-CrI_3, (c) 2H-NbSe$_2$/2L-$CrCl_3$, and (d) 2H-TaSe$_2$/2L-$CrCl_3$ based MTJs. The TMR for the ↑↑-state is plotted in black while the TMR for the ↑↓-state (in reference to the parallel) is plotted in green. Both the valence (E_v) and conductance (E_c) band edges of CrX_3 are denoted.

Assuming a MTJ in the parallel (↑↑) configuration produces a low resistance state, the TMR is defined by Eq. 3.4. If the antiparallel (↑↓) configuration produces the low resistance state, the TMR is redefined:

$$\mathrm{TMR}_m^{AP} = \frac{(T_\uparrow^m + T_\downarrow^m) - (T_\uparrow^P + T_\downarrow^P)}{T_\uparrow^P + T_\downarrow^P}, \tag{5.1}$$

where the parallel (P) configuration serves as reference. In Fig. 5.12, both $\mathrm{TMR}_{\uparrow\uparrow}$ (black) and $\mathrm{TMR}_{\uparrow\downarrow}^{AP}$ (green) are plotted for each 2H-MSe$_2$/2L-CrX_3 junction. Based on Eq. 3.4 or Eq. 5.1, the magnetoresistance computed at the Fermi energy for 2H-NbSe$_2$/2L-CrI$_3$ and 2H-TaSe$_2$/2L-CrI$_3$ junctions are $\mathrm{TMR}_{\uparrow\uparrow} \approx 30\%$ and $\mathrm{TMR}_{\uparrow\uparrow} \approx 10\%$, respectively. Likewise, the magnetoresistance computed at the Fermi energy for 2H-NbSe$_2$/2L-CrCl$_3$ and 2H-TaSe$_2$/2L-CrCl$_3$ junctions are $\mathrm{TMR}_{\uparrow\uparrow} \approx 90\%$ and $\mathrm{TMR}_{\uparrow\downarrow}^{AP} \approx 30\%$, respectively. The magnetoresistance values in these 2H-MSe$_2$/2L-CrX_3 MTJs are slightly lower or comparable to experimental values ($\mathrm{TMR}_{\uparrow\uparrow} \approx$ 50-100%) in Gr/2L-CrI$_3$ based devices [7, 108]. Moreover, giant TMR values in 2H-MSe$_2$/2L-CrX_3 junctions are observed near CrX_3 band edges as seen in Gr/2L-CrI$_3$ junctions (Fig. 3.15) due to the overlap between metal and CrX_3 states. For 2H-NbSe$_2$/2L-CrI$_3$ and 2H-NbSe$_2$/2L-CrCl$_3$ junctions [Fig. 5.12(a) and (c)], large TMR on the order of 100% exists roughly 0.2 eV above the Fermi level due to the coupling between the leads and channel. We note that coupling in 2H-NbSe$_2$/2L-CrX_3 heterojunctions may be epitaxially dependent.

5.5 Transport Approximations via Complex Wavevectors

The 2H-MSe$_2$/CrX_3 interfaces constructed in this chapter posses highly commensurate epitaxies, however, many lead materials do not form basic interfaces with CrX_3. In order to approximate transmissions through CrX_3 (X = Br and I) channels with ideal metal leads (regardless of epitaxy), we compute $\mathbf{k}_\parallel$-resolved (12×12 k-point mesh) energy dependent decay rates of evanescent wave functions in bulk CrX_3 for both parallel and antiparallel magnetic configurations as previously demonstrated for CrI$_3$ in Chapter 3.6. In Fig. 5.13, we present the perpendicular complex wavevectors in bulk (a) CrBr$_3$ and (b) CrI$_3$ for both parallel and antiparallel magnetic configurations with respect to Γ, K, and M hexagonal symmetry points, where the spin majority (blue) and minority (red) wavevectors in ferromagnetic CrX_3 are superimposed on the spin majority/minority (gray) wavevectors in antiferromagnetic CrX_3 (Fig. 5.13). The CBS of both parallel and antiparallel CrX_3 configurations are aligned by their midgap energies.

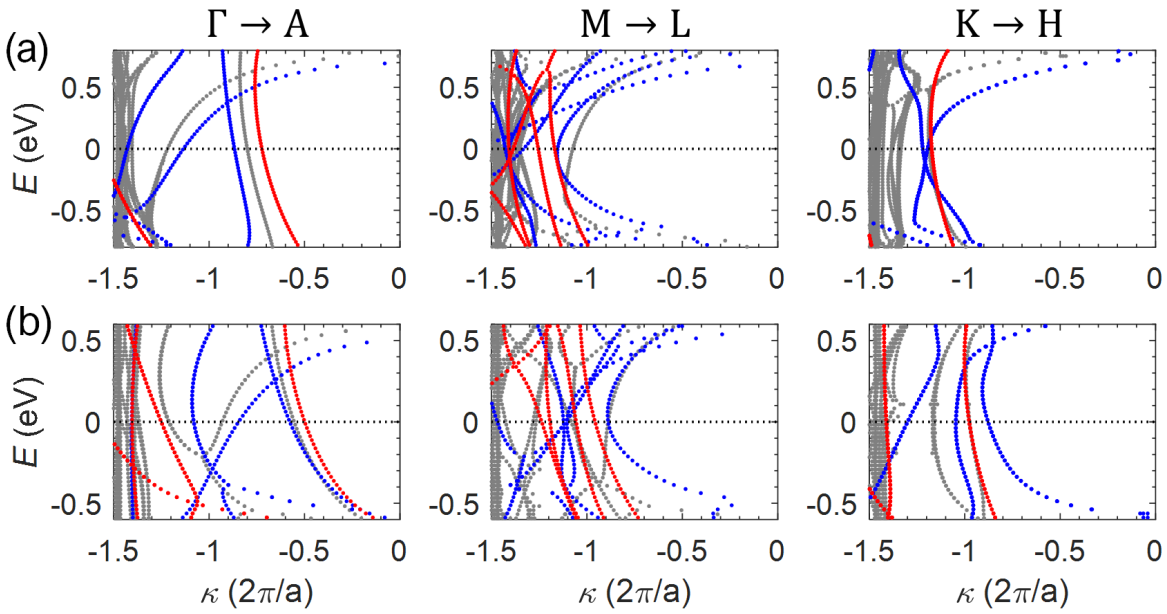

Figure 5.13: Perpendicular imaginary wavevectors to the hexagonal BZ plane for bulk (a) $CrBr_3$ and (b) CrI_3. Gray lines represent majority/minority evanescent states produced in the antiparalell configuration (↑↓↑↓↑↓), which have been scaled to reflect a three layer unit cell. Blue (red) lines represent majority (minority) evanescent states produced in the paralell configuration (↑↑↑).

We note that antiferromagnetic cases are constructed using six layers of CrX_3 (↑↓↑↓↑↓) versus three layers for the ferromagnetic case (↑↑↑). We find that bulk $CrBr_3$ [Fig. 5.13(a)] produces stronger spin barriers than bulk CrI_3 [Fig. 5.13(b)] for energies within its band gap. This is due to $CrBr_3$ possessing a larger band gap than CrI_3, in which longer (more negative) complex wavevectors κ are produced within its gap. Moreover, wavevectors (blue and red) produced in ferromagnetic bulk $CrBr_3$ are appreciably closer to the wavevectors (grey) produced in the antiferromagnetic case compared to those in CrI_3 (Fig. 5.13). For ferromagnetic CrX_3 (X = Br and I), spin minority (red) barriers are comparable or shorter than the spin majority (blue) perpendicular to the Γ-point, enabling greater spin minority transmission.

Using Eq. 3.5, we estimate spin-resolved transmissions through NL-CrX_3 (N = 2, 3, and 4) channels. We denote transmission estimates using complex wavevectors as $\widetilde{T}_s^m(E)$, where all spin transmissions for $CrBr_3$ systems are normalized by the unit cell area of CrI_3 ($A_{\mathrm{CrI_3}}/A_{\mathrm{CrBr_3}}$). In Fig. 5.14, spin-resolved transmission values $\widetilde{T}_s^m(E)$ for N-layer CrX_3 channels in parallel (blue and red) and antiparallel (black) configurations are plotted as a function of energy. In both $CrBr_3$ and CrI_3 channels, spin transmissions diminish for energies beyond the valence

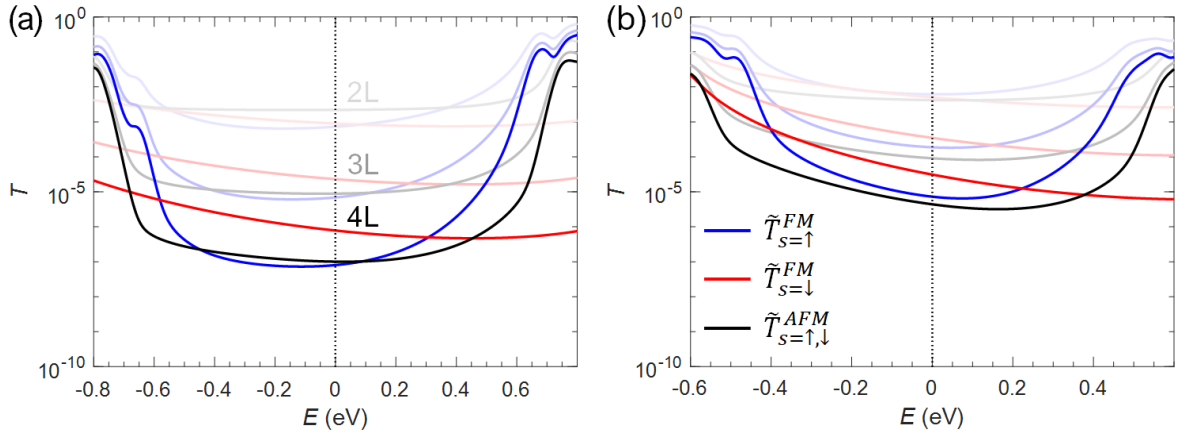

Figure 5.14: Approximate transmission probabilities using bulk properties through N-layers (N = 2, 3, and 4) of (a) $CrBr_3$ and (b) CrI_3 for the parallel (blue; red) and antiparallel (black) configurations, where all transmissions in $CrBr_3$ systems are normalized by A_{CrI_3}/A_{CrBr_3} while bilayer, trilayer, and tetralayer systems are colored from faint to dark, respectively. Note that all transmission curves are centered around the middle of the CrX_3 band gap.

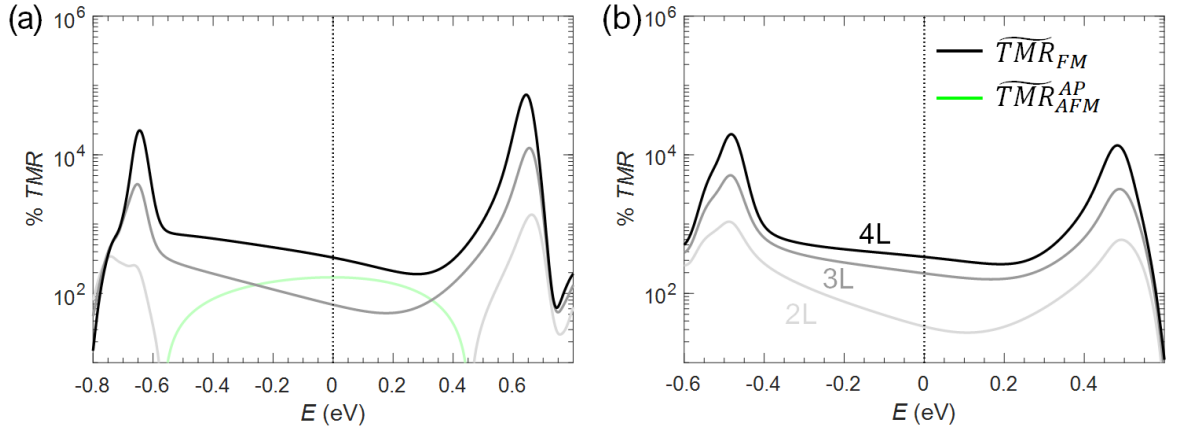

Figure 5.15: Approximate TMR using bulk properties through N-layers (N = 2, 3, and 4) of (a) $CrBr_3$, and (b) CrI_3, where TMR_m is plotted in black while TMR^{AP}_m is plotted in green. Bilayer, trilayer, and tetralayer systems are colored from faint to dark, respectively.

band edges (VBEs) and into the gap (Fig. 5.14), where longer complex wavevectors reside. For parallel configurations, spin minority (red) transmissions prevail over the spin majority (blue) for energies just above the VBE of CrX_3 (X = Br and I). Moreover, spin transmissions (black) in antiparallel junctions are comparable to spin majority transmissions (blue) in parallel cases for energies near the middle of the gap (Fig. 5.14). For consecutively thicker CrI_3 channels, spin transmissions decrease roughly by an order of magnitude for every additional layer as seen in Fig. 5.14(b). Due to larger spin barriers produced in $CrBr_3$, spin transmissions in

$CrBr_3$ channels decrease nearly two orders of magnitude for every additional layer as seen in Fig. 5.14(b). Spin transmission estimates $\widetilde{T}_s^m(E)$ close to the Fermi level for ferromagnetic bilayer CrI_3 [Fig. 5.14(b)] are comparable in magnitude to spin transmissions $T_s^m(E)$ (blue and red) found in the 2H-$NbSe_2$/2L-CrI_3 MTJ [Fig. 5.11(a)].

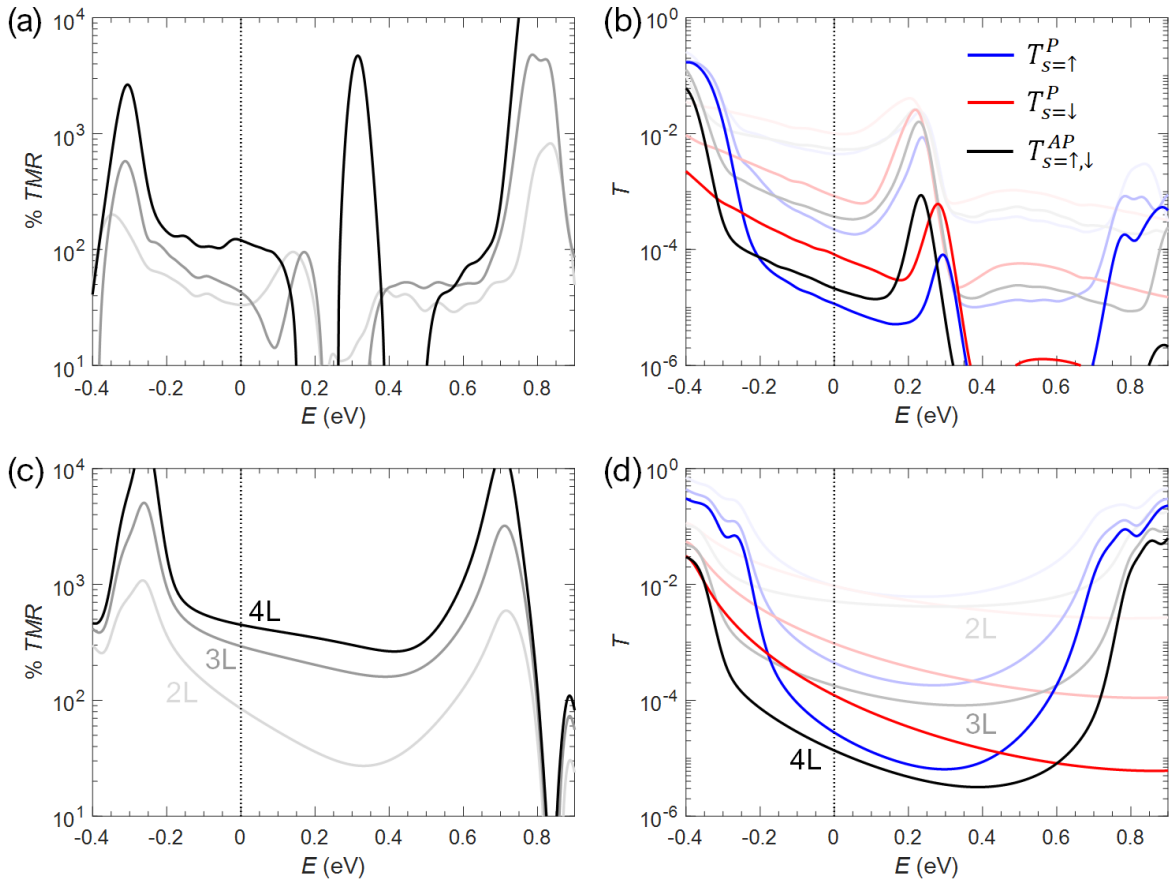

Figure 5.16: Calculated (a) TMR_m and (b) spin transmission in 2H-$NbSe_2$/NL-CrI_3 junctions as well as estimated (c) TMR_m and (d) spin transmission through N-layers (N = 2, 3, and 4) of bulk CrI_3. Bilayer, trilayer, and tetralayer systems are colored from faint to dark, respectively.

Furthermore, spin transmissions $\widetilde{T}_s^m(E)$ based on the CBS of bulk CrX_3 (X = Br and I) are used to estimate energy dependent TMR in ideal NL-CrX_3 (N = 2, 3, and 4) channels. In Fig. 5.15, both TMR_m (black) and TMR_m^{AP} (green) are plotted for $CrBr_3$ and CrI_3 channels using CBS derived transmissions. Regarding bilayer approximations (faint lines), TMR on the order of 100% or greater is observed near the CrX_3 band edges (Fig. 5.15), in good agreement with TMR found in 2H-MSe_2/2L-CrX_3 junctions (Fig. 5.12). Within the CrX_3 band gaps, a significant competition exists between net transmission through parallel versus antiparallel channels. As seen in 2H-$TaSe_2$/2L-CrI_3 and 2H-$TaSe_2$/2L-$CrCl_3$ junctions [Fig. 5.12(b) and

(d)], spin transmissions in antiparallel (↑↓) configurations prevail over those in parallel (↑↑) configurations slightly above the Fermi level.

As the number of CrX_3 layers are increased in each system, spin transmissions in the parallel CrX_3 (X = Br and I) junction begin to dominate (Fig. 5.15). These transmission disparities between the two magnetic states consequently leads to increases in TMR for thicker junctions while simultaneously results with drops in net transmission. To illustrate this phenomenon, we calculate the magnetoresistances in 2H-$NbSe_2$/NL-CrI_3 (N = 2, 3, and 4) based MTJs as seen in Fig 5.16. For reference, we plot the TMR derived through CBS estimates under the results for 2H-$NbSe_2$/NL-CrI_3 junctions. Although deviations exist due to varying state overlap between leads and channel and the formation of MIGS, which causes transmission spikes above the Fermi level, overall TMR trends in 2H-$NbSe_2$/NL-CrI_3 heterojunctions mimic bulk CBS approximations [Fig. 5.15(a) and (b)]. Moreover, drops in spin transmissions as a function of channel thickness in 2H-$NbSe_2$/CrI_3 systems can also be roughly estimated using bulk CBS approximations [Fig. 5.16(b) and (d)].

5.6 Alternative TMD Electrode Search

Apart from being one of the most widely studied 2D material families [258], transition metal dichalcogenides (TMDs) offer a large array of combinations between Group III-XII and Group XVI elements, in addition to various polymorphs. Based on band alignments found prior in the 2H-MSe_2/2L-CrI_3 junctions and preknowledge of the CBS of bulk CrI_3, we investigate alternative TMD leads with significantly higher and lower work functions. By choosing TMD materials that offer higher (lower) work functions, a boost in TMR is expected for resulting Fermi level alignments close to the VBE (CBE) of CrI_3. In order to determine sufficient TMD candidates for electrode materials, we developed a high-throughput material workflow that computes relative stabilities and work functions of all monolayer TMDs MX_2 (X = S, Se, and Te) in the 1H, 1T, 1T', and Pbca phases as seen in Fig. 5.17.

In the workflow, lattice parameters for TMDs with a set chalcogenide and phase are initially extracted from the open-source Automatic - FLOW for Materials Discovery (AFLOW) repository [259]. Remaining structures with unknown lattice parameters are estimated based

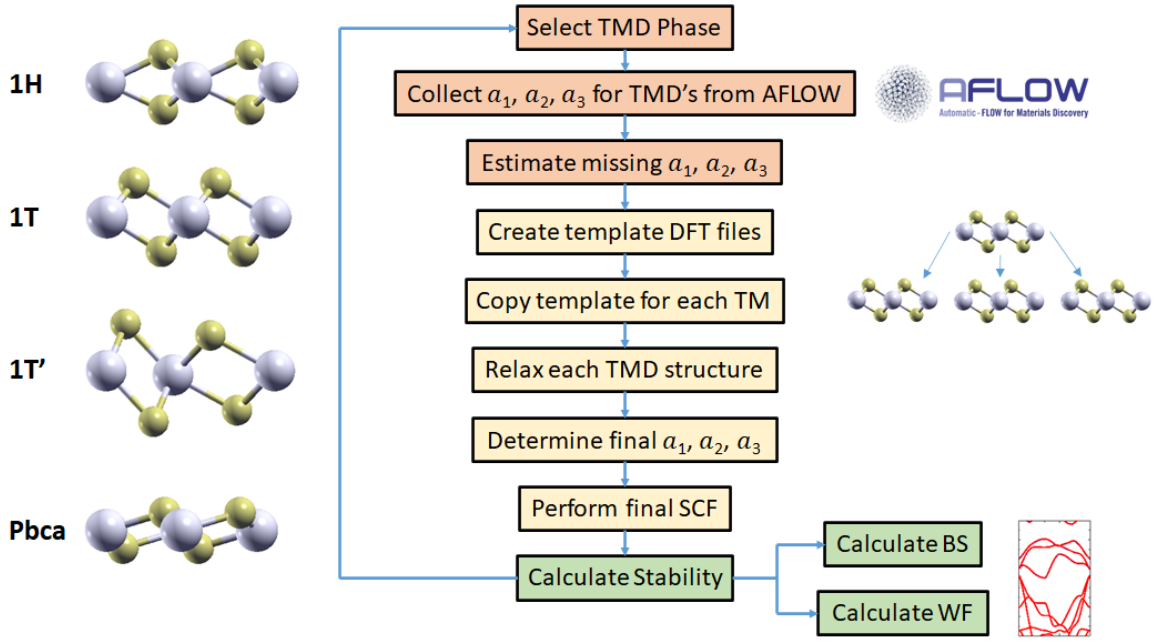

Figure 5.17: Material (TMD) computational workflow used to compute relative energies, lattice parameters, atomic geometries, and work functions in mass.

on periodic table groups. For each chalcogenide and phase, a Quantum Espresso [171] template input file is copied then modified to reflect the appropriate material. Based on these input files, atomic relaxation calculations are performed in order to solve for the equilibrium configurations. Lastly, a final SCF calculation is performed using the relaxed TMD structure to determine relative energies or additional quantities such as the work function.

All first principles calculations are carried out using the Quantum Espresso software [169, 170, 171, 172], where the exchange-correlation energy is parameterized by spin polarized generalized gradient approximation (PBE) functionals [173] including dispersion forces (vdW-DF-C09) [174, 175, 176]. Atomic cores are characterized via projector augmented wave (PAW) pseudopotentials [177, 178] with cutoff energies of 75 Ry and 750 Ry regarding the Kohn-Sham wave functions and densities, respectively. The 2D-BZ is sampled using a 30×30 Monkhorst-Pack mesh [190], where BZ integration is performed using the tetrahedron method [226, 227]. The convergence thresholds of total energy and forces for ionic minimization is set to their default values of 1.0×10^{-4} Ry and 1.0×10^{-3} Ry$\cdot a_0^{-1}$, respectively. The convergence

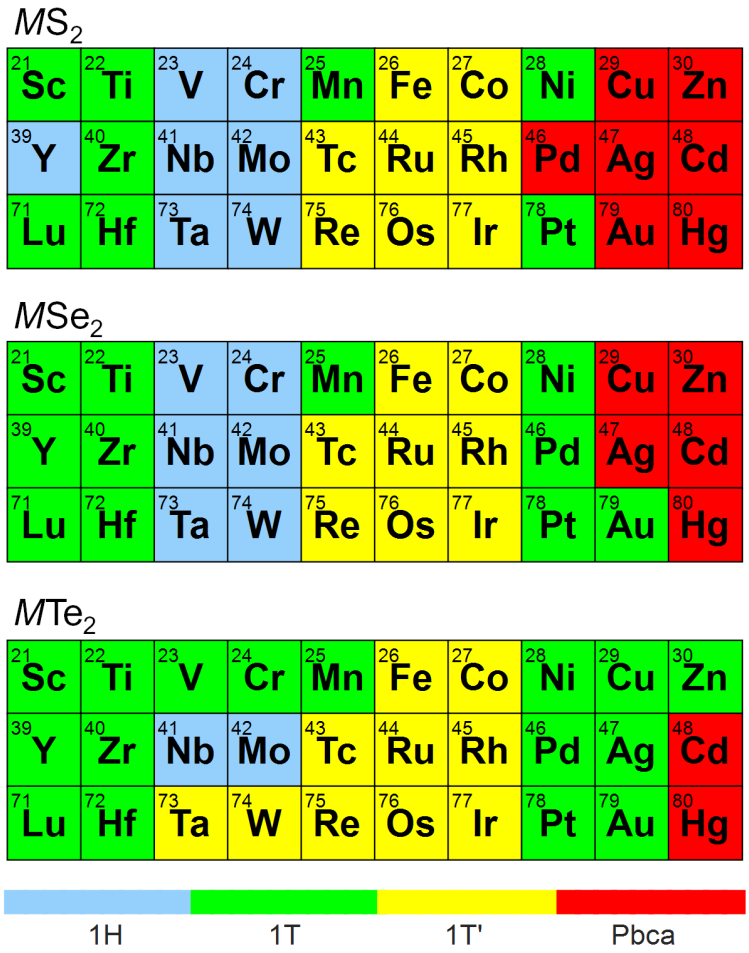

Figure 5.18: Most stable monolayer TMD polymorphs calculated using PBE functionals displayed in a periodic table format. Elements within the periodic table denote the respective transition metals M.

threshold for self-consistent calculations are set to their default of 1.0×10^{-6} Ry. Due to periodic boundary conditions, at least 15 Å of perpendicular vacuum space is set in TMD unit cells.

In Fig. 5.18, the most stable (via PBE functionals) MX_2 (X = S, Se, and Te) structures are provided. Based on their relative energies, TMDs consisting of Groups III and IV transition metals (TMs) mainly adopt the 1T structure while TMDs consisting of Groups V and VI metals prefer the 1H phase. By continuing down the periods, TMDs adopt the 1T' followed by the 1T and lastly the Pbca phase. As previously reported in a past study [260], TMD phases are determined by ligand field splitting in which the splitting of the t_{2g} orbital leads to trigonal prismatic geometry (1H phase). Next, we identify which of the most stable structures are

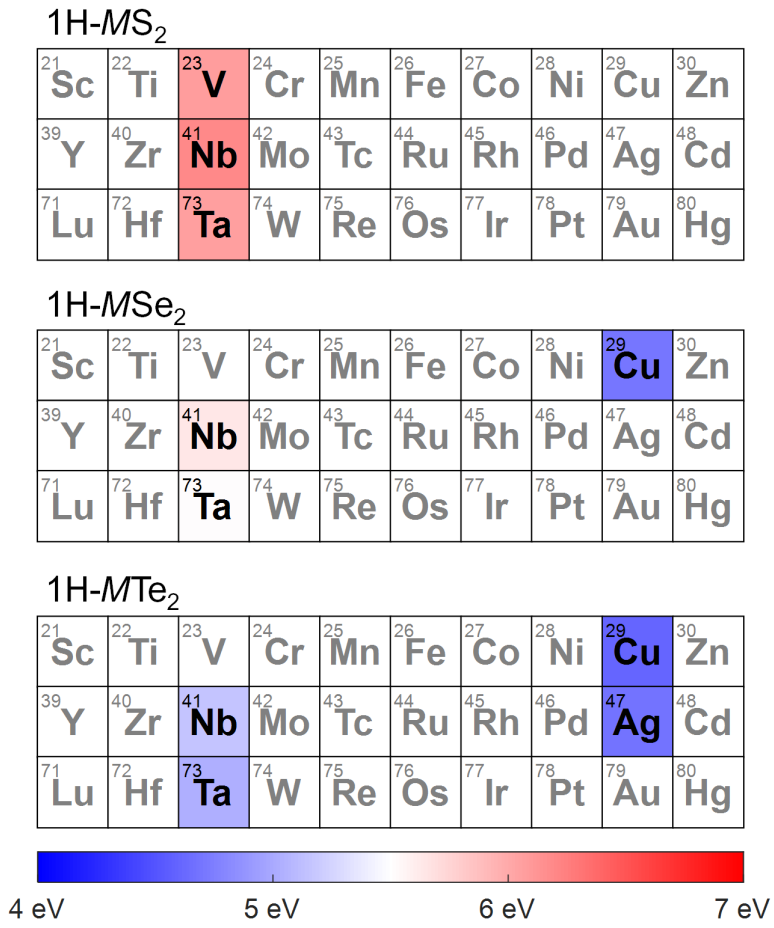

Figure 5.19: Most stable monolayer TMD found in the 1H phase and predicted to be metallic based on PBE functionals, displayed in a periodic table format. Note that 1H polymorphs with energy differences within 0.1 eV per formula of the most stable phase are also included. Elements within the periodic table denote the respective transition metals M, where a cell's color indicates the TMD work function while a transparent symbol color indicates lower stability.

metallic, including any polymorphs with energy differences smaller than 0.1 eV per formula compared to the most stable phase. The work functions for all predicted stable metals in the 1H and 1T are presented in Fig. 5.19 and Fig. 5.20, respectively. Work functions in these monolayer systems are calculated as the difference between the Fermi energy and the vacuum level as described in Chapter 4.5.

As illustrated in Fig. 5.19, only TM elements belonging to Groups V and XI are predicted to form metallic TMDs in the 1H phase. Moreover, heavier chalcogenide systems in the 1H phase produce lower work functions. As seen in Fig. 5.20, significantly more TM elements are capable of forming metallic TMDs in the 1T phase. As similarly found for the 1H structures, heavier chalcogenide systems in the 1T phase also produce lower work functions. By cross

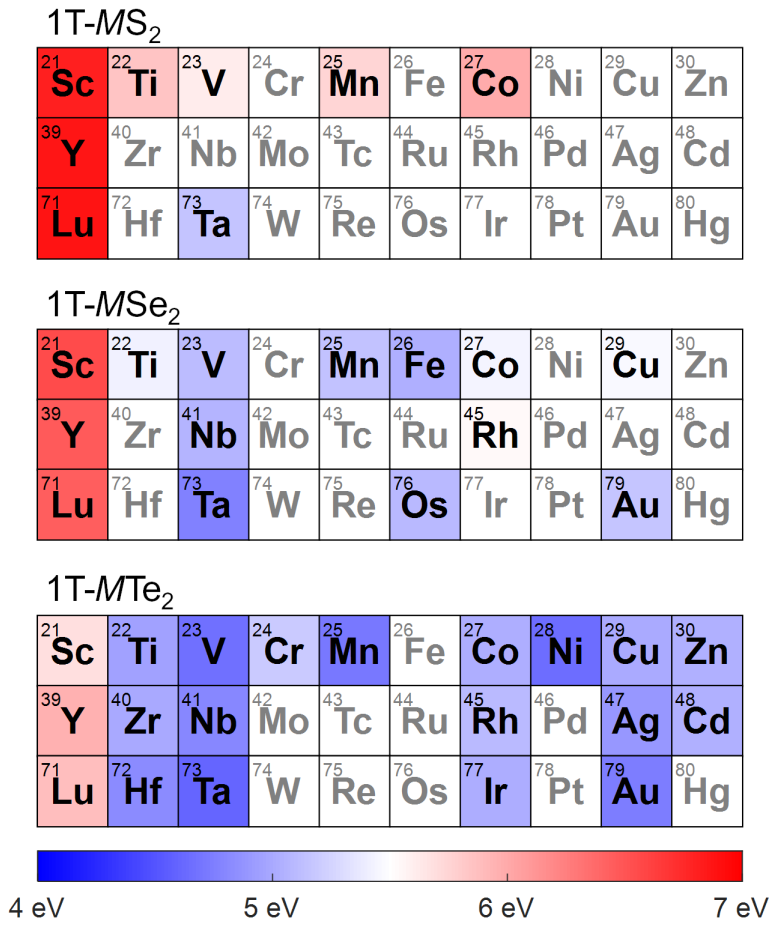

Figure 5.20: Most stable monolayer TMD found in the 1T phase and predicted to be metallic based on PBE functionals, displayed in a periodic table format. Note that 1T polymorphs with energy differences within 0.1 eV per formula of the most stable phase are also included. Elements within the periodic table denote the respective transition metals M, where a cell's color indicates the TMD work function while a transparent symbol color indicates lower stability.

referencing our list of stable metals with those found experimentally, we find that 1T-$TaSe_2$ with one of the lowest calculated WF ($\sim$ 4.8 eV) and 1H-TaS_2 with one of the highest calculated WF ($\sim$ 6.1 eV) form fairly commensurate (2×2) epitaxies with (1×1)-CrI_3 (Table 5.1). Note that commensuration between these vdW materials is not a restraint in practice, rather a computational limitation.

5.7 Low and High Work Function TMD Junctions

Again, we calculate the transmission probability $T_s^m(E)$ corresponding to a spin channel s ($\uparrow$ or $\downarrow$) for 1T-$TaSe_2$/*N*L-CrI_3 and 2H-TaS_2/*N*L-CrI_3 (*N* = 2 and 4) MTJs in a metamagnetic state m using Eq. 2.23. In Fig. 5.21(a), we present both TMR_m (black) and TMR_m^{AP} (green) using Eqs. 3.4 and 5.1 for CrI_3 junctions with low work function 1T-$TaSe_2$ electrodes. Additionally, spin transmissions for 1T-$TaSe_2$/CrI_3 junctions in parallel (blue and red) and antiparallel (black) configurations are plotted in Fig. 5.21(b). By selecting a low work function TMD, the resulting Fermi level resides close to the CBE of CrI_3, where sizable increases in spin transmissions are observed in CBS estimates. As a result, TMR values of $TMR_{\uparrow\uparrow} \approx 80\%$ and $TMR_{\uparrow\uparrow\uparrow\uparrow} \approx 420\%$ are achieved in 1T-$TaSe_2$/2L-CrI_3 and 1T-$TaSe_2$/4L-CrI_3 junctions at the Fermi energy [Fig. 5.21(a)], consistent with CBS estimates near the band edge [Fig. 5.15(b)]. The 1T-$TaSe_2$/2L-CrI_3 junction produces a TMR value comparable to that of the Gr/2L-CrI_3 MTJ at the Fermi energy, yet offers two orders of magnitude greater spin transmissions. Furthermore, the 1T-$TaSe_2$/4L-CrI_3 junction produces comparable spin transmissions to that of the Gr/2L-CrI_3 MTJ, yet offers four times larger TMR at the Fermi level.

Similarly, we present both the TMR and spin transmission curves for CrI_3 junctions with high work function 2H-TaS_2 electrodes in Fig. 5.21(c) and (d), respectively. By choosing a high work function TMD, the resulting Fermi level falls nearly at the VBE of CrI_3. TMR values of $TMR_{\uparrow\uparrow} \approx 60\%$ and $TMR_{\uparrow\uparrow\uparrow\uparrow} \approx 120\%$ are achieved in 2H-TaS_2/2L-CrI_3 and 2H-TaS_2/4L-CrI_3 junctions at the Fermi energy, respectively. Although a slightly lower TMR value is produced in the 2H-TaS_2/2L-CrI_3 junction compared to the Gr/2L-CrI_3 MTJ at the Fermi level, the 2H-TaS_2/2L-CrI_3 junction offers nearly 1,000 times greater spin transmissions. Moreover, the thicker 2H-TaS_2/4L-CrI_3 junction offers a comparable TMR to the Gr/2L-CrI_3 MTJ at the Fermi energy, yet produces 100 times greater spin transmissions.

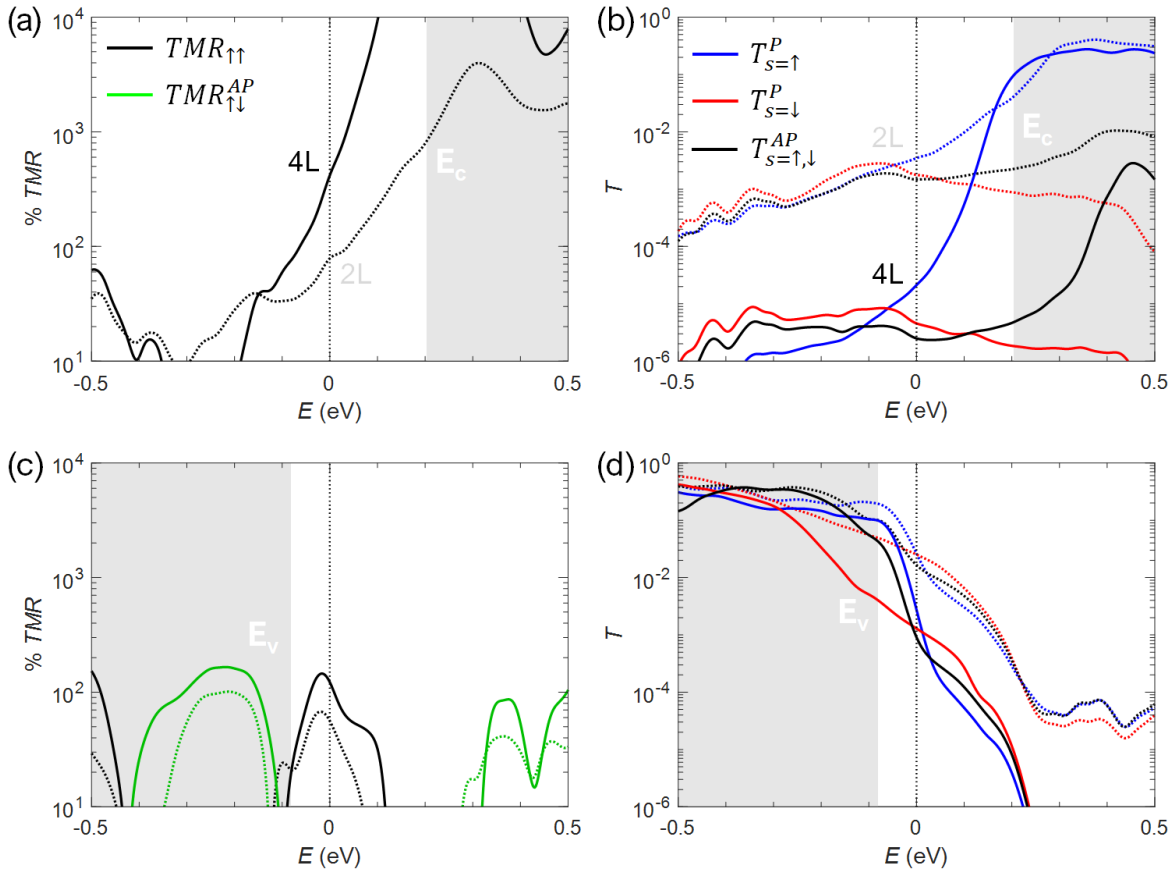

Figure 5.21: Calculated (a) TMR and (b) spin transmissions in 1T-$TaSe_2$/NL-CrI_3 junctions and the calculated (c) TMR and (d) spin transmissions in 2H-TaS_2/NL-CrI_3 junctions (N = 2 and 4). Note that TMR and transmission curves for bilayer junctions are indicated by dashed lines while TMR and transmission curves for tetralayer junctions are denoted by solid lines.

Chapter 6

Summary and Outlook

Regarding the published work in Chapter 3, our study was the first to characterize graphene (Gr)/NL-CrI_3 (N = 1, 2, 3) based magnetic tunnel junctions (MTJs) using first principles calculations within the density functional theory and Landauer's formalism for ballistic transport. Through our analysis of the electronic band structure of few-layer CrI_3 junctions, we find that tunneling is the primary transport mechanism based on Gr/CrI_3 band alignments, consistent with experimental findings. Furthermore, metamagnetic dependent band gaps (spin barriers) are observed in few-layer CrI_3 for isolated or heterojunction systems due to quantum confinement and interlayer magnetic coupling. Consequently, these small changes in band alignments due to the magnetic order of the CrI_3 channel significantly impact spin-resolved transmission probabilities in Gr/CrI_3 junctions. Additionally, we show that average transmissions in trilayer junctions are roughly characterized by the complex band structure (CBS) of bulk CrI_3 for each respective magnetic state. Based on our ballistic transport calculations, we calculate tunneling magnetoresistance (TMR) values in remarkable agreement to experiment for bilayer and trilayer MTJs.

In Chapter 4, we characterize electronic band alignments in low-strain NL-Gr/CrX_3 (N = 1, 2, 3; X = F, Cl, Br, I) heterojunctions via ACBN0 pseudohybrid Hubbard density functionals, which enable self-consistent Hubbard corrections to be applied to these large systems. We find that CrX_3 with lighter halides promotes greater charge transfer with adjacent graphene layers, producing a significant charge screening effect in multilayer graphene. Due to the sizable charge transfer in Gr/CrF_3 systems, conduction band splitting is observed in CrF_3 d-states. Additionally, the AB (ABA)-Gr/CrF_3 heterojunction exhibits the formation of a graphene band

gap of 173 meV (104 meV) due in part to the Stark effect. We also find that an increase in the number of graphene layers transforms several Gr/CrX_3 Ohmic junctions into Schottky contacts, requiring no external field or force to be applied. Furthermore, we provide an intuitive electrostatic band alignment model for 2D material heterojunctions, which relies on the isolated properties of each material.

In Chapter 5, we identify several metallic transition metal dichalcogenide (TMD) candidates as potential 2D material based MTJ electrodes, offering several orders of magnitude greater conductivity than in current graphene based junctions. Based on our first principles calculations, MSe$_2$ (M = Nb, Ta) and 2H-TaS$_2$ electrodes offer between 10^2 to 10^3 greater spin current densities than turbostratic graphene leads for bilayer CrI$_3$ channels. Moreover, TMR values on the order of 100% are achievable by means of increasing the number of CrI$_3$ layers within the channel or choosing low/high WF TMDs which produce Fermi level alignments close to the band edges of CrI$_3$. We also find that TMDs such as 2H-NbSe$_2$ and 2H-TaSe$_2$ couple with the CrI$_3$ channel, inducing MIGS at the interfaces. Lastly, we introduce a technique for both transmission and TMR approximation in CrX_3 (X = Br and I) channels using the complex wavevectors of bulk. This technique serves as a guide for future vdW engineering in 2D based devices.

The newly found ferromagnetic 2D semiconductor CrI$_3$ has opened various avenues in spintronic research and applications such as magnetic tunnel junctions. Although current CrI$_3$ devices are capable of producing substantial magnetoresistance values, they are limited to low temperatures and require strong external fields to operate. Beyond Gr/NL-CrI$_3$ based magnetic tunnel junctions, the search for alternative room temperature magnetic 2D semiconducting junctions is imperative in the design and application of 2D material based spintronic devices. Regarding our research, we offer an underlying blueprint that may be used to characterize alternative and future devices using their isolated or bulk properties such as complex band structures. We find that the complex band structure is a crucial quantity in describing spin transport in thin channels and offers atomistic insights on the underlying physical phenomena, applicable to both magnetic or nonmagnetic insulators. By proposing several TMD electrode candidates

and offering an additional list of potentially viable metallic TMD leads via high-throughput calculations, we hope to facilitate experimental design.

References

[1] J. J. Heath, M. Costa, M. Buongiorno-Nardelli, and M. A. Kuroda, "Role of quantum confinement and interlayer coupling in cri 3-graphene magnetic tunnel junctions," *Physical Review B*, vol. 101, no. 19, p. 195439, 2020. [Online]. Available: https://doi.org/10.1103/PhysRevB.101.195439

[2] M. D. Blanchet, J. J. Heath, T. C. Kaspar, B. E. Matthews, S. R. Spurgeon, M. E. Bowden, S. M. Heald, T. Issacs-Smith, M. A. Kuroda, and R. B. Comes, "Electronic and structural properties of single-crystal jahn–teller active co1+ x mn2- x o4 thin films," *Journal of Physics: Condensed Matter*, vol. 33, no. 12, p. 124002, 2021. [Online]. Available: https://doi.org/10.1088/1361-648X/abd573

[3] B. Hunt, J. D. Sanchez-Yamagishi, A. F. Young, M. Yankowitz, B. J. LeRoy, K. Watanabe, T. Taniguchi, P. Moon, M. Koshino, P. Jarillo-Herrero *et al.*, "Massive dirac fermions and hofstadter butterfly in a van der waals heterostructure," *Science*, vol. 340, no. 6139, pp. 1427–1430, 2013.

[4] J. B. Kuo, W. Lee, and J.-H. Sim, "Back-gate bias effect on the subthreshold behavior and the switching performance in an ultrathin soi cmos inverter operating at 77 and 300 k," *IEEE transactions on electron devices*, vol. 39, no. 12, pp. 2781–2790, 1992.

[5] B. Radisavljevic, A. Radenovic, J. Brivio, V. Giacometti, and A. Kis, "Single-layer mos 2 transistors," *Nature nanotechnology*, vol. 6, no. 3, pp. 147–150, 2011.

[6] S. Yuasa, T. Nagahama, A. Fukushima, Y. Suzuki, and K. Ando, "Giant room-temperature magnetoresistance in single-crystal fe/mgo/fe magnetic tunnel junctions," *Nature materials*, vol. 3, no. 12, pp. 868–871, 2004.

[7] D. R. Klein, D. MacNeill, J. L. Lado, D. Soriano, E. Navarro-Moratalla, K. Watanabe, T. Taniguchi, S. Manni, P. Canfield, J. Fernández-Rossier, and P. Jarillo-Herrero, "Probing magnetism in 2d van der waals crystalline insulators via electron tunneling," *Science*, vol. 360, no. 6394, pp. 1218–1222, 2018.

[8] M. Chakraverty and P. Harisankar, "Demonstration of bias dependence of tunnel magnetoresistance in co-mgo-co magnetic tunnel junctions using first principles calculations," in *2018 4th International Conference on Devices, Circuits and Systems (ICDCS)*. IEEE, 2018, pp. 130–136.

[9] J. W. Moore, W. G. Davies, and R. W. Collins, *Chemisrty*. McGraw-Hill, 1978.

[10] D.-M. Chen, P. M. Shenai, and Y. Zhao, "Tight binding description on the band gap opening of pyrene-dispersed graphene," *Physical Chemistry Chemical Physics*, vol. 13, no. 4, pp. 1515–1520, 2011.

[11] T. Aktor, A.-P. Jauho, and S. R. Power, "Electronic transport in graphene nanoribbons with sublattice-asymmetric doping," *Physical Review B*, vol. 93, no. 3, p. 035446, 2016.

[12] I. Pollini, "Satellite structure in photoelectron spectra of crcl3," *Solid state communications*, vol. 113, no. 10, pp. 559–564, 2000.

[13] M. A. McGuire, H. Dixit, V. R. Cooper, and B. C. Sales, "Coupling of crystal structure and magnetism in the layered, ferromagnetic insulator cri3," *Chem. of Mater.*, vol. 27, no. 2, pp. 612–620, 2015.

[14] M. Marezio, P. Dernier, A. Menth, and G. Hull Jr, "The crystal structure of nbse2 at 15 k," *Journal of Solid State Chemistry*, vol. 4, no. 3, pp. 425–429, 1972.

[15] D. E. Moncton, J. Axe, and F. DiSalvo, "Neutron scattering study of the charge-density wave transitions in 2 h- ta se 2 and 2 h- nb se 2," *Physical Review B*, vol. 16, no. 2, p. 801, 1977.

[16] G. A. Wiegers, J. L. de Boer, A. Meetsma, and S. van Smaalen, "Domain structure and refinement of the triclinic superstructure of 1t-tase2 by single crystal x-ray diffraction," *Zeitschrift für Kristallographie-Crystalline Materials*, vol. 216, no. 1, pp. 45–50, 2001.

[17] A. Meetsma, G. Wiegers, R. Haange, and J. De Boer, "Structure of 2h-tas2," *Acta Crystallographica Section C: Crystal Structure Communications*, vol. 46, no. 9, pp. 1598–1599, 1990.

[18] R. Peierls, "Quelques propriétés typiques des corps solides," in *Annales de l'institut Henri Poincaré*, vol. 5, no. 3, 1935, pp. 177–222.

[19] L. D. Landau, "Zur theorie der phasenumwandlungen ii," *Phys. Z. Sowjetunion*, vol. 11, no. 545, pp. 26–35, 1937.

[20] N. D. Mermin, "Crystalline order in two dimensions," *Physical Review*, vol. 176, no. 1, p. 250, 1968.

[21] K. S. Novoselov, A. K. Geim, S. V. Morozov, D. Jiang, Y. Zhang, S. V. Dubonos, I. V. Grigorieva, and A. A. Firsov, "Electric field effect in atomically thin carbon films," *science*, vol. 306, no. 5696, pp. 666–669, 2004.

[22] K. Watanabe, T. Taniguchi, and H. Kanda, "Direct-bandgap properties and evidence for ultraviolet lasing of hexagonal boron nitride single crystal," *Nature materials*, vol. 3, no. 6, pp. 404–409, 2004.

[23] K. S. Novoselov, A. K. Geim, S. V. Morozov, D. Jiang, M. I. Katsnelson, I. Grigorieva, S. Dubonos, and A. A. Firsov, "Two-dimensional gas of massless dirac fermions in graphene," *nature*, vol. 438, no. 7065, pp. 197–200, 2005.

[24] B. Lalmi, H. Oughaddou, H. Enriquez, A. Kara, S. Vizzini, B. Ealet, and B. Aufray, "Epitaxial growth of a silicene sheet," *Applied Physics Letters*, vol. 97, no. 22, p. 223109, 2010.

[25] A. K. Geim and K. S. Novoselov, "The rise of graphene," in *Nanoscience and technology: a collection of reviews from nature journals*. World Scientific, 2010, pp. 11–19.

[26] N. Mounet, M. Gibertini, P. Schwaller, D. Campi, A. Merkys, A. Marrazzo, T. Sohier, I. E. Castelli, A. Cepellotti, G. Pizzi *et al.*, "Two-dimensional materials from high-throughput computational exfoliation of experimentally known compounds," *Nature nanotechnology*, vol. 13, no. 3, pp. 246–252, 2018.

[27] I. E. Dzyaloshinskii, E. M. Lifshitz, and L. P. Pitaevskii, "The general theory of van der waals forces," *Advances in Physics*, vol. 10, no. 38, pp. 165–209, 1961.

[28] M. Dresselhaus and G. Dresselhaus, "Intercalation compounds of graphite," *Advances in Physics*, vol. 30, no. 2, pp. 139–326, 1981.

[29] I. L. Spain, "Electronic transport-properties of graphite, carbons, and related materials," *Chemistry and physics of carbon*, vol. 16, pp. 119–304, 1981.

[30] C. Lee, X. Wei, J. W. Kysar, and J. Hone, "Measurement of the elastic properties and intrinsic strength of monolayer graphene," *science*, vol. 321, no. 5887, pp. 385–388, 2008.

[31] K. Cao, S. Feng, Y. Han, L. Gao, T. H. Ly, Z. Xu, and Y. Lu, "Elastic straining of free-standing monolayer graphene," *Nature communications*, vol. 11, no. 1, pp. 1–7, 2020.

[32] A. K. Geim and I. V. Grigorieva, "Van der waals heterostructures," *Nature*, vol. 499, no. 7459, pp. 419–425, 2013.

[33] D. Malko, C. Neiss, F. Vines, and A. Görling, "Competition for graphene: graphynes with direction-dependent dirac cones," *Physical review letters*, vol. 108, no. 8, p. 086804, 2012.

[34] P. Vogt, P. De Padova, C. Quaresima, J. Avila, E. Frantzeskakis, M. C. Asensio, A. Resta, B. Ealet, and G. Le Lay, "Silicene: compelling experimental evidence for graphenelike two-dimensional silicon," *Physical review letters*, vol. 108, no. 15, p. 155501, 2012.

[35] M. Dávila, L. Xian, S. Cahangirov, A. Rubio, and G. Le Lay, "Germanene: a novel two-dimensional germanium allotrope akin to graphene and silicene," *New Journal of Physics*, vol. 16, no. 9, p. 095002, 2014.

[36] L. Li, S.-z. Lu, J. Pan, Z. Qin, Y.-q. Wang, Y. Wang, G.-y. Cao, S. Du, and H.-J. Gao, "Buckled germanene formation on pt (111)," *Advanced Materials*, vol. 26, no. 28, pp. 4820–4824, 2014.

[37] H. Liu, A. T. Neal, Z. Zhu, Z. Luo, X. Xu, D. Tománek, and P. D. Ye, "Phosphorene: an unexplored 2d semiconductor with a high hole mobility," *ACS nano*, vol. 8, no. 4, pp. 4033–4041, 2014.

[38] Z. Zhang, Y. Yang, G. Gao, and B. I. Yakobson, "Two-dimensional boron monolayers mediated by metal substrates," *Angewandte Chemie*, vol. 127, no. 44, pp. 13 214–13 218, 2015.

[39] F.-f. Zhu, W.-j. Chen, Y. Xu, C.-l. Gao, D.-d. Guan, C.-h. Liu, D. Qian, S.-C. Zhang, and J.-f. Jia, "Epitaxial growth of two-dimensional stanene," *Nature materials*, vol. 14, no. 10, pp. 1020–1025, 2015.

[40] P. Ares, F. Aguilar-Galindo, D. Rodríguez-San-Miguel, D. A. Aldave, S. Díaz-Tendero, M. Alcamí, F. Martín, J. Gómez-Herrero, and F. Zamora, "Mechanical isolation of highly stable antimonene under ambient conditions," *Advanced Materials*, vol. 28, no. 30, pp. 6332–6336, 2016.

[41] F. Reis, G. Li, L. Dudy, M. Bauernfeind, S. Glass, W. Hanke, R. Thomale, J. Schäfer, and R. Claessen, "Bismuthene on a sic substrate: A candidate for a high-temperature quantum spin hall material," *Science*, vol. 357, no. 6348, pp. 287–290, 2017.

[42] J. Yuhara, B. He, N. Matsunami, M. Nakatake, and G. Le Lay, "Graphene's latest cousin: Plumbene epitaxial growth on a "nano watercube"," *Advanced Materials*, vol. 31, no. 27, p. 1901017, 2019.

[43] A. Rubio, J. L. Corkill, and M. L. Cohen, "Theory of graphitic boron nitride nanotubes," *Physical Review B*, vol. 49, no. 7, p. 5081, 1994.

[44] M. Morscher, M. Corso, T. Greber, and J. Osterwalder, "Formation of single layer h-bn on pd (1 1 1)," *Surface science*, vol. 600, no. 16, pp. 3280–3284, 2006.

[45] Z. Y. Al Balushi, K. Wang, R. K. Ghosh, R. A. Vilá, S. M. Eichfeld, J. D. Caldwell, X. Qin, Y.-C. Lin, P. A. DeSario, G. Stone *et al.*, "Two-dimensional gallium nitride realized via graphene encapsulation," *Nature materials*, vol. 15, no. 11, pp. 1166–1171, 2016.

[46] C. Li, C. Cao, and H. Zhu, "Preparation of graphitic carbon nitride by electrodeposition," *Chinese Science Bulletin*, vol. 48, no. 16, pp. 1737–1740, 2003.

[47] Q. Guo, Y. Xie, X. Wang, S. Lv, T. Hou, and X. Liu, "Characterization of well-crystallized graphitic carbon nitride nanocrystallites via a benzene-thermal route at low temperatures," *Chemical Physics Letters*, vol. 380, no. 1-2, pp. 84–87, 2003.

[48] J. Xu, L. Zhang, R. Shi, and Y. Zhu, "Chemical exfoliation of graphitic carbon nitride for efficient heterogeneous photocatalysis," *Journal of Materials Chemistry A*, vol. 1, no. 46, pp. 14 766–14 772, 2013.

[49] A. N. Andriotis, E. Richter, and M. Menon, "Prediction of a new graphenelike si 2 bn solid," *Physical Review B*, vol. 93, no. 8, p. 081413, 2016.

[50] M. Naguib, M. Kurtoglu, V. Presser, J. Lu, J. Niu, M. Heon, L. Hultman, Y. Gogotsi, and M. W. Barsoum, "Two-dimensional nanocrystals produced by exfoliation of ti3alc2," *Advanced materials*, vol. 23, no. 37, pp. 4248–4253, 2011.

[51] A. Lipatov, M. Alhabeb, M. R. Lukatskaya, A. Boson, Y. Gogotsi, and A. Sinitskii, "Effect of synthesis on quality, electronic properties and environmental stability of individual monolayer ti3c2 mxene flakes," *Advanced Electronic Materials*, vol. 2, no. 12, p. 1600255, 2016.

[52] K. Hantanasirisakul, M. Alhabeb, A. Lipatov, K. Maleski, B. Anasori, P. Salles, C. Ieosakulrat, P. Pakawatpanurut, A. Sinitskii, S. J. May *et al.*, "Effects of synthesis and processing on optoelectronic properties of titanium carbonitride mxene," *Chemistry of Materials*, vol. 31, no. 8, pp. 2941–2951, 2019.

[53] A. Iqbal, F. Shahzad, K. Hantanasirisakul, M.-K. Kim, J. Kwon, J. Hong, H. Kim, D. Kim, Y. Gogotsi, and C. M. Koo, "Anomalous absorption of electromagnetic waves by 2d transition metal carbonitride ti3cntx (mxene)," *Science*, vol. 369, no. 6502, pp. 446–450, 2020.

[54] Y. Gogotsi and B. Anasori, "The rise of mxenes," 2019.

[55] P. Joensen, R. Frindt, and S. R. Morrison, "Single-layer mos2," *Materials research bulletin*, vol. 21, no. 4, pp. 457–461, 1986.

[56] D. Yang and R. Frindt, "Li-intercalation and exfoliation of ws2," *Journal of Physics and Chemistry of Solids*, vol. 57, no. 6-8, pp. 1113–1116, 1996.

[57] D. J. O'Hara, T. Zhu, A. H. Trout, A. S. Ahmed, Y. K. Luo, C. H. Lee, M. R. Brenner, S. Rajan, J. A. Gupta, D. W. McComb *et al.*, "Room temperature intrinsic ferromagnetism in epitaxial manganese selenide films in the monolayer limit," *Nano letters*, vol. 18, no. 5, pp. 3125–3131, 2018.

[58] Y. Guo, H. Deng, X. Sun, X. Li, J. Zhao, J. Wu, W. Chu, S. Zhang, H. Pan, X. Zheng *et al.*, "Modulation of metal and insulator states in 2d ferromagnetic vs2 by van der waals interaction engineering," *Advanced Materials*, vol. 29, no. 29, p. 1700715, 2017.

[59] M. Bonilla, S. Kolekar, Y. Ma, H. C. Diaz, V. Kalappattil, R. Das, T. Eggers, H. R. Gutierrez, M.-H. Phan, and M. Batzill, "Strong room-temperature ferromagnetism in vse 2 monolayers on van der waals substrates," *Nature nanotechnology*, vol. 13, no. 4, pp. 289–293, 2018.

[60] K. Xu, P. Chen, X. Li, C. Wu, Y. Guo, J. Zhao, X. Wu, and Y. Xie, "Ultrathin nanosheets of vanadium diselenide: a metallic two-dimensional material with ferromagnetic charge-density-wave behavior," *Angewandte Chemie*, vol. 125, no. 40, pp. 10 671–10 675, 2013.

[61] E. Wollan, H. Child, W. Koehler, and M. Wilkinson, "Antiferromagnetic properties of the iron group trifluorides," *Physical Review*, vol. 112, no. 4, p. 1132, 1958.

[62] S. Mattsson and B. Paulus, "Density functional theory calculations of structural, electronic, and magnetic properties of the 3d metal trifluorides mf3 (m= ti-ni) in the solid state," *Journal of computational chemistry*, vol. 40, no. 11, pp. 1190–1197, 2019.

[63] N. D. Mermin and H. Wagner, "Absence of ferromagnetism or antiferromagnetism in one- or two-dimensional isotropic heisenberg models," *Phys. Rev. Lett.*, vol. 17, pp. 1133–1136, 1966.

[64] P. Bruno, "Absence of spontaneous magnetic order at nonzero temperature in one- and two-dimensional heisenberg and XY systems with long-range interactions," *Phys. Rev. Lett.*, vol. 87, p. 137203, 2001.

[65] B. Sachs, T. O. Wehling, K. S. Novoselov, A. I. Lichtenstein, and M. I. Katsnelson, "Ferromagnetic two-dimensional crystals: Single layers of k_2cuf_4," *Phys. Rev. B*, vol. 88, p. 201402, 2013.

[66] X. Li and J. Yang, "Crxte3 (x = si, ge) nanosheets: two dimensional intrinsic ferromagnetic semiconductors," *J. Mater. Chem. C*, vol. 2, pp. 7071–7076, 2014.

[67] Y. Tian, M. J. Gray, H. Ji, R. J. Cava, and K. S. Burch, "Magneto-elastic coupling in a potential ferromagnetic 2d atomic crystal," *2D Mater.*, vol. 3, no. 2, p. 025035, 2016.

[68] J.-U. Lee, S. Lee, J. H. Ryoo, S. Kang, T. Y. Kim, P. Kim, C.-H. Park, J.-G. Park, and H. Cheong, "Ising-type magnetic ordering in atomically thin feps3," *Nano Lett.*, vol. 16, no. 12, pp. 7433–7438, 12 2016.

[69] C. Gong, L. Li, Z. Li, H. Ji, A. Stern, Y. Xia, T. Cao, W. Bao, C. Wang, Y. Wang, Z. Q. Qiu, R. J. Cava, S. G. Louie, J. Xia, and X. Zhang, "Discovery of intrinsic ferromagnetism in two-dimensional van der Waals crystals," *Nature*, vol. 546, no. 7657, pp. 265–269, Jun. 2017.

[70] B. Huang, G. Clark, E. Navarro-Moratalla, D. R. Klein, R. Cheng, K. L. Seyler, D. Zhong, E. Schmidgall, M. A. McGuire, D. H. Cobden, W. Yao, D. Xiao, P. Jarillo-Herrero, and X. Xu, "Layer-dependent ferromagnetism in a van der Waals crystal down to the monolayer limit," *Nature*, vol. 546, no. 7657, pp. 270–273, Jun. 2017.

[71] M. A. McGuire, G. Clark, K. Santosh, W. M. Chance, G. E. Jellison Jr, V. R. Cooper, X. Xu, and B. C. Sales, "Magnetic behavior and spin-lattice coupling in cleavable van der waals layered crcl 3 crystals," *Physical Review Materials*, vol. 1, no. 1, p. 014001, 2017.

[72] M. Abramchuk, S. Jaszewski, K. R. Metz, G. B. Osterhoudt, Y. Wang, K. S. Burch, and F. Tafti, "Controlling magnetic and optical properties of the van der waals crystal crcl3-xbrx via mixed halide chemistry," *Advanced Materials*, vol. 30, no. 25, p. 1801325, 2018.

[73] Z. Zhang, J. Shang, C. Jiang, A. Rasmita, W. Gao, and T. Yu, "Direct photoluminescence probing of ferromagnetism in monolayer two-dimensional crbr3," *Nano Letters*, vol. 19, no. 5, pp. 3138–3142, 2019.

[74] W. Chen, Z. Sun, Z. Wang, L. Gu, X. Xu, S. Wu, and C. Gao, "Direct observation of van der waals stacking–dependent interlayer magnetism," *Science*, vol. 366, no. 6468, pp. 983–987, 2019.

[75] J. He, S. Ma, P. Lyu, and P. Nachtigall, "Unusual dirac half-metallicity with intrinsic ferromagnetism in vanadium trihalide monolayers," *Journal of Materials Chemistry C*, vol. 4, no. 13, pp. 2518–2526, 2016.

[76] D. Sheberla, L. Sun, M. A. Blood-Forsythe, S. Er, C. R. Wade, C. K. Brozek, A. Aspuru-Guzik, and M. Dincă, "High electrical conductivity in ni3 (2, 3, 6, 7, 10, 11-hexaiminotriphenylene) 2, a semiconducting metal–organic graphene analogue," *Journal of the American Chemical Society*, vol. 136, no. 25, pp. 8859–8862, 2014.

[77] S. Chen, J. Dai, and X. C. Zeng, "Metal–organic kagome lattices m 3 (2, 3, 6, 7, 10, 11-hexaiminotriphenylene) 2 (m= ni and cu): from semiconducting to metallic by metal substitution," *Physical Chemistry Chemical Physics*, vol. 17, no. 8, pp. 5954–5958, 2015.

[78] M. G. Campbell, D. Sheberla, S. F. Liu, T. M. Swager, and M. Dincă, "Cu3 (hexaiminotriphenylene) 2: an electrically conductive 2d metal–organic framework for chemiresistive sensing," *Angewandte Chemie International Edition*, vol. 54, no. 14, pp. 4349–4352, 2015.

[79] V. O. Özçelik and S. Ciraci, "Size dependence in the stabilities and electronic properties of α-graphyne and its boron nitride analogue," *The Journal of Physical Chemistry C*, vol. 117, no. 5, pp. 2175–2182, 2013.

[80] G. Li, Y. Li, H. Liu, Y. Guo, Y. Li, and D. Zhu, "Architecture of graphdiyne nanoscale films," *Chemical Communications*, vol. 46, no. 19, pp. 3256–3258, 2010.

[81] K. Novoselov, o. A. Mishchenko, o. A. Carvalho, and A. C. Neto, "2d materials and van der waals heterostructures," *Science*, vol. 353, no. 6298, 2016.

[82] M. Yankowitz, J. Xue, D. Cormode, J. D. Sanchez-Yamagishi, K. Watanabe, T. Taniguchi, P. Jarillo-Herrero, P. Jacquod, and B. J. LeRoy, "Emergence of superlattice dirac points in graphene on hexagonal boron nitride," *Nature physics*, vol. 8, no. 5, pp. 382–386, 2012.

[83] W. Yang, G. Chen, Z. Shi, C.-C. Liu, L. Zhang, G. Xie, M. Cheng, D. Wang, R. Yang, D. Shi *et al.*, "Epitaxial growth of single-domain graphene on hexagonal boron nitride," *Nature materials*, vol. 12, no. 9, pp. 792–797, 2013.

[84] P. Zomer, S. Dash, N. Tombros, and B. Van Wees, "A transfer technique for high mobility graphene devices on commercially available hexagonal boron nitride," *Applied Physics Letters*, vol. 99, no. 23, p. 232104, 2011.

[85] K. Khan, A. K. Tareen, M. Aslam, R. Wang, Y. Zhang, A. Mahmood, Z. Ouyang, H. Zhang, and Z. Guo, "Recent developments in emerging two-dimensional materials

and their applications," *Journal of Materials Chemistry C*, vol. 8, no. 2, pp. 387–440, 2020.

[86] H. J. Yoon, J. H. Yang, Z. Zhou, S. S. Yang, M. M.-C. Cheng *et al.*, "Carbon dioxide gas sensor using a graphene sheet," *Sensors and Actuators B: Chemical*, vol. 157, no. 1, pp. 310–313, 2011.

[87] N. R. Glavin, R. Rao, V. Varshney, E. Bianco, A. Apte, A. Roy, E. Ringe, and P. M. Ajayan, "Emerging applications of elemental 2d materials," *Advanced Materials*, vol. 32, no. 7, p. 1904302, 2020.

[88] S. P. Surwade, S. N. Smirnov, I. V. Vlassiouk, R. R. Unocic, G. M. Veith, S. Dai, and S. M. Mahurin, "Water desalination using nanoporous single-layer graphene," *Nature nanotechnology*, vol. 10, no. 5, pp. 459–464, 2015.

[89] T. H. Han, Y.-K. Huang, A. T. Tan, V. P. Dravid, and J. Huang, "Steam etched porous graphene oxide network for chemical sensing," *Journal of the American Chemical Society*, vol. 133, no. 39, pp. 15 264–15 267, 2011.

[90] J. Xiao, D. Mei, X. Li, W. Xu, D. Wang, G. L. Graff, W. D. Bennett, Z. Nie, L. V. Saraf, I. A. Aksay *et al.*, "Hierarchically porous graphene as a lithium–air battery electrode," *Nano letters*, vol. 11, no. 11, pp. 5071–5078, 2011.

[91] D. Datta, J. Li, and V. B. Shenoy, "Defective graphene as a high-capacity anode material for na-and ca-ion batteries," *ACS applied materials & interfaces*, vol. 6, no. 3, pp. 1788–1795, 2014.

[92] J. J. Heath and M. A. Kuroda, "First principles studies of the interactions between alkali metal elements and oxygen-passivated nanopores in graphene," *Physical Chemistry Chemical Physics*, vol. 20, no. 40, pp. 25 822–25 828, 2018. [Online]. Available: https://doi.org/10.1039/C8CP04958K

[93] C. H. Wann, K. Noda, T. Tanaka, M. Yoshida, and C. Hu, "A comparative study of advanced mosfet concepts," *IEEE Transactions on Electron Devices*, vol. 43, no. 10, pp. 1742–1753, 1996.

[94] F. Xia, D. B. Farmer, Y.-m. Lin, and P. Avouris, "Graphene field-effect transistors with high on/off current ratio and large transport band gap at room temperature," *Nano letters*, vol. 10, no. 2, pp. 715–718, 2010.

[95] C. Zhou, X. Wang, S. Raju, Z. Lin, D. Villaroman, B. Huang, H. L.-W. Chan, M. Chan, and Y. Chai, "Low voltage and high on/off ratio field-effect transistors based on cvd mos 2 and ultra high-k gate dielectric pzt," *Nanoscale*, vol. 7, no. 19, pp. 8695–8700, 2015.

[96] X. Liu, D. Qu, J. Ryu, F. Ahmed, Z. Yang, D. Lee, and W. J. Yoo, "P-type polar transition of chemically doped multilayer mos2 transistor," *Advanced Materials*, vol. 28, no. 12, pp. 2345–2351, 2016.

[97] P. Bolshakov, P. Zhao, A. Azcatl, P. K. Hurley, R. M. Wallace, and C. D. Young, "Improvement in top-gate mos2 transistor performance due to high quality backside al2o3 layer," *Applied Physics Letters*, vol. 111, no. 3, p. 032110, 2017.

[98] C. Liu, R. A. Khadar, and E. Matioli, "Vertical gan-on-si mosfets with monolithically integrated freewheeling schottky barrier diodes," *IEEE Electron Device Letters*, vol. 39, no. 7, pp. 1034–1037, 2018.

[99] M. H. Wong, K. Goto, H. Murakami, Y. Kumagai, and M. Higashiwaki, "Current aperture vertical beta-ga 2 o 3 mosfets fabricated by n-and si-ion implantation doping," *IEEE Electron Device Letters*, vol. 40, no. 3, pp. 431–434, 2018.

[100] A. Nourbakhsh, A. Zubair, R. N. Sajjad, A. Tavakkoli KG, W. Chen, S. Fang, X. Ling, J. Kong, M. S. Dresselhaus, E. Kaxiras *et al.*, "Mos2 field-effect transistor with sub-10 nm channel length," *Nano letters*, vol. 16, no. 12, pp. 7798–7806, 2016.

[101] C. Klinkert, Á. Szabó, C. Stieger, D. Campi, N. Marzari, and M. Luisier, "2-d materials for ultra-scaled field-effect transistors: hundred candidates under the ab initio microscope," *ACS Nano*, 2020.

[102] Z. Diao, D. Apalkov, M. Pakala, Y. Ding, A. Panchula, and Y. Huai, "Spin transfer switching and spin polarization in magnetic tunnel junctions with mgo and alo x barriers," *Applied Physics Letters*, vol. 87, no. 23, p. 232502, 2005.

[103] S. Tehrani, B. Engel, J. Slaughter, E. Chen, M. DeHerrera, M. Durlam, P. Naji, R. Whig, J. Janesky, and J. Calder, "Recent developments in magnetic tunnel junction mram," *IEEE Transactions on magnetics*, vol. 36, no. 5, pp. 2752–2757, 2000.

[104] S. S. Parkin, C. Kaiser, A. Panchula, P. M. Rice, B. Hughes, M. Samant, and S.-H. Yang, "Giant tunnelling magnetoresistance at room temperature with mgo (100) tunnel barriers," *Nature materials*, vol. 3, no. 12, pp. 862–867, 2004.

[105] S. Ikeda, K. Miura, H. Yamamoto, K. Mizunuma, H. Gan, M. Endo, S. Kanai, J. Hayakawa, F. Matsukura, and H. Ohno, "A perpendicular-anisotropy cofeb–mgo magnetic tunnel junction," *Nature materials*, vol. 9, no. 9, pp. 721–724, 2010.

[106] S. Ikeda, J. Hayakawa, Y. Ashizawa, Y. Lee, K. Miura, H. Hasegawa, M. Tsunoda, F. Matsukura, and H. Ohno, "Tunnel magnetoresistance of 604% at 300 k by suppression of ta diffusion in co fe b/ mg o/ co fe b pseudo-spin-valves annealed at high temperature," *Applied Physics Letters*, vol. 93, no. 8, p. 082508, 2008.

[107] T. Song, X. Cai, M. W.-Y. Tu, X. Zhang, B. Huang, N. P. Wilson, K. L. Seyler, L. Zhu, T. Taniguchi, K. Watanabe, M. A. McGuire, D. H. Cobden, D. Xiao, W. Yao, and X. Xu, "Giant tunneling magnetoresistance in spin-filter van der Waals heterostructures," *Science*, vol. 360, no. 6394, pp. 1214–1218, 2018.

[108] H. H. Kim, B. Yang, S. Tian, C. Li, G.-X. Miao, H. Lei, and A. W. Tsen, "Tailored tunnel magnetoresistance response in three ultrathin chromium trihalides," *Nano letters*, vol. 19, no. 8, pp. 5739–5745, 2019.

[109] H. Liu, A. T. Neal, and P. D. Ye, "Channel length scaling of mos2 mosfets," *ACS nano*, vol. 6, no. 10, pp. 8563–8569, 2012.

[110] Y. Zhao, L. Lin, Q. Zhou, Y. Li, S. Yuan, Q. Chen, S. Dong, and J. Wang, "Surface vacancy-induced switchable electric polarization and enhanced ferromagnetism in monolayer metal trihalides," *Nano letters*, vol. 18, no. 5, pp. 2943–2949, 2018.

[111] M. Pizzochero, "Atomic-scale defects in the two-dimensional ferromagnet cri3 from first principles," *Journal of Physics D: Applied Physics*, vol. 53, no. 24, p. 244003, 2020.

[112] R. Wang, Y. Su, G. Yang, J. Zhang, and S. Zhang, "Bipolar doping by intrinsic defects and magnetic phase instability in monolayer cri3," *Chemistry of Materials*, vol. 32, no. 4, pp. 1545–1552, 2020.

[113] S. Hegde, E. Lerner, and J. Daunt, "Thermal and electrical conductivities of exfoliated graphite at low temperatures," *Cryogenics*, vol. 13, no. 4, pp. 230–231, 1973.

[114] H. Pierson, "Handbook of carbon, graphite, diamond, and fullerenes: Properties, processing and applications, noyes, park ridge," 1993.

[115] Z.-M. Liao, H.-C. Wu, S. Kumar, G. S. Duesberg, Y.-B. Zhou, G. L. Cross, I. V. Shvets, and D.-P. Yu, "Large magnetoresistance in few layer graphene stacks with current perpendicular to plane geometry," *Advanced Materials*, vol. 24, no. 14, pp. 1862–1866, 2012.

[116] G. Taylor, A. Isin, and R. Coleman, "Resistivity of iron as a function of temperature and magnetization," *Physical Review*, vol. 165, no. 2, p. 621, 1968.

[117] R. A. Serway, "Principles of physics . fort worth, texas; london: Saunders college pub," ISBN 0-03-020457-7, Tech. Rep., 1998.

[118] S. Meyer, R. Howard, G. Stewart, J. V. Acrivos, and T. Geballe, "Properties of intercalated 2h-nbse2, 4hb-tas2, and 1t-tas2," *The Journal of Chemical Physics*, vol. 62, no. 11, pp. 4411–4419, 1975.

[119] C. Zhang, J. Tan, Y. Pan, X. Cai, X. Zou, H.-M. Cheng, and B. Liu, "Mass production of 2d materials by intermediate-assisted grinding exfoliation," *National Science Review*, vol. 7, no. 2, pp. 324–332, 2020.

[120] L. Yang, W. Chen, Q. Yu, and B. Liu, "Mass production of two-dimensional materials beyond graphene and their applications," *Nano Research*, pp. 1–15, 2020.

[121] R. Mas-Balleste, C. Gomez-Navarro, J. Gomez-Herrero, and F. Zamora, "2d materials: to graphene and beyond," *Nanoscale*, vol. 3, no. 1, pp. 20–30, 2011.

[122] J. C. Slater, *Quantum Theory of Molecules and Solids. Vol. 1: Electronic Structure of Molecules*. McGraw-Hill, 1963.

[123] J. Singleton, *Band theory and electronic properties of solids*. Oxford University Press, 2001, vol. 2.

[124] A. Bravais, "Les systemes formes par des pointes distribues regulierement sur un plan ou dans l'espace," *J. Ecole. Polytech.*, pp. 1–128, 1850.

[125] M. Born and T. Von Karman, "Theory of specific heat," *Phys. Z*, vol. 14, p. 15, 1913.

[126] F. Bloch, "Quantum mechanics of electrons in crystal lattices," *Z. Phys*, vol. 52, pp. 555–600, 1928.

[127] L. Brillouin, "Les électrons dans les métaux et le classement des ondes de de broglie correspondantes," *Comptes Rendus Hebdomadaires des Séances de l'Académie des Sciences*, vol. 191, p. 292, 1930.

[128] E. Goodwin, "Electronic states at the surfaces of crystals: I. the approximation of nearly free electrons," in *Mathematical Proceedings of the Cambridge Philosophical Society*, vol. 35, no. 2. Cambridge University Press, 1939, pp. 205–220.

[129] E. O. Kane, "Theory of tunneling," *Journal of applied Physics*, vol. 32, no. 1, pp. 83–91, 1961.

[130] D. R. Hartree, "The wave mechanics of an atom with a non-coulomb central field. part i. theory and methods," in *Mathematical Proceedings of the Cambridge Philosophical Society*, vol. 24, no. 1. Cambridge University Press, 1928, pp. 89–110.

[131] J. C. Slater, "The self consistent field and the structure of atoms," *Physical Review*, vol. 32, no. 3, p. 339, 1928.

[132] J. Gaunt, "A theory of hartree's atomic fields," in *Mathematical Proceedings of the Cambridge Philosophical Society*, vol. 24, no. 2. Cambridge University Press, 1928, pp. 328–342.

[133] J. C. Slater, "Note on hartree's method," *Physical Review*, vol. 35, no. 2, p. 210, 1930.

[134] V. Fock, "Selfconsistent field mit austausch für natrium," *Zeitschrift für Physik*, vol. 62, no. 11-12, pp. 795–805, 1930.

[135] D. R. Hartree and W. Hartree, "Self-consistent field, with exchange, for beryllium," *Proceedings of the Royal Society of London. Series A-Mathematical and Physical Sciences*, vol. 150, no. 869, pp. 9–33, 1935.

[136] L. H. Thomas, "The calculation of atomic fields," in *Mathematical Proceedings of the Cambridge Philosophical Society*, vol. 23, no. 5. Cambridge University Press, 1927, pp. 542–548.

[137] E. Fermi, "Statistical method to determine some properties of atoms," *Rend. Accad. Naz. Lincei*, vol. 6, no. 602-607, p. 5, 1927.

[138] P. Hohenberg and W. Kohn, "Inhomogeneous electron gas," *Physical review*, vol. 136, no. 3B, p. B864, 1964.

[139] L. Sham and W. Kohn, "One-particle properties of an inhomogeneous interacting electron gas," *Physical Review*, vol. 145, no. 2, p. 561, 1966.

[140] W. Kohn and L. J. Sham, "Self-consistent equations including exchange and correlation effects," *Physical review*, vol. 140, no. 4A, p. A1133, 1965.

[141] P. A. Dirac, "Note on exchange phenomena in the thomas atom," in *Mathematical Proceedings of the Cambridge Philosophical Society*, vol. 26, no. 3. Cambridge University Press, 1930, pp. 376–385.

[142] E. Wigner, "On the interaction of electrons in metals," *Physical Review*, vol. 46, no. 11, p. 1002, 1934.

[143] M. Gell-Mann and K. A. Brueckner, "Correlation energy of an electron gas at high density," *Physical Review*, vol. 106, no. 2, p. 364, 1957.

[144] D. M. Ceperley and B. J. Alder, "Ground state of the electron gas by a stochastic method," *Physical review letters*, vol. 45, no. 7, p. 566, 1980.

[145] S. H. Vosko, L. Wilk, and M. Nusair, "Accurate spin-dependent electron liquid correlation energies for local spin density calculations: a critical analysis," *Canadian Journal of physics*, vol. 58, no. 8, pp. 1200–1211, 1980.

[146] J. P. Perdew and A. Zunger, "Self-interaction correction to density-functional approximations for many-electron systems," *Physical Review B*, vol. 23, no. 10, p. 5048, 1981.

[147] L. A. Cole and J. Perdew, "Calculated electron affinities of the elements," *Physical Review A*, vol. 25, no. 3, p. 1265, 1982.

[148] J. P. Perdew and Y. Wang, "Accurate and simple analytic representation of the electron-gas correlation energy," *Physical review B*, vol. 45, no. 23, p. 13244, 1992.

[149] J. P. Perdew, J. A. Chevary, S. H. Vosko, K. A. Jackson, M. R. Pederson, D. J. Singh, and C. Fiolhais, "Atoms, molecules, solids, and surfaces: Applications of the generalized gradient approximation for exchange and correlation," *Physical review B*, vol. 46, no. 11, p. 6671, 1992.

[150] A. D. Becke, "Density-functional exchange-energy approximation with correct asymptotic behavior," *Physical review A*, vol. 38, no. 6, p. 3098, 1988.

[151] C. Lee, W. Yang, and R. G. Parr, "Development of the colle-salvetti correlation-energy formula into a functional of the electron density," *Physical review B*, vol. 37, no. 2, p. 785, 1988.

[152] Y. Wang and J. P. Perdew, "Correlation hole of the spin-polarized electron gas, with exact small-wave-vector and high-density scaling," *Physical Review B*, vol. 44, no. 24, p. 13298, 1991.

[153] J. P. Perdew, K. Burke, and M. Ernzerhof, "Phys rev lett 77: 3865," *Errata:(1997) Phys Rev Lett*, vol. 78, p. 1396, 1996.

[154] L. A. Agapito, S. Curtarolo, and M. B. Nardelli, "Reformulation of dft+ u as a pseudo-hybrid hubbard density functional for accelerated materials discovery," *Physical Review X*, vol. 5, no. 1, p. 011006, 2015.

[155] J. Heyd, G. E. Scuseria, and M. Ernzerhof, "Hybrid functionals based on a screened coulomb potential," *The Journal of chemical physics*, vol. 118, no. 18, pp. 8207–8215, 2003.

[156] A. D. Becke, "A new mixing of hartree–fock and local density-functional theories," *The Journal of chemical physics*, vol. 98, no. 2, pp. 1372–1377, 1993.

[157] P. Drude, "Zur elektronentheorie der metalle," *Annalen der physik*, vol. 306, no. 3, pp. 566–613, 1900.

[158] A. Sommerfeld, "An electronic theory of the metals based on fermi's statistics," *Z. Phys*, vol. 47, no. 1, p. 1, 1928.

[159] E. Schöll, *Theory of transport properties of semiconductor nanostructures*. Springer Science & Business Media, 2013, vol. 4.

[160] R. Landauer, "Spatial variation of currents and fields due to localized scatterers in metallic conduction," *IBM Journal of research and development*, vol. 1, no. 3, pp. 223–231, 1957.

[161] M. Büttiker, "Four-terminal phase-coherent conductance," *Physical review letters*, vol. 57, no. 14, p. 1761, 1986.

[162] C. Caroli, R. Combescot, P. Nozieres, and D. Saint-James, "Direct calculation of the tunneling current," *Journal of Physics C: Solid State Physics*, vol. 4, no. 8, p. 916, 1971.

[163] J.-H. Jiang and J.-S. Wang, "Caroli formalism in near-field heat transfer between parallel graphene sheets," *Physical Review B*, vol. 96, no. 15, p. 155437, 2017.

[164] Y. Meir and N. S. Wingreen, "Landauer formula for the current through an interacting electron region," *Physical review letters*, vol. 68, no. 16, p. 2512, 1992.

[165] A. Di Carlo, P. Vogl, and W. Pötz, "Theory of zener tunneling and wannier-stark states in semiconductors," *Physical Review B*, vol. 50, no. 12, p. 8358, 1994.

[166] S. Datta, *Electronic Transport in Mesoscopic Systems*, ser. Cambridge Studies in Semiconductor Physics and Microelectronic Engineering. Cambridge: Cambridge University Press, 1995.

[167] A. Di Carlo, P. Vogl, and W. Pötz, "Theory of zener tunneling and wannier-stark states in semiconductors," *Phys. Rev. B*, vol. 50, pp. 8358–8377, 1994.

[168] M. A. Kuroda, J. Tersoff, D. M. Newns, and G. J. Martyna, "Conductance through multilayer graphene films," *Nano Lett.*, vol. 11, no. 9, pp. 3629–3633, 2011.

[169] H. Joon Choi and J. Ihm, "Ab initio pseudopotential method for the calculation of conductance in quantum wires," *Phys. Rev. B*, vol. 59, pp. 2267–2275, Jan 1999.

[170] A. Smogunov, A. Dal Corso, and E. Tosatti, "Ballistic conductance of magnetic co and ni nanowires with ultrasoft pseudopotentials," *Phys. Rev. B*, vol. 70, p. 045417, Jul 2004.

[171] P. Giannozzi, S. Baroni, N. Bonini, M. Calandra, R. Car, C. Cavazzoni, D. Ceresoli, G. L. Chiarotti, M. Cococcioni, I. Dabo, A. D. Corso, S. de Gironcoli, S. Fabris, G. Fratesi, R. Gebauer, U. Gerstmann, C. Gougoussis, A. Kokalj, M. Lazzeri, L. Martin-Samos, N. Marzari, F. Mauri, R. Mazzarello, S. Paolini, A. Pasquarello, L. Paulatto, C. Sbraccia,

S. Scandolo, G. Sclauzero, A. P. Seitsonen, A. Smogunov, P. Umari, and R. M. Wentzcovitch, "Quantum espresso: a modular and open-source software project for quantum simulations of materials," *J. Phys. Condens. Matter*, vol. 21, no. 39, p. 395502, 2009.

[172] P. Giannozzi, O. Andreussi, T. Brumme, O. Bunau, M. Buongiorno Nardelli, M. Calandra, R. Car, C. Cavazzoni, D. Ceresoli, M. Cococcioni, N. Colonna, I. Carnimeo, A. Dal Corso, S. de Gironcoli, P. Delugas, R. A. DiStasio Jr., A. Ferretti, A. Floris, G. Fratesi, G. Fugallo, R. Gebauer, U. Gerstmann, F. Giustino, T. Gorni, J. Jia, M. Kawamura, H.-Y. Ko, A. Kokalj, E. Kucukbenli, M. Lazzeri, M. Marsili, N. Marzari, F. Mauri, N. L. Nguyen, H.-V. Nguyen, A. Otero-de-la Roza, L. Paulatto, S. Ponce', D. Rocca, R. Sabatini, B. Santra, M. Schlipf, A. P. Seitsonen, A. Smogunov, I. Timrov, T. Thonhauser, P. Umari, N. Vast, X. Wu, and S. Baroni, "Advanced capabilities for materials modelling with quantum espresso," *Journal of Physics: Condensed Matter*, vol. 29, no. 46, p. 465901, 2017.

[173] J. P. Perdew, K. Burke, and M. Ernzerhof, "Generalized gradient approximation made simple [phys. rev. lett. 77, 3865 (1996)]," *Phys. Rev. Lett.*, vol. 78, pp. 1396–1396, Feb 1997.

[174] M. Dion, H. Rydberg, E. Schröder, D. C. Langreth, and B. I. Lundqvist, "Van der waals density functional for general geometries," *Phys. Rev. Lett.*, vol. 92, p. 246401, Jun 2004.

[175] T. Thonhauser, V. R. Cooper, S. Li, A. Puzder, P. Hyldgaard, and D. C. Langreth, "Van der waals density functional: Self-consistent potential and the nature of the van der waals bond," *Phys. Rev. B*, vol. 76, no. 12, pp. 125 112–, 09 2007.

[176] V. R. Cooper, "Van der waals density functional: An appropriate exchange functional," *Phys. Rev. B*, vol. 81, p. 161104, Apr 2010.

[177] P. E. Blöchl, "Projector augmented-wave method," *Phys. Rev. B*, vol. 50, pp. 17 953–17 979, Dec 1994.

[178] A. D. Corso, "Pseudopotentials periodic table: From h to pu," *Comput. Mater. Sci.*, vol. 95, pp. 337 – 350, 2014.

[179] L. Wang, I. Meric, P. Huang, Q. Gao, Y. Gao, H. Tran, T. Taniguchi, K. Watanabe, L. Campos, D. Muller *et al.*, "One-dimensional electrical contact to a two-dimensional material," *Science*, vol. 342, no. 6158, pp. 614–617, 2013.

[180] S. Latil and L. Henrard, "Charge carriers in few-layer graphene films," *Phys. Rev. Lett.*, vol. 97, no. 3, p. 036803, 2006.

[181] A. Splendiani, L. Sun, Y. Zhang, T. Li, J. Kim, C.-Y. Chim, G. Galli, and F. Wang, "Emerging photoluminescence in monolayer mos2," *Nano Lett.*, vol. 10, no. 4, pp. 1271–1275, 2010.

[182] T. R. Paudel and E. Y. Tsymbal, "Spin filtering in cri3 tunnel junctions," *ACS applied materials & interfaces*, vol. 11, no. 17, pp. 15 781–15 787, 2019. [Online]. Available: https://doi.org/10.1021/acsami.9b01942

[183] W. Butler, X.-G. Zhang, T. Schulthess, and J. MacLaren, "Spin-dependent tunneling conductance of fe— mgo— fe sandwiches," *Phys. Rev. B*, vol. 63, no. 5, p. 054416, 2001.

[184] V. Karpan, G. Giovannetti, P. Khomyakov, M. Talanana, A. Starikov, M. Zwierzycki, J. Van Den Brink, G. Brocks, and P. J. Kelly, "Graphite and graphene as perfect spin filters," *Phys. Rev. Lett.*, vol. 99, no. 17, p. 176602, 2007.

[185] S. Latil, V. Meunier, and L. Henrard, "Massless fermions in multilayer graphitic systems with misoriented layers: Ab initio calculations and experimental fingerprints," *Phys. Rev. B*, vol. 76, no. 20, p. 201402, 2007.

[186] S. Shallcross, S. Sharma, E. Kandelaki, and O. Pankratov, "Electronic structure of turbostratic graphene," *Physical Review B*, vol. 81, no. 16, p. 165105, 2010.

[187] K. Kim, A. DaSilva, S. Huang, B. Fallahazad, S. Larentis, T. Taniguchi, K. Watanabe, B. J. LeRoy, A. H. MacDonald, and E. Tutuc, "Tunable moiré bands and strong correlations in small-twist-angle bilayer graphene," *Proceedings of the National Academy of Sciences*, vol. 114, no. 13, pp. 3364–3369, 2017.

[188] W. Bao, L. Jing, J. Velasco Jr, Y. Lee, G. Liu, D. Tran, B. Standley, M. Aykol, S. Cronin, D. Smirnov *et al.*, "Stacking-dependent band gap and quantum transport in trilayer graphene," *Nature Physics*, vol. 7, no. 12, p. 948, 2011.

[189] H. J. Monkhorst and J. D. Pack, "Special points for brillouin-zone integrations," *Phys. Rev. B*, vol. 13, no. 12, pp. 5188–5192, 1976.

[190] M. Methfessel and A. Paxton, "High-precision sampling for brillouin-zone integration in metals," *Physical Review B*, vol. 40, no. 6, p. 3616, 1989.

[191] M. Buongiorno Nardelli, "Electronic transport in extended systems: Application to carbon nanotubes," *Phys. Rev. B*, vol. 60, pp. 7828–7833, Sep 1999.

[192] M. Buongiorno Nardelli, F. T. Cerasoli, M. Costa, S. Curtarolo, R. De Gennaro, M. Fornari, L. Liyanage, A. R. Supka, and H. Wang, "Paoflow: A utility to construct and operate on ab initio hamiltonians from the projections of electronic wavefunctions on atomic orbital bases, including characterization of topological materials," *Comput. Mater. Sci.*, vol. 143, pp. 462–472, 2018.

[193] J. Zhang, B. Zhao, T. Zhou, Y. Xue, C. Ma, and Z. Yang, "Strong magnetization and chern insulators in compressed graphene/cri 3 van der waals heterostructures," *Physical Review B*, vol. 97, no. 8, p. 085401, 2018.

[194] D. Sanchez-Portal, E. Artacho, and J. M. Soler, "Projection of plane-wave calculations into atomic orbitals," *Solid State Communications*, vol. 95, no. 10, pp. 685–690, 1995.

[195] X. Qian, J. Li, L. Qi, C.-Z. Wang, T.-L. Chan, Y.-X. Yao, K.-M. Ho, and S. Yip, "Quasi-atomic orbitals for ab initio tight-binding analysis," *Physical Review B*, vol. 78, no. 24, p. 245112, 2008.

[196] P. Li, C. Wang, J. Zhang, S. Chen, D. Guo, W. Ji, and D. Zhong, "Single-layer cri3 grown by molecular beam epitaxy," *Science Bulletin*, 2020. [Online]. Available: https://doi.org/10.1016/j.scib.2020.03.031

[197] P. Jiang, C. Wang, D. Chen, Z. Zhong, Z. Yuan, Z.-Y. Lu, and W. Ji, "Stacking tunable interlayer magnetism in bilayer cri 3," *Physical Review B*, vol. 99, no. 14, p. 144401, 2019.

[198] D. Soriano, C. Cardoso, and J. Fernández-Rossier, "Interplay between interlayer exchange and stacking in cri3 bilayers," *Solid State Communications*, vol. 299, p. 113662, 2019.

[199] S. W. Jang, M. Y. Jeong, H. Yoon, S. Ryee, and M. J. Han, "Microscopic understanding of magnetic interactions in bilayer cri 3," *Physical Review Materials*, vol. 3, no. 3, p. 031001, 2019. [Online]. Available: https://doi.org/10.1103/PhysRevMaterials.3.031001

[200] K. L. Seyler, D. Zhong, D. R. Klein, S. Gao, X. Zhang, B. Huang, E. Navarro-Moratalla, L. Yang, D. H. Cobden, M. A. McGuire *et al.*, "Ligand-field helical luminescence in a 2d ferromagnetic insulator," *Nature Physics*, vol. 14, no. 3, p. 277, 2018.

[201] Z. Wu, J. Yu, and S. Yuan, "Strain-tunable magnetic and electronic properties of monolayer cri 3," *Physical Chemistry Chemical Physics*, vol. 21, no. 15, pp. 7750–7755, 2019.

[202] J. L. Lado and J. Fernández-Rossier, "On the origin of magnetic anisotropy in two dimensional cri3," *2D Materials*, vol. 4, no. 3, p. 035002, 2017.

[203] Z. Wang, I. Gutiérrez-Lezama, N. Ubrig, M. Kroner, M. Gibertini, T. Taniguchi, K. Watanabe, A. Imamoğlu, E. Giannini, and A. F. Morpurgo, "Very large tunneling magnetoresistance in layered magnetic semiconductor cri 3," *Nat. Commun.*, vol. 9, no. 1, p. 2516, 2018.

[204] M. Wu, Z. Li, T. Cao, and S. G. Louie, "Physical origin of giant excitonic and magneto-optical responses in two-dimensional ferromagnetic insulators," *Nature communications*, vol. 10, no. 1, p. 2371, 2019.

[205] A. Castellanos-Gomez, L. Vicarelli, E. Prada, J. O. Island, K. L. Narasimha-Acharya, S. I. Blanter, D. J. Groenendijk, M. Buscema, G. A. Steele, J. V. Alvarez, H. W. Zandbergen, J. J. Palacios, and H. S. J. van der Zant, "Isolation and characterization of few-layer black phosphorus," *2D Mater.*, vol. 1, no. 2, p. 025001, jun 2014.

[206] E. U. Condon, "Tunneling—how it all started," *Am. J. Phys.*, vol. 46, no. 4, pp. 319–323, 1978.

[207] S. M. Sze, *Physics of Semiconductor Devices*, ser. Wiley-Interscience publication. New York: John Wiley & Sons, 1981.

[208] F. A. Padovani and R. Stratton, "Field and thermionic-field emission in Schottky barriers," *Solid State Electron.*, vol. 9, pp. 695–707, Jul. 1966.

[209] T. Song, M. W.-Y. Tu, C. Carnahan, X. Cai, T. Taniguchi, K. Watanabe, M. A. McGuire, D. H. Cobden, D. Xiao, W. Yao, and X. Xu, "Voltage Control of a van der Waals Spin-Filter Magnetic Tunnel Junction," *Nano Lett.*, vol. 19, no. 2, pp. 915–920, Feb. 2019.

[210] C. Enderlein, Y. Kim, A. Bostwick, E. Rotenberg, and K. Horn, "The formation of an energy gap in graphene on ruthenium by controlling the interface," *New Journal of Physics*, vol. 12, no. 3, p. 033014, 2010.

[211] A. Fedorov, N. Verbitskiy, D. Haberer, C. Struzzi, L. Petaccia, D. Usachov, O. Vilkov, D. Vyalikh, J. Fink, M. Knupfer *et al.*, "Observation of a universal donor-dependent vibrational mode in graphene," *Nature communications*, vol. 5, p. 3257, 2014.

[212] D. Pierucci, H. Henck, J. Avila, A. Balan, C. H. Naylor, G. Patriarche, Y. J. Dappe, M. G. Silly, F. Sirotti, A. C. Johnson *et al.*, "Band alignment and minigaps in monolayer mos2-graphene van der waals heterostructures," *Nano letters*, vol. 16, no. 7, pp. 4054–4061, 2016.

[213] M. A. Kuroda, J. Tersoff, D. M. Newns, and G. J. Martyna, "Conductance through multilayer graphene films," *Nano Lett.*, vol. 11, pp. 3629–3633, Aug 2011.

[214] N. Sivadas, S. Okamoto, X. Xu, C. J. Fennie, and D. Xiao, "Stacking-dependent magnetism in bilayer cri3," *Nano Lett.*, vol. 18, no. 12, pp. 7658–7664, 2018.

[215] L. Tao and J. Wang, "Giant magnetoresistance and perfect spin filter effects in manganese phthalocyanine based molecular junctions," *Nanoscale*, vol. 9, no. 34, pp. 12 684–12 689, 2017.

[216] I. V. Krainov, J. Klier, A. P. Dmitriev, S. Klyatskaya, M. Ruben, W. Wernsdorfer, and I. V. Gornyi, "Giant magnetoresistance in carbon nanotubes with single-molecule magnets tbpc2," *ACS nano*, vol. 11, no. 7, pp. 6868–6880, 2017.

[217] S. Meena and K. Anudeep, "Spin transport study in chromium trihalides crcl 3, crbr 3, and cri 3: an ab initio study," *Journal of Superconductivity and Novel Magnetism*, pp. 1–10, 2019.

[218] L. Pan, L. Huang, M. Zhong, X.-W. Jiang, H.-X. Deng, J. Li, J.-B. Xia, and Z. Wei, "Large tunneling magnetoresistance in magnetic tunneling junctions based on two-dimensional crx 3 (x= br, i) monolayers," *Nanoscale*, vol. 10, no. 47, pp. 22 196–22 202, 2018.

[219] H. Li, Y.-K. Xu, K. Lai, and W.-B. Zhang, "The enhanced ferromagnetism of single-layer crx 3 (x= br and i) via van der waals engineering," *Physical Chemistry Chemical Physics*, vol. 21, no. 22, pp. 11 949–11 955, 2019.

[220] C. Cardoso, D. Soriano, N. García-Martínez, and J. Fernández-Rossier, "Van der waals spin valves," *Physical Review Letters*, vol. 121, no. 6, p. 067701, 2018.

[221] H. Zhang, Y. Ning, W. Yang, J. Zhang, R. Zhang, and X. Xu, "Possible realization of the high-temperature and multichannel quantum anomalous hall effect in graphene/crbr 3 heterostructures under pressure," *Physical Chemistry Chemical Physics*, vol. 21, no. 31, pp. 17 087–17 095, 2019.

[222] S. K. Behera, M. Bora, S. S. P. Chowdhury, and P. Deb, "Proximity effects in graphene and ferromagnetic crbr 3 van der waals heterostructures," *Physical Chemistry Chemical Physics*, vol. 21, no. 46, pp. 25 788–25 796, 2019.

[223] M. U. Farooq and J. Hong, "Switchable valley splitting by external electric field effect in graphene/cri 3 heterostructures," *npj 2D Materials and Applications*, vol. 3, no. 1, pp. 1–7, 2019.

[224] H. Li, Y.-K. Xu, Z.-P. Cheng, B.-G. He, and W.-B. Zhang, "Spin-dependent schottky barriers and vacancy-induced spin-selective ohmic contacts in magnetic vdw heterostructures," *Physical Chemistry Chemical Physics*, vol. 22, no. 17, pp. 9460–9466, 2020.

[225] X. Liu, C. Song, Z. Wu, J. Wang, J. Pan, and C. Li, "Bandgap opening and magnetic anisotropy switching by uniaxial strain in graphene/cri3 heterojunction," *Journal of Physics D: Applied Physics*, 2020.

[226] P. E. Blöchl, O. Jepsen, and O. K. Andersen, "Improved tetrahedron method for brillouin-zone integrations," *Physical Review B*, vol. 49, no. 23, p. 16223, 1994.

[227] M. Kawamura, Y. Gohda, and S. Tsuneyuki, "Improved tetrahedron method for the brillouin-zone integration applicable to response functions," *Physical Review B*, vol. 89, no. 9, p. 094515, 2014.

[228] M. B. Nardelli, F. T. Cerasoli, M. Costa, S. Curtarolo, R. De Gennaro, M. Fornari, L. Liyanage, A. R. Supka, and H. Wang, "Paoflow: A utility to construct and operate on ab initio hamiltonians from the projections of electronic wavefunctions on atomic orbital bases, including characterization of topological materials," *Computational Materials Science*, vol. 143, pp. 462–472, 2018.

[229] J.-E. Jørgensen, W. Marshall, and R. Smith, "The compression mechanism of crf3," *Acta Crystallographica Section B: Structural Science*, vol. 60, no. 6, pp. 669–673, 2004.

[230] A. v. Bondi, "van der waals volumes and radii," *The Journal of physical chemistry*, vol. 68, no. 3, pp. 441–451, 1964.

[231] C. Jin, F. A. Rasmussen, and K. S. Thygesen, "Tuning the schottky barrier at the graphene/mos2 interface by electron doping: density functional theory and many-body calculations," *The Journal of Physical Chemistry C*, vol. 119, no. 34, pp. 19 928–19 933, 2015.

[232] S. Duhm, G. Heimel, I. Salzmann, H. Glowatzki, R. L. Johnson, A. Vollmer, J. P. Rabe, and N. Koch, "Orientation-dependent ionization energies and interface dipoles in ordered molecular assemblies," *Nature materials*, vol. 7, no. 4, pp. 326–332, 2008.

[233] G. Heimel, I. Salzmann, S. Duhm, J. P. Rabe, and N. Koch, "Intrinsic surface dipoles control the energy levels of conjugated polymers," *Advanced Functional Materials*, vol. 19, no. 24, pp. 3874–3879, 2009.

[234] Y. Lin, X. Ling, L. Yu, S. Huang, A. L. Hsu, Y.-H. Lee, J. Kong, M. S. Dresselhaus, and T. Palacios, "Dielectric screening of excitons and trions in single-layer mos2," *Nano letters*, vol. 14, no. 10, pp. 5569–5576, 2014.

[235] K. F. Mak, C. Lee, J. Hone, J. Shan, and T. F. Heinz, "Atomically thin mos 2: a new direct-gap semiconductor," *Physical review letters*, vol. 105, no. 13, p. 136805, 2010.

[236] D. R. Klein, D. MacNeill, J. L. Lado, D. Soriano, E. Navarro-Moratalla, K. Watanabe, T. Taniguchi, S. Manni, P. Canfield, J. Fernández-Rossier *et al.*, "Probing magnetism in 2d van der waals crystalline insulators via electron tunneling," *Science*, vol. 360, no. 6394, pp. 1218–1222, 2018.

[237] H. H. Kim, B. Yang, T. Patel, F. Sfigakis, C. Li, S. Tian, H. Lei, and A. W. Tsen, "One million percent tunnel magnetoresistance in a magnetic van der waals heterostructure," *Nano letters*, vol. 18, no. 8, pp. 4885–4890, 2018.

[238] Y. Wang, L. Huang, L. Du, and X. Dai, "Doping-driven orbital-selective mott transition in multi-band hubbard models with crystal field splitting," *Chinese Physics B*, vol. 25, no. 3, p. 037103, 2016.

[239] M. A. Kuroda, J. Tersoff, and G. J. Martyna, "Nonlinear screening in multilayer graphene systems," *Physical review letters*, vol. 106, no. 11, p. 116804, 2011.

[240] A. C. Neto, F. Guinea, N. M. Peres, K. S. Novoselov, and A. K. Geim, "The electronic properties of graphene," *Reviews of modern physics*, vol. 81, no. 1, p. 109, 2009.

[241] J. Zhou, J. Qiao, C.-G. Duan, A. Bournel, K. L. Wang, and W. Zhao, "Large tunneling magnetoresistance in vse2/mos2 magnetic tunnel junction," *ACS applied materials & interfaces*, vol. 11, no. 19, pp. 17 647–17 653, 2019.

[242] L. V. Begunovich, A. V. Kuklin, M. A. Visotin, A. A. Kuzubov, F. N. Tomilin, A. S. Tarasov, Y. G. Mikhalev, and P. V. Avramov, "Triple vte2/graphene/vte2 heterostructures as perspective magnetic tunnel junctions," *Applied Surface Science*, vol. 510, p. 145315, 2020.

[243] F. Li, B. Yang, Y. Zhu, X. Han, and Y. Yan, "Four distinct resistive states in van der waals full magnetic 1t-vse2/cri3/1t-vse2 tunnel junction," *Applied Surface Science*, vol. 505, p. 144648, 2020.

[244] W. Yu, J. Li, T. S. Herng, Z. Wang, X. Zhao, X. Chi, W. Fu, I. Abdelwahab, J. Zhou, J. Dan *et al.*, "Chemically exfoliated vse2 monolayers with room-temperature ferromagnetism," *Advanced Materials*, vol. 31, no. 40, p. 1903779, 2019.

[245] M. Arai, R. Moriya, N. Yabuki, S. Masubuchi, K. Ueno, and T. Machida, "Construction of van der waals magnetic tunnel junction using ferromagnetic layered dichalcogenide," *Applied Physics Letters*, vol. 107, no. 10, p. 103107, 2015.

[246] W. Wang, A. Narayan, L. Tang, K. Dolui, Y. Liu, X. Yuan, Y. Jin, Y. Wu, I. Rungger, S. Sanvito *et al.*, "Spin-valve effect in nife/mos2/nife junctions," *Nano letters*, vol. 15, no. 8, pp. 5261–5267, 2015.

[247] K. Zhao, Y. Xing, J. Han, J. Feng, W. Shi, B. Zhang, and Z. Zeng, "Magnetic transport property of nife/wse2/nife spin valve structure," *Journal of Magnetism and Magnetic Materials*, vol. 432, pp. 10–13, 2017.

[248] M. F. Khan, H. Kim, G. Nazir, S. Jung, and J. Eom, "Layer dependent magnetoresistance of vertical mos 2 magnetic tunnel junctions," *Nanoscale*, vol. 10, no. 35, pp. 16 703–16 710, 2018.

[249] P. Kumar, A. Kumar, and D. Kaur, "Spin valve effect in sputtered fl-mos2 and ferromagnetic shape memory alloy based magnetic tunnel junction," *Ceramics International*, vol. 47, no. 4, pp. 4587–4594, 2021.

[250] J. Renteria, R. Samnakay, C. Jiang, T. Pope, P. Goli, Z. Yan, D. Wickramaratne, T. Salguero, A. Khitun, R. Lake *et al.*, "All-metallic electrically gated 2h-tase2 thin-film switches and logic circuits," *Journal of Applied Physics*, vol. 115, no. 3, p. 034305, 2014.

[251] T.-R. Chang, P.-J. Chen, G. Bian, S.-M. Huang, H. Zheng, T. Neupert, R. Sankar, S.-Y. Xu, I. Belopolski, G. Chang *et al.*, "Topological dirac surface states and superconducting pairing correlations in pbtase 2," *Physical Review B*, vol. 93, no. 24, p. 245130, 2016.

[252] J. Á. Silva-Guillén, P. Ordejón, F. Guinea, and E. Canadell, "Electronic structure of 2h-nbse2 single-layers in the cdw state," *2D Materials*, vol. 3, no. 3, p. 035028, 2016.

[253] D. C. Miller, S. D. Mahanti, and P. M. Duxbury, "Charge density wave states in tantalum dichalcogenides," *Physical Review B*, vol. 97, no. 4, p. 045133, 2018.

[254] A. Anikin, R. Schaller, G. Wiederrecht, E. Margine, I. Mazin, and G. Karapetrov, "Ultrafast dynamics in the high-symmetry and in the charge density wave phase of 2 h- nb se 2," *Physical Review B*, vol. 102, no. 20, p. 205139, 2020.

[255] J. Kang, W. Liu, D. Sarkar, D. Jena, and K. Banerjee, "Computational study of metal contacts to monolayer transition-metal dichalcogenide semiconductors," *Physical Review X*, vol. 4, no. 3, p. 031005, 2014.

[256] I. Popov, G. Seifert, and D. Tománek, "Designing electrical contacts to mos 2 monolayers: a computational study," *Physical review letters*, vol. 108, no. 15, p. 156802, 2012.

[257] G.-S. Kim, S.-H. Kim, J. Park, K. H. Han, J. Kim, and H.-Y. Yu, "Schottky barrier height engineering for electrical contacts of multilayered mos2 transistors with reduction of metal-induced gap states," *ACS nano*, vol. 12, no. 6, pp. 6292–6300, 2018.

[258] Q. H. Wang, K. Kalantar-Zadeh, A. Kis, J. N. Coleman, and M. S. Strano, "Electronics and optoelectronics of two-dimensional transition metal dichalcogenides," *Nature nanotechnology*, vol. 7, no. 11, pp. 699–712, 2012.

[259] S. Curtarolo, W. Setyawan, G. L. Hart, M. Jahnatek, R. V. Chepulskii, R. H. Taylor, S. Wang, J. Xue, K. Yang, O. Levy *et al.*, "Aflow: An automatic framework for high-throughput materials discovery," *Computational Materials Science*, vol. 58, pp. 218–226, 2012.

[260] Y. Zhang, M. Yoshida, R. Suzuki, and Y. Iwasa, "2d crystals of transition metal dichalcogenide and their iontronic functionalities," *2D Materials*, vol. 2, no. 4, p. 044004, 2015.

Appendices

Appendix A

APS Copyright Permission

American Physical Society
Reuse and Permissions License

02-Mar-2021

This license agreement between the American Physical Society ("APS") and Jonathan Heath ("You") consists of your license details and the terms and conditions provided by the American Physical Society and SciPris.

Licensed Content Information

License Number:	**RNP/21/MAR/037129**
License date:	02-Mar-2021
DOI:	10.1103/PhysRevB.101.195439
Title:	Role of quantum confinement and interlayer coupling in ${\mathrm{CrI}}_{3}$-graphene magnetic tunnel junctions
Author:	Jonathan J. Heath et al.
Publication:	Physical Review B
Publisher:	American Physical Society
Cost:	USD $ 0.00

Request Details

Does your reuse require significant modifications: No

Specify intended distribution locations:	Worldwide
Reuse Category:	Reuse in a thesis/dissertation
Requestor Type:	Student
Items for Reuse:	Whole Article
Format for Reuse:	Electronic

Information about New Publication:

University/Publisher:	Auburn University
Title of dissertation/thesis:	Characterization of Chromium Trihalide based Magnetic Tunnel Junctions via First Principles Calculations
Author(s):	Jonathan J Heath
Expected completion date:	May. 2021

License Requestor Information

Name:	Jonathan Heath
Affiliation:	Individual
Email Id:	jjh0041@auburn.edu
Country:	United States

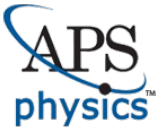

American Physical Society
Reuse and Permissions License

TERMS AND CONDITIONS

The American Physical Society (APS) is pleased to grant the Requestor of this license a non-exclusive, non-transferable permission, limited to Electronic format, provided all criteria outlined below are followed.

1. You must also obtain permission from at least one of the lead authors for each separate work, if you haven't done so already. The author's name and affiliation can be found on the first page of the published Article.
2. For electronic format permissions, Requestor agrees to provide a hyperlink from the reprinted APS material using the source material's DOI on the web page where the work appears. The hyperlink should use the standard DOI resolution URL, http://dx.doi.org/{DOI}. The hyperlink may be embedded in the copyright credit line.
3. For print format permissions, Requestor agrees to print the required copyright credit line on the first page where the material appears: "Reprinted (abstract/excerpt/figure) with permission from [(FULL REFERENCE CITATION) as follows: Author's Names, APS Journal Title, Volume Number, Page Number and Year of Publication.] Copyright (YEAR) by the American Physical Society."
4. Permission granted in this license is for a one-time use and does not include permission for any future editions, updates, databases, formats or other matters. Permission must be sought for any additional use.
5. Use of the material does not and must not imply any endorsement by APS.
6. APS does not imply, purport or intend to grant permission to reuse materials to which it does not hold copyright. It is the requestor's sole responsibility to ensure the licensed material is original to APS and does not contain the copyright of another entity, and that the copyright notice of the figure, photograph, cover or table does not indicate it was reprinted by APS with permission from another source.
7. The permission granted herein is personal to the Requestor for the use specified and is not transferable or assignable without express written permission of APS. This license may not be amended except in writing by APS.
8. You may not alter, edit or modify the material in any manner.
9. You may translate the materials only when translation rights have been granted.
10. APS is not responsible for any errors or omissions due to translation.
11. You may not use the material for promotional, sales, advertising or marketing purposes.
12. The foregoing license shall not take effect unless and until APS or its agent, Aptara, receives payment in full in accordance with Aptara Billing and Payment Terms and Conditions, which are incorporated herein by reference.
13. Should the terms of this license be violated at any time, APS or Aptara may revoke the license with no refund to you and seek relief to the fullest extent of the laws of the USA. Official written notice will be made using the contact information provided with the permission request. Failure to receive such notice will not nullify revocation of the permission.
14. APS reserves all rights not specifically granted herein.
15. This document, including the Aptara Billing and Payment Terms and Conditions, shall be the entire agreement between the parties relating to the subject matter hereof.